UCLA
UCLA Electronic Theses and Dissertations

Title
Chemical effect on diffusion in intermetallic compounds

Permalink
https://escholarship.org/uc/item/8bp6w3bh

Author
Chen, Yi-Ting

Publication Date
2016

Peer reviewed|Thesis/dissertation

eScholarship.org Powered by the California Digital Library
University of California

UNIVERSITY OF CALIFORNIA

Los Angeles

CHEMICAL EFFECT ON DIFFUSION IN INTERMETALLIC COMPOUNDS

A dissertation submitted in partial satisfaction of the

requirements for the degree Doctor of Philosophy

in Materials Science and Engineering

by

Yi-Ting Chen

2016

© Copyright by

Yi-Ting Chen

2016

ABSTRACT OF THE DISSERTATION

Chemical Effect on Diffusion in Intermetallic Compounds

by

Yi-Ting Chen

Doctor of Philosophy in Materials Science and Engineering

University of California, Los Angeles, 2016

Professor King-Ning Tu, Chair

With the trend of big data and the Internet of things, we live in a world full of personal electronic devices and small electronic devices. In order to make the devices more powerful, advanced electronic packaging such as wafer level packaging or 3D IC packaging play an important role. Furthermore, μ-bumps, which connect silicon dies together with dimension less than 10 μm, are crucial parts in advanced packaging. Owing to the dimension of μ-bumps, they transform into intermetallic compound from tin based solder after the liquid state bonding process. Moreover, many new reliability issues will occur in electronic packaging when the bonding materials change; in this case, we no longer have tin based solder joint, instead, we have intermetallic compound μ-bumps. Most of the potential reliability issues in intermetallic compounds are caused by the chemical reactions driven by atomic diffusion in the material; thus, to know the diffusivities of atoms inside a material is

significant and can help us to further analyze the reliability issues. However, we are lacking these kinds of data in intermetallic compound because there are some problems if used traditional Darken's analysis. Therefore, we considered Wagner diffusivity in our system to solve the problems and applied the concept of chemical effect on diffusion by taking the advantage that large amount of energy will release when compounds formed. Moreover, by inventing the holes markers made by Focus ion beam (FIB), we can conduct the diffusion experiment and obtain the tracer diffusivities of atoms inside the intermetallic compound. We applied the technique on Ni_3Sn_4 and Cu_3Sn, which are two of the most common materials in electronic packaging, and the tracer diffusivities are measured under several different temperatures; moreover, microstructure of the intermetallic compounds are investigated to ensure the diffusion environment. Additionally, the detail diffusion mechanism was also discussed in aspect of diffusion activation enthalpy and diffusion pre-factor by using lattice structure simulation. Last but not the least, X-ray photoelectron spectroscopy and First principal calculation simulation were used to observe the electron binding energies in the intermetallic compound and illustrate the partial covalent bonding behavior in the intermetallic compounds.

The dissertation of Yi-Ting Chen is approved.

Yu-Huang

Subramanian Srikantes Iyer

King-Ning Tu, Committee Chair

University of California, Los Angeles

2016

This thesis is dedicated to my family.

TABLE OF CONTENTS

LIST OF FIGURES

LIST OF TABLES

ACKNOWLEGEMENTS

Finishing this dissertation is one of the most challenging and gratifying experiences throughout my life. I am delightful to take the chance to show my appreciation for the help I received in this journey.

I would like to express my deepest gratitude to Professor King-Ning Tu, my advisor who led me, encouraged me and supported me through my Ph.D. journey. What I leaned from professor Tu was not only the vast technical knowledge, but also the logically thinking to the physics, things and life. I would also like to show my sincere thanks to Professor Yu Huang, Professor Subramanian Iyer, Professor Greg Carman and Professor Jenn-Ming Yang for being my dissertation committee members and their helpful comments.

I would like to extend my appreciation to Professor A. M. Gusak in the Department of Theoretical Physics, Cherkasy National University, Cherkasy, Ukraine, for his theoretical support and Professor C.Y. Liu from National Central University, Taiwan for providing me the precious samples. I would also like to thank Mr. Xia Yi (soon to be Dr. Xia Yi) for the support of First principle simulation. I could not finish my thesis without their valuable help.

I would also like to extend my thanks to Dr. Y.W. Cheng, Dr. Edward Cheng and Miss Yingxia Liu (soon to be Dr. Liu) for the valuable discussions.

Above all, I would like to thank my family for their love and support.

VITA

2010	B.S., Chemical Engineering National Taiwan University Taipei, Taiwan
2010-2011	Second Lieutenant ROC Army Taiwan
2012	Packaging Engineer Summer Internship TSMC Hsinchu, Taiwan
2013	M.S., Materials Science and Engineering University of California, Los Angeles Los Angeles, CA, USA
2013	Packaging Engineer Summer Internship Intel Corporation Chandler, AZ, USA

PUBLICATIONS

1. Yi-Ting Chen, Yingxia Liu and K.N. Tu, "Marker Analysis to Determine Dominant Diffusing Species in Ni3Sn4", Journal of Electronic Materials, 2016 TMS special issue for advanced packaging
2. Yi-Ting Chen, A.M. Gusak and K.N. Tu, "Determination of Tracer Diffusivites of Cu atoms and Sn atoms in Cu3Sn Intermetallic Compound by Considering Chemical Effect," 2016 ECTC proceedings
3. Yingxia Liu, Yi-Ting Chen, K.N. Tu, DW Kim and San Gu, " Fracture Reliability Concern of (Au,Ni)Sn4 Phase in 3D Integrated Circuit Microbumps Using Ni/Au Surface Finishing," Scripta Materialia (accepted)
4. David Chu, Jie-An Lin, Shu-Han Chao, Yi-Ting Chen, Chun-Chieh Wang, Yen-Fang Song, Cheng-Cheng Chiang, Chih Chen, and King-Ning Tu, " Chemical reactions to form layer-type and porous-type Cu3Sn in microbumps," JAP (under review)
5. Yi-Ting Chen, A.M. Gusak and K.N. Tu, "Chemical Effects on Intrinsic Diffusivities of Ni and Sn in Ni3Sn4 Intermetallic Compound," Acta Mat. (submitted)

Chapter 1 Introduction

1.1 Motivation

In mobile technology and the trend of Internet of things (IOT), the electronic devices are developing toward lower power consumption, more compact form factors and high performance, driving the growth of advanced electronic packaging industry. Among all the techniques, the use of 3-dimensional integrated circuits (3D IC) by stacking homogeneous or heterogeneous chips vertically (Fig. 1.1) has gained much attention recently [1-2], because it is a promising way to extent Moore's law on the trend of transistor circuit density increase in Si devices. The stacking approach requires the usage of micro solder bumps (μ-bump), having dimension approaching 10 μm. However, the reflow process to form the μ-bump (time and temperature in liquid-state bonding reaction) remains the same as that in forming larger solder joints. Thus, the fraction of intermetallic compound (IMC) inside a μ-bump is much larger, and its significance on reliability cannot be overemphasized.

The three most important IMCs in electronic packaging technology are Ni_3Sn_4, Cu_6Sn_5, and Cu_3Sn; there are many publications [3-9] on their basic physical properties such as conductivity, thermal expansion coefficient, hardness, Young's Modulus, and interdiffusion coefficient, except the intrinsic diffusivities. Yet, they are the basic kinetic parameters of the IMC and describe how fast they can diffuse in the IMC and determine the dominant diffusion species during the IMC growth. Furthermore, from the point of view of reliability under electromigration or stress-

migration, the rate of failure requires knowing the diffusivities. Moreover, recently there are many reliability issues on μ-bump such as porous Cu_3Sn formation [10], metastable phase in Ni-Sn system [11] and new failure mode in μ-bump under electromigration, these problems are all related to the diffusion of atoms inside the IMC. Thus, to know the intrinsic diffusivity of atoms inside the IMC is very significant in order to further analyze the reliability issue on μ-bump.

In the traditional way to obtain diffusivities of atoms in a binary metallic alloys, Darken's marker motion analysis and Boltzmann and Matano's analysis of interdiffusion [12-13] were combined to determine the intrinsic diffusivities. However, we note that in Boltzmann and Matano's analysis, it measures the concentration profile or gradient across the alloy. However, the concentration gradient is near zero and immeasurable experimentally across an IMC because we assume a stoichiometric compound. Fortunately, in a binary material, the thermodynamic factors for both atoms are the same [14]; therefore, tracer diffusivities of atoms can represent the intrinsic diffusivities. For metallic alloys, we can use chemical potential of an ideal dilute solution as well as a regular solution to obtain a thermodynamic factor, which represents the chemical effect. Additionally, the thermodynamic factor enables the intrinsic diffusivities link to the tracer diffusivities.

The challenge in obtaining tracer diffusivities in an IMC is how to remove the strong chemical bonding effect on diffusion. Thus, in our kinetic analysis of tracer diffusivities in IMC, we use Wagner diffusivities to overcome this problem. In Wagner's model of IMC growth, the diffusion is driven by heat of formation of IMC, not by chemical concentration gradient. A new thermodynamic factor was obtained

to convert the intrinsic diffusivities to tracer diffusivities in IMC.

On marker experiments, we used focus ion beam (FIB) to etch micron size cylindrical holes into IMC to serve as diffusion markers. They enabled us to observe the faster diffusing species as well as marker velocity. Specifically, we used FIB to etch marker holes on the growing IMC in the diffusion couple. Also we indented large and fixed markers on one side of the diffusion couple, as the references for marker motion measurements. Upon annealing the diffusion couples at several different temperatures and times to obtain the required data, we were able to calculate the tracer diffusivities of atoms in the IMC lattice. The activation energies of atomic diffusion in IMC can also be determined. The details of diffusion mechanism will be further discussed by using the lattice structure simulation, First-principle simulation model and x-ray photoelectron spectroscopy (XPS).

1.2 Introduction to Darken's analysis

Darken's analysis on marker motion is based on the experiment conducted by Kirkendall and the concept of vacancy diffusion [12-13]. For a substitutional diffusion based system, atoms are migrating through the vacancy process; the jump of an atom into a vacant site can be considered as the jump of a "vacancy" into the atom. In an A-B diffusion couple forming AB alloy in between as shown in Fig. 1.2; if the flux of A (J_A) is larger than the flux of B (J_B), then there will be a net flux of vacancy (J_V) in the opposite direction of A:

$$J_v = -J_A - J_B \quad \text{--- (1.1)}$$

If we applied Fick's first law [15-16] in equation 1.1, we get:

$$J_v = (D_A - D_B)\frac{\partial C_A}{\partial x} \quad \text{--- (1.2)}$$

where C_A is the concentration of A and D_A, D_B are the intrinsic diffusivities of A and B in AB alloy.

The net flux of the vacancies in AB alloy will accompany with the movement of the lattice, and edge dislocation is a good example to understand the phenomenon. Edge dislocations serve as good source or sinks for vacancies as shown in Fig. 1.3; the extra half-plane at A side can absorb vacancies and be annihilated eventually while the extra half-plane at B side can emit vacancies (absorb atoms) and the new atomic plane will be generated and introduced. Owing to the annihilation and generation of the lattice plane, the lattice plane in the middle will shift to left. If we put a marker between the annihilated and generated planes, we can observe the velocity of the moving lattice plane, v. If the area of the plane is A with concentration of atoms C_0, during a small amount of time t, there will be $AvtC_0$ atoms removed by the total amount of vacancies traveling across the plane in time t, which equals to J_vAt. Thus we can have the relation:

$$J_v = C_0 v \quad \text{--- (1.3)}$$

Substituting equation 1.2 gives:

$$v = (D_A - D_B)\frac{\partial X_A}{\partial x} \quad \text{--- (1.4)}$$

where the mole fraction of A is $X_A = C_A/C_0$.

Since the lattice plane is moving, if we observe total flux of A, J_A, at the stationary plane (e.g., the end of the diffusion couple) instead of the moving plane, we should notice that it is the sum of the diffusive flux relative to the moving lattice and flux caused by the movement of the lattice:

$$J_A = -D_A\frac{\partial C_A}{\partial x} + vC_A \qquad \text{--- (1.5)}$$

By combining equation 1.4 and equation 1.5, we obtain:

$$J_A = -(X_B D_A + X_A D_B)\frac{\partial C_A}{\partial x} = -\widetilde{D}\frac{\partial C_A}{\partial x} \qquad \text{--- (1.6)}$$

where $\widetilde{D}$ is interdiffusion coefficient.

1.3 Introduction to Boltzmann and Matano's analysis

The interdiffusion coefficient, $\widetilde{D}$, is not easy to determine analytically because we need to solve the partial differential equation resulting from Fick's law. Fortunately, Ludwig Boltzmann found a way to convert the partial differential equation into ordinary differential equation; which is much easier to solve; additionally, Chijiro Matano performed the experiment to calculate the interdiffusion coefficient in metal alloy.

To begin with, we should start from Fick's second law [15-16]:

$$\frac{\partial C_B}{\partial t} = \frac{\partial}{\partial x}\left(\tilde{D}\frac{\partial C_B}{\partial x}\right) = \frac{\partial \tilde{D}}{\partial x}\frac{\partial C_B}{\partial x} + \tilde{D}\frac{\partial^2 C_B}{\partial x^2} \qquad \text{--- (1.7)}$$

In order to solve this partial differential equation, we can assume that $C(x,t) = C(\eta)$ and $\eta = x/t^{1/2}$ to convert equation 1.7 into an easier-to-solve ordinary differential equation. By differentiation, we have:

$$\begin{aligned}
&\frac{\partial C}{\partial t} = \frac{\partial C}{\partial \eta}\frac{\partial \eta}{\partial t} = -\frac{1}{2}\frac{x}{t^{3/2}}\frac{dC}{d\eta} = -\frac{\eta}{2t}\frac{dC}{d\eta} \\
&\frac{\partial C}{\partial x} = \frac{\partial C}{\partial \eta}\frac{\partial \eta}{\partial x} = \frac{1}{t^{1/2}}\frac{dC}{d\eta} \\
&\frac{\partial^2 C}{\partial x^2} = \frac{\partial}{\partial x}\left(\frac{\partial C}{\partial x}\right) = \frac{\partial}{\partial \eta}\frac{\partial \eta}{\partial x}\left(\frac{\partial C}{\partial x}\right) = \frac{1}{t}\frac{d^2 C}{d\eta^2} \\
&\frac{\partial \tilde{D}}{\partial x} = \frac{\partial \tilde{D}}{\partial \eta}\frac{\partial \eta}{\partial x} = \frac{1}{t^{1/2}}\frac{d\tilde{D}}{d\eta}
\end{aligned} \qquad \text{--- (1.8)}$$

and we can substitute these terms from equation 1.7 into:

$$\begin{aligned}
&-\frac{\eta}{2t}\frac{dC}{d\eta} = \frac{1}{t^{1/2}}\frac{d\tilde{D}}{d\eta}\frac{1}{t^{1/2}}\frac{dC}{d\eta} + \frac{\tilde{D}}{t}\frac{d^2 C}{d\eta^2} \\
&-\frac{\eta}{2}\frac{dC}{d\eta} = \frac{d\tilde{D}}{d\eta}\frac{dC}{d\eta} + \tilde{D}\frac{d^2 C}{d\eta^2} = \frac{d}{d\eta}\left(\tilde{D}\frac{dC}{d\eta}\right)
\end{aligned} \qquad \text{--- (1.9)}$$

We can drop $1/d\eta$ in equation 1.9 and integrate both sides to obtain:

$$-\frac{1}{2}\int_0^{C'} \eta\, dC = \int_0^{C'} d\left(\tilde{D}\frac{dC}{d\eta}\right) = \left[\tilde{D}\frac{dC}{d\eta}\right]_0^{C'} \qquad \text{--- (1.10)}$$

where C' is an arbitrary concentration between 1 and C_0 where C_0 is the concentration of A at $x = \infty$ (pure A). Now we consider at a given time (t is a fixed constant), and both ends of the diffusion couple are pure A and pure B (constant concentration); we can integrate equation 1.10 from C=0 to C=C_0 along the C axis in Fig. 1.4 and obtain:

$$-\frac{1}{2}\int_0^{C'} \eta\, dC = \tilde{D}\frac{dC}{d\eta}\bigg|_{C=C_0} - \tilde{D}\frac{dC}{d\eta}\bigg|_{C=0} = 0 - 0 = 0 \qquad \text{--- (1.11)}$$

This infers that $\int_0^{C_0} x dC = 0$ because t is a constant, and x here determines the Matano interface at a given time t. The Matano interface represents the amount of A atoms been removed from the left of the interface is equal to the amount of A atoms been added to the right of the interface (the shaded areas on A side and B side in Fig. 1.4 are equal). Moreover, the Matono interface is the same as the original interface.

If we again consider at a fixed time t and convert η to x in equation 1.10, we can have the interdiffusion coefficient:

$$\tilde{D}(C') = -\frac{1}{2}\left(\frac{dx}{dC}\right)_{C'} \int_0^{C'} x\, dC \qquad \text{--- (1.12)}$$

At a given time t, we can measure the concentration profile of the diffusion couple as shown in Fig. 1.5, then we can choose a position with concentration C' and obtain the slope and the shaded area. By inserting them into equation 1.12, we know the interdiffusion coefficient $\widetilde{D}$ at the concentration C'. Therefore, we can know the interdiffusion coefficient by using the graphical method of Boltzmann-Matono analysis; in addition to Darken's marker analysis, we can solve the intrinsic diffusivities of atoms in a metal alloy.

1.4 Introduction to XPS analysis and chemical shift

X-ray photoemission spectroscopy (XPS) is also known as ESCA (Electron Spectroscopy for Chemical Analysis) [17-19], which is used to analyze atomic compositions and learn information about the types of bonding that occurs within various compounds on the sample surface (Fig. 1.6). The technique is based on Einstein's photoelectron effect theory, using X-ray source to strike and transfer the

entire energy to the electrons in atoms; if the energy is large enough for electrons to leave the atoms, then photoelectrons are generated and collected by the analyzer. If there are massive amounts of photoelectrons being generated, the analyzer can have enough data to generate the spectrum of the binding energy of the electrons. There are photoelectrons from various atomic orbitals with different binding energy, and the binding energy is equal to the kinetic energy measured by the analyzer plus the amount of energy the particle loses in transit from the sample to the analyzer, which is called work function; the work function is consistent for each sample on a specific XPS analyzer.

Since the binding energy is dependent on the type of atom the electron came from as well as the environment it came from. The electrons from the same atomic orbital from the same element might have different binding energy if there's a change in the chemical bonding of that element, in other words, the variation of the distribution of the charges at the atom site; and the phenomenon is called the chemical shift. The binding energies are determined by the electrostatic interaction between the electron and the nucleus plus the electrostatic shielding of the nuclear charge from all other electrons in the atom. Therefore, if there are electronic charges being withdrawal or added (lose or gain of the valence electron), the binding energy will also vary. For example, we can see the binding energy of Li 1s electron from pure Li and LiO_2 from Fig. 1.7. Originally, when Li 1s electron wanted to leave Li atom, the Li 2s electron outside will shield the nuclear charge and help Li 1s electron to leave and we will receive the binding energy of Li 1s from the analyzer. However, when Li_2O formed, the Li 2s will leave Li atom to O atom because the electronegativity for O atom is larger; now when Li 1s receive the X-ray energy and try to leave Li atom, there's no more Li 2s electron to shield the nuclear charge because the Li atom in

Li_2O has +1 valence charge compared to Li atom in pure Li. Therefore, the Li 1s electron in Li_2O is harder to leave and results in higher binding energy.

Except the chemical shift, there are other effects can cause the variation of the binding energy of the electron in an element. The energy from the X-ray may also transfer to the ions instead of the electrons, and it results in the excitation of the ions to the excited state instead of the ground state (main peak) as shown in Fig. 1.8a. The effects of excitation of the ions during photoemission process will make the photoelectrons have less kinetic energy, which means the analyzer will show higher binding energy in the spectrum. The excitation processes shown in the spectrum have to categories, and they are called shake-up and shake-off satellites. Shake-up satellite is because of the excitation of the electrons in the ions to bound state while Shake-off satellite is owing of the excitation of the electrons in the ions to unbound state as shown in Fig. 1.8b and Fig. 1.8c; furthermore, shake-up features especially common in transition metal oxides associated with paramagnetic species [20-22].

Overall, the shake-up and shake-off satellites peaks varied from parent photoelectron peak and are unique to each chemical state. This behavior can be used to analyze the chemical state of the elements. For instance, chemical shifts are too small to distinguish the chemical states of Mn in MnO from the main peaks of Mn 2p electrons in XPS spectrum as shown in Fig. 1.7. Nevertheless, the unique satellites peaks only occur in Mn^{2+} chemical states thus we can differentiate the Mn 2p in between pure Mn and MnO. In our study, we would like to use XRD technique to understand more about the chemical state change between the element in the IMC and its pure metal element, so that we can know the different bonding behavior between the element in the IMC and pure metal.

1.5 Introduction to First principle simulation

First principles physics model is a model that try to calculate the physical property quantitatively from the very basic established laws of physics without making any assumptions of the system [23-25]. For instance, calculation of electronic structure using Schrödinger's equation within a set of approximations that do not include fitting the model to experimental data [26] is one of the most important techniques. The values and the physical quantities from this approach and simulation provide a good estimation of the real state of the physical system; the model has high accuracy of its approximation and can be used in many physical inferences and applications. However, there are some limitations for first principles calculations; and it is not the complexity of the physics, but rather the size of the problem in terms of a numerical formulation. The development of accurate and efficient theoretical and computational techniques for dealing with so many particles is therefore central to the ongoing research in this field.

In this study, we would like to use the first principle approach to simulate the lattice on our intermetallic compounds. We start from a given lattice structure of the IMC, knowing what kinds of atoms they are made of and then further detail down to the amount of positively charged nucleus, and negatively charged electrons in the system. From the calculation and the simulation, we can understand the interactions between atoms such as chemical and molecular bonding by interpreting the energy of atomic orbitals for electrons for each element in the IMC, this can make us understand more about the chemical interaction in the IMC. Moreover, we can also know the

lattice vibrational pattern for the atoms in the IMC in the perfect lattice state, which can help us to illustrate the diffusion pre-factor in our diffusion analysis.

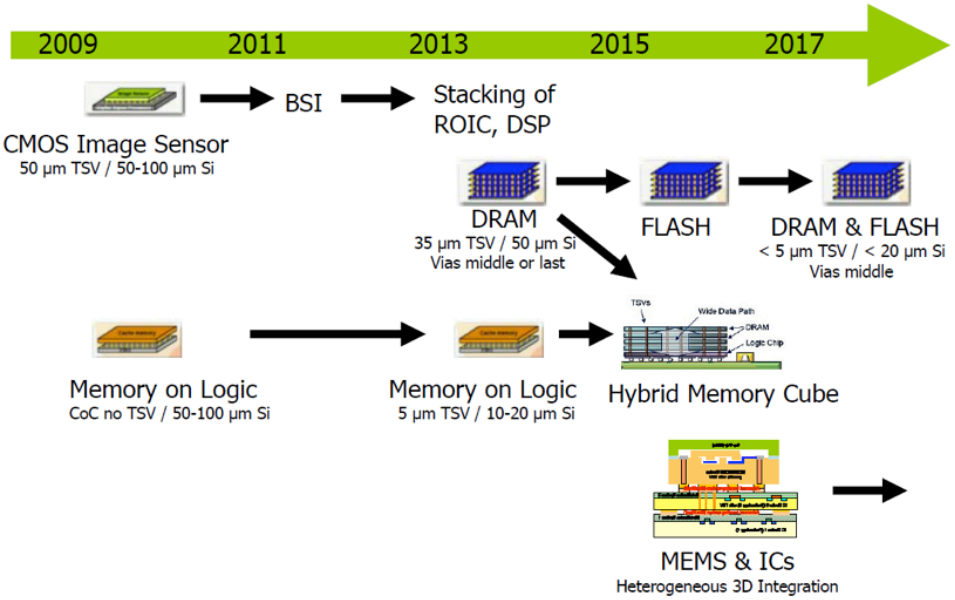

Figure 1.1 Trend of advanced packaging and 3D IC packaging

(Image from online resources)

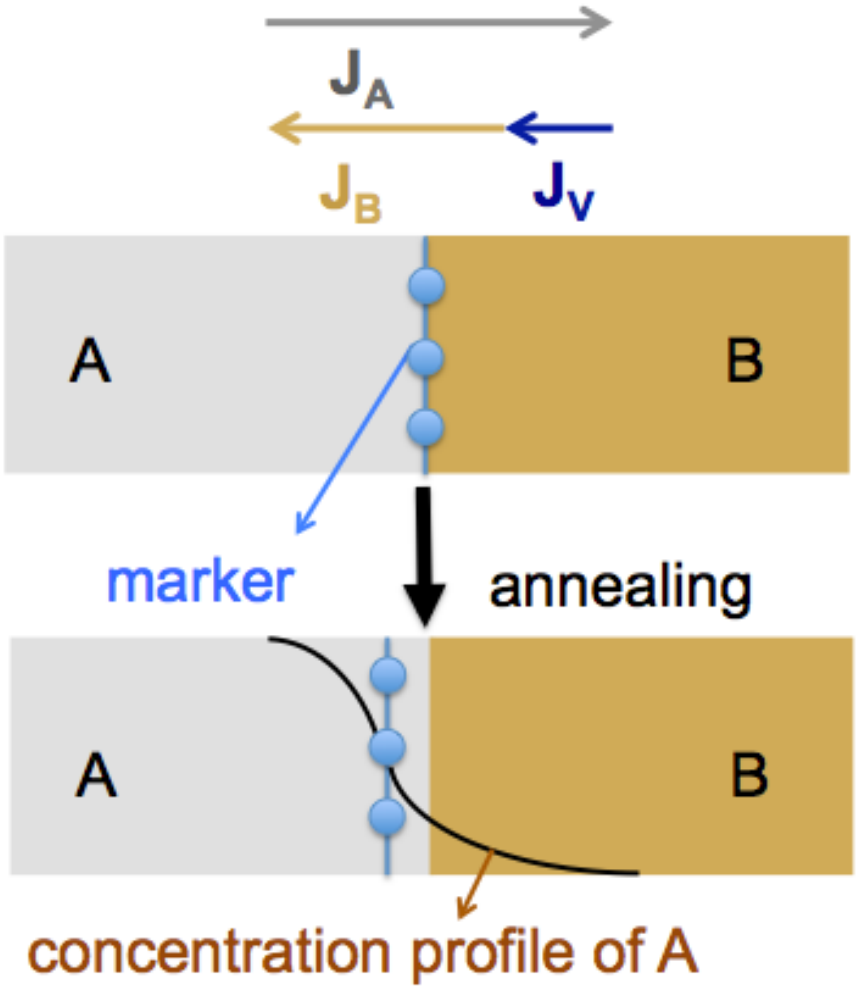

Figure 1.2 Diffusion couple of A metal/AB alloy/B metal and markers in the alloy region

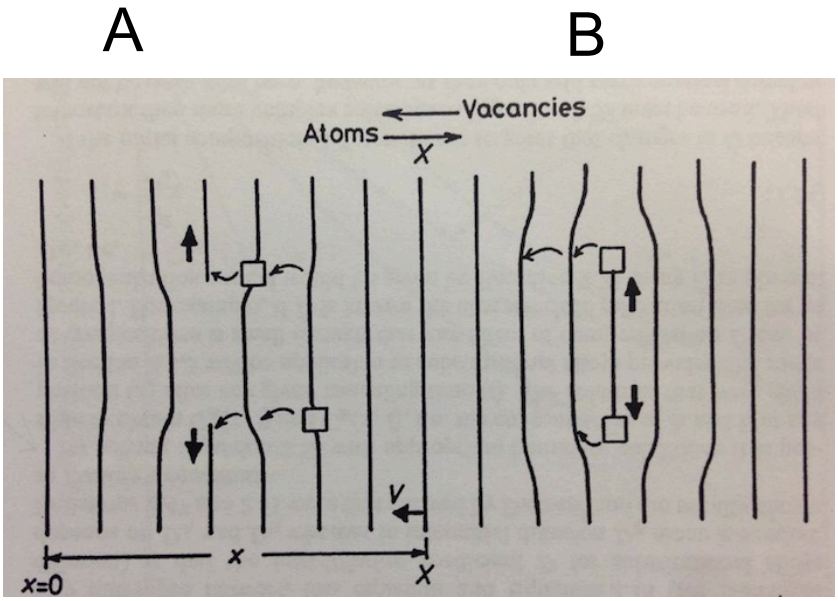

Figure 1.3 The edge dislocations in A lattice serve as good sinks of vacancies while the edge dislocations in the B lattice serve as good sources of vacancies

© King-Ning Tu, Electronic Thin-Film Reliability 2011
Cambridge University Press

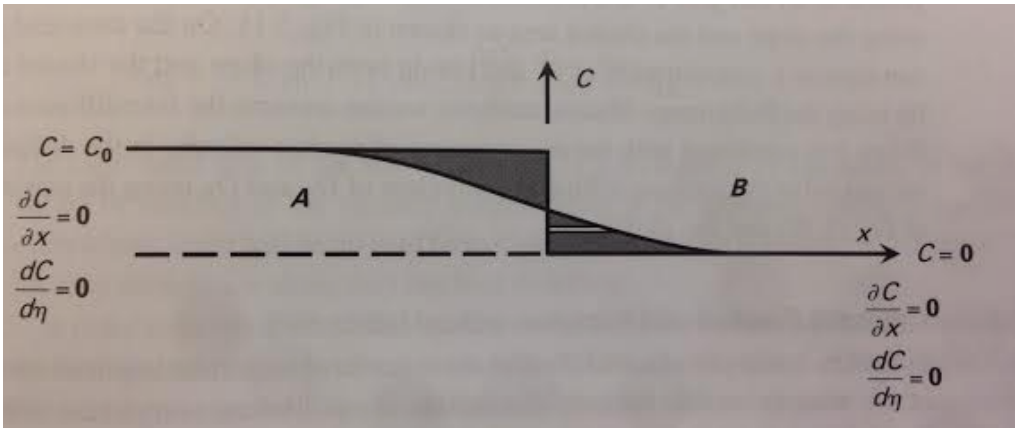

Figure 1.4 The location x where the left of the shaded area is equal to the right of shaded area along C axis defines Matano interface. A atoms removed from the left of the interface is equal to A atoms added to the right of the interface

© King-Ning Tu, Electronic Thin-Film Reliability 2011
Cambridge University Press

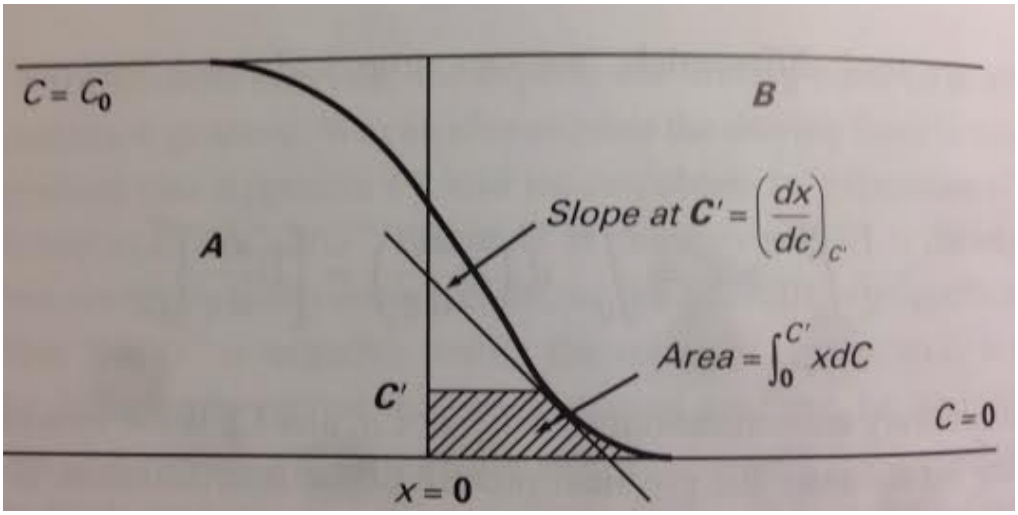

Figure 1.5 The interdiffusion coefficient at concentration C' can be obtained at a given t by knowing the slope and the shaded area at that concentration

© King-Ning Tu, Electronic Thin-Film Reliability 2011
Cambridge University Press

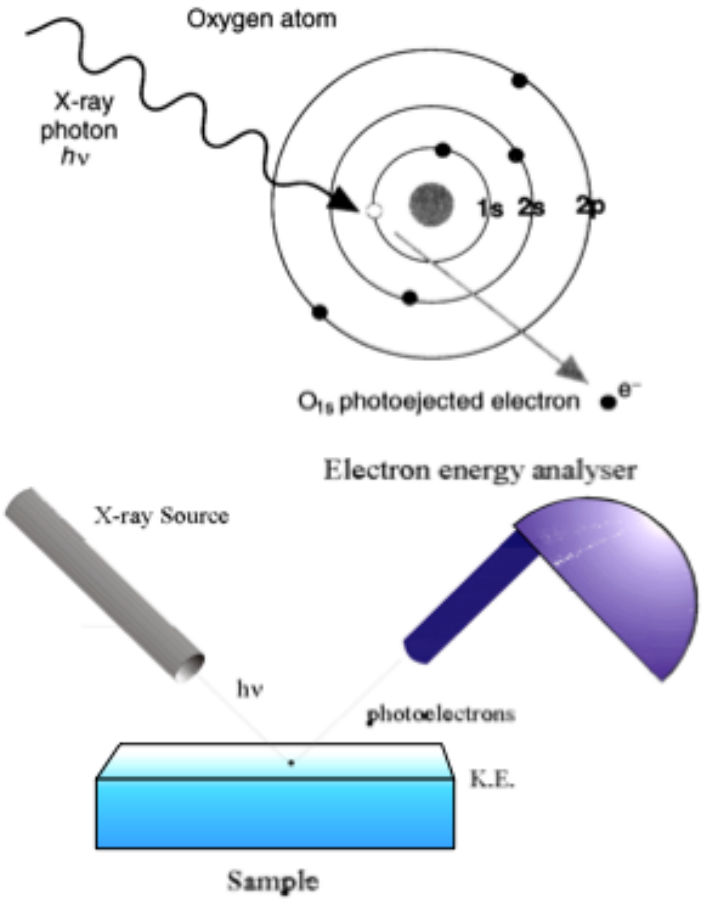

Figure 1.6 Schematic diagram about the functionality of XPS

(Image from UCLA XPS training materials)

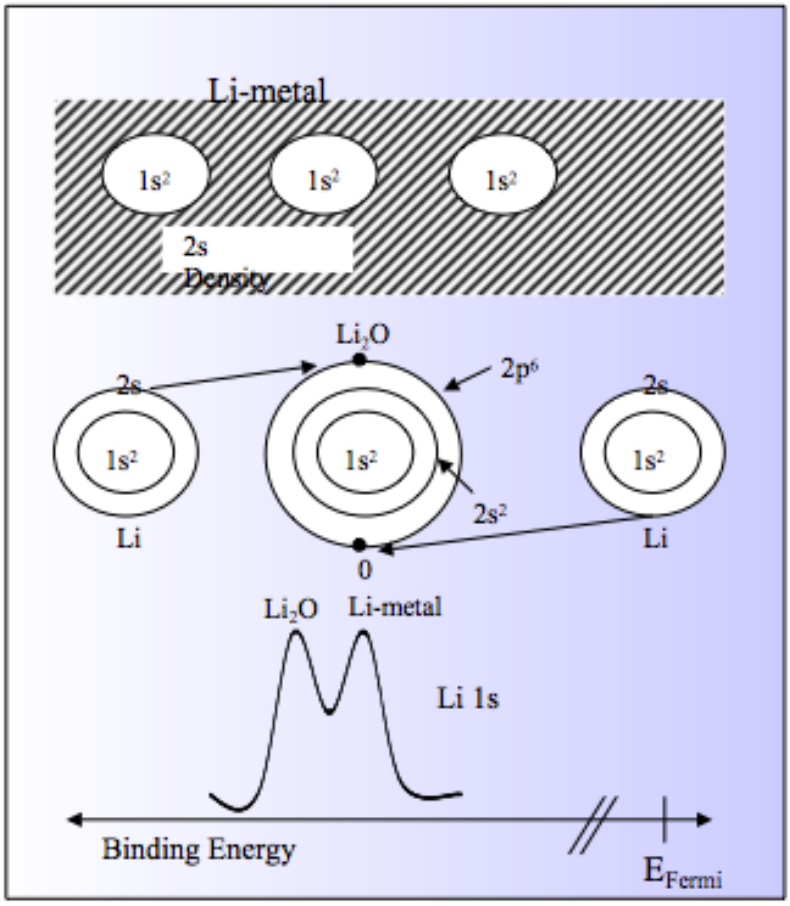

Figure 1.7 Chemical shift between Li 1s electron in pure Li metal and Li_2O compound

(Image from UCLA XPS training materials)

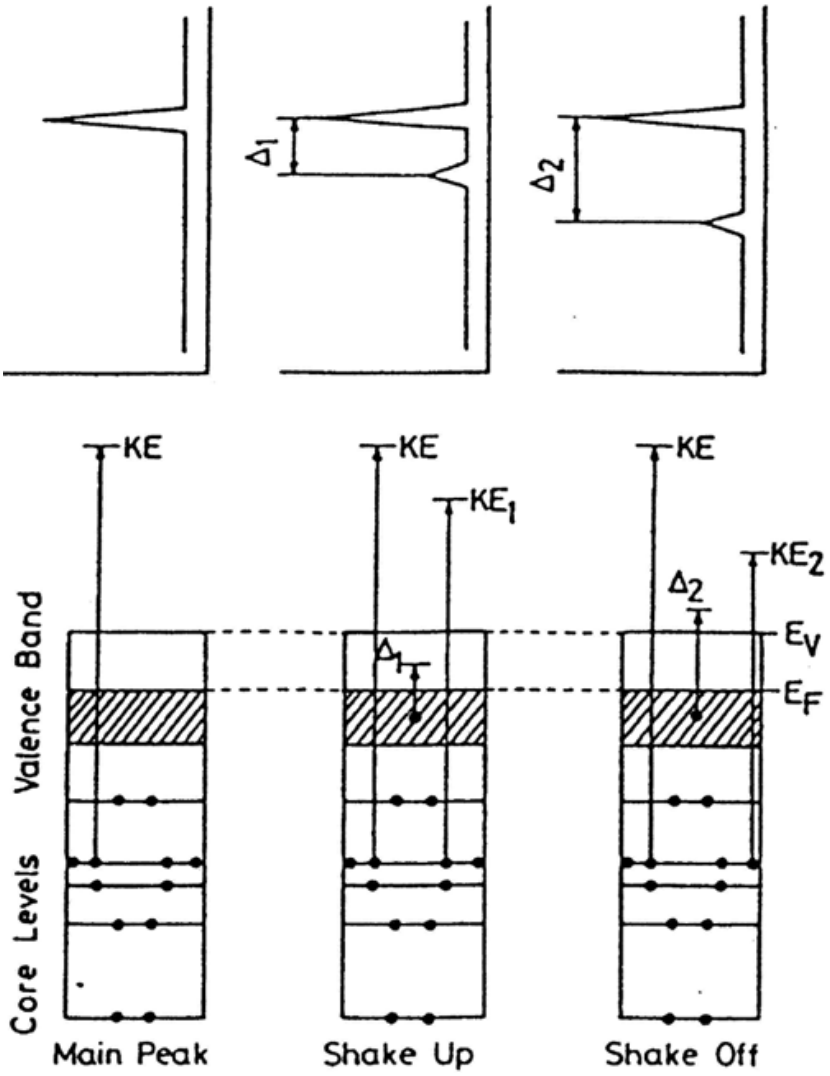

Figure 1.8 The shake-up and shake-off satellite peak caused by the excitation of other electrons in the ion

(Image from www.physics.nus.edu.sg)

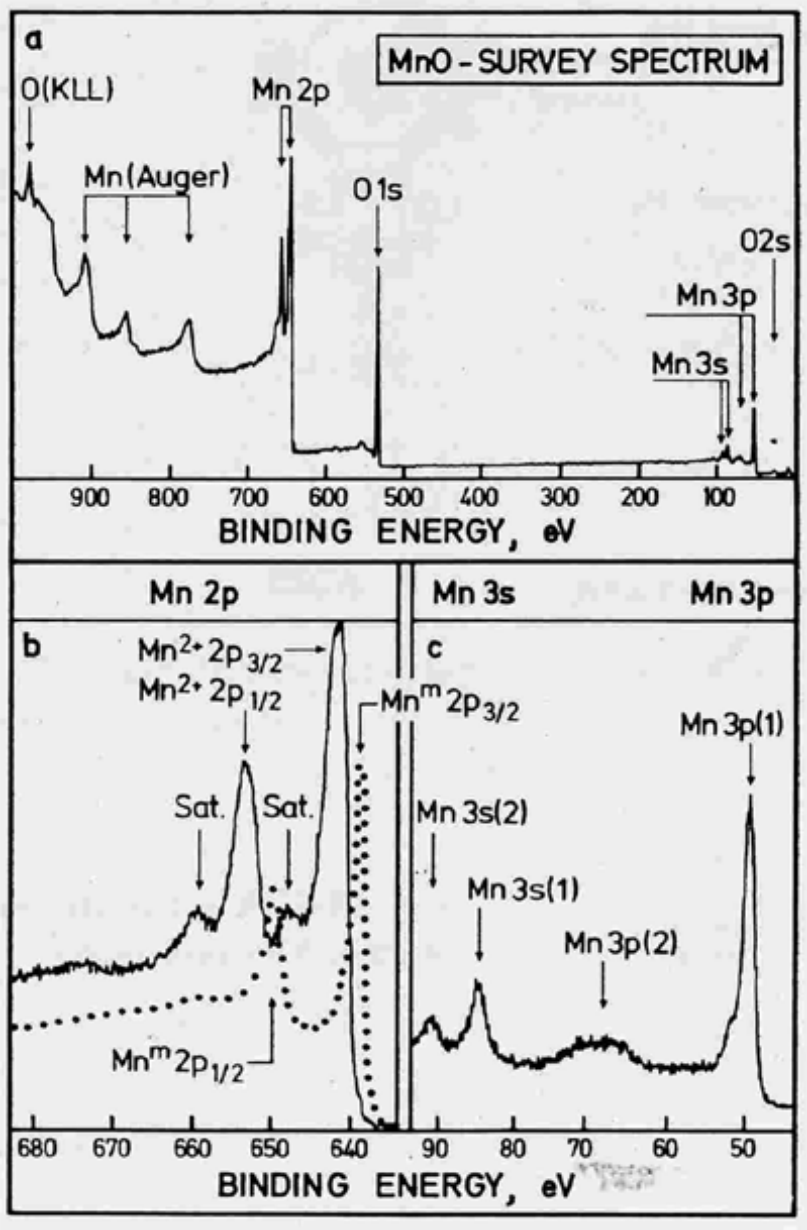

Figure 1.9 The unique XPS satellite peak for Mn^{2+} ion, which make it distinct from Mn

(Image from www.physics.nus.edu.sg)

Chapter 2 Chemical Effect on Diffusion

2.1 Diffusion analysis in the intermetallic compounds

To analyze the diffusion in the IMC that follow diffusion-control growth, we need to know the intrinsic diffusivities of atoms in the IMC. Recall that in the analysis in metal alloy, we can use Darken's marker analysis and Bolzmann-Matano analysis of interdiffusion to obtain the information. In interdiffusion forming an alloy, the composition changes continuously, so that we can apply the Matano's analysis to draw the slope at the alloy composition to obtain the interdiffusivity. However, a big issue in the IMC is that the composition (atomic concentration) changes abruptly across the phase interfaces (the interface of the IMC and the pure metal). Furthermore, the composition gradient inside an IMC is nearly flat since we assume stoichiometry compound [27]. Therefore, we should obtain a similar pair of equations for intermetallic compound.

We begin our analysis from considering the growth of a single layer of an intermetallic compound of i between pure A metal and pure B metal as shown in Fig. 2.1. That is the concentration profile of the diffusion couple, where we assume pure A with concentration C_A at A side and the one in B side is 0 due to the fact that they are nearly immiscible metals with negligible solubility of A in B or B in A. We can have equation 2.1 from considering mass balance at x_1 and x_2, where flux-in minus flux-out is equal to atoms accumulated minus depleted at the interface.

$$(C_1^{(i)} - C_A)\frac{dx_1}{dt} = J_{IMC} - 0 \qquad \text{--- (2.1a)}$$

$$(0 - C_2^{(i)})\frac{dx_2}{dt} = 0 - J_{IMC} \qquad \text{--- (2.1b)}$$

where $J_{IMC} = -\tilde{D}^{(i)}\frac{C_2^{(i)} - C_1^{(i)}}{x_2 - x_1} = \tilde{D}^{(i)}\frac{\Delta C^{(i)}}{\Delta x^{(i)}}$

is a flux in respect to laboratory reference frame (with respect to Matano plane) and t is time.

By subtracting (2) by (1) and assuming $C_1^{(i)} \approx C_2^{(i)} \approx C^{(i)}$, we can obtain:

$$x_i^2 - x_0^2 = 2\frac{(C_A)\Delta C^{(i)}}{(C_A - C^{(i)})C^{(i)}}\tilde{D}^{(i)}t \qquad \text{--- (2.2)}$$

Note that $\Delta C^{(i)}$ represents the concentration difference across the two interfaces of the IMC, since we assume intermetallic compound is stoichiometry, which means only a very narrow concentration range across the interfaces. The value is too small to be measured accurately and this is the fundamental obstacle mentioned before.

2.2 Chemical effect between atoms in solution

In IMC, the chemical interaction between A and B atoms must be very strong otherwise they will not bond together [28]. That is to say, AB bond (ε_{AB}) is much stronger than half of AA bond (ε_{AA}) plus BB bond (ε_{BB}) as shown in equation 2.3. To envision a clear picture of the chemical effect between atoms, we consider the partial pressure on a liquid solution surface (Fig. 2.2a) with extremely low concentration of B. The partial pressure of A and B above the surface are p_A and p_B, respectively. For

an ideal solution, AB bond is the same as BB bond and AA bond (as shown in equation 2.4) because there is no chemical effect between the atoms; and p_B will follow Raoult's law, be proportional to the concentration of B in the solution as depicted by the broken straight line in Fig. 2.2c.

$$\varepsilon_{AB} \geq \frac{1}{2}\left(\varepsilon_{AA} + \varepsilon_{BB}\right) \qquad \text{--- (2.3)}$$

$$\varepsilon_{AB} = \frac{1}{2}\left(\varepsilon_{AA} + \varepsilon_{BB}\right) \qquad \text{--- (2.4)}$$

For a regular solution, B atom is more eager to form AB bond than BB bond due to a stronger chemical interaction between A atom and B atom. This will cause p_B to have a negative deviation in dilute solid solution since the small number of B atoms are all surrounded by A atoms and locked by AB bonds which are harder to break and more stable compared to BB or AA bonds. When the B concentration goes up in the solution, there will be less AB bonds for B atom because B atom is less likely to be surrounded by all A atoms. That is to say, the chemical effect for B atom decreases, and the partial pressure of B will gradually become proportional to its concentration, this behavior is called Henry's law as the solid curve shown in Fig. 2.2c.

The chemical effect on diffusion is similar to the previous discussion. Let's take the substitutional diffusion in an AB alloy with low concentration of B for example. Since, B atom has more AB bond than A atom (stronger bonding), the vacancy exchange process with B atom is harder than with A atom. To understand more about the process, we use chemical potential (μ) as the factor of driving force of the diffusion as below:

$$\mu = kT \ln a = kT \ln \gamma X \qquad \text{--- (2.5)}$$

where a is defined as the activity and γ is the activity coefficient. Since diffusion is driven by chemical potential gradient, we can first derive the atomic flux equation of B atom in an ideal solid solution (a=X) similar to Fick's first law:

$$J_B = C_B < v >= C_B MF = C_B \frac{D_B^*}{kT}\left(-\frac{\partial \mu_B}{\partial x}\right) \qquad \text{--- (2.6)}$$

$$J_B = C_B \frac{D_B^*}{kT}\left(-\frac{\partial}{\partial x}\left(kT \ln X_B\right)\right) = \frac{D_B^*}{kT}\left(-\frac{\partial C_B}{\partial x}\right) \qquad \text{--- (2.7)}$$

where <v> is the drift velocity, M is the atomic mobility and F is the driving force. The system is in chemical homogeneous state for an ideal solution, thus D_B^* represents the tracer diffusivity and the diffusivity in Fick's first law is referring to tracer diffusivity. We can apply the same procedure to analyze the regular solution where the system is not in chemical homogeneous state and obtain equation 2.6. The chemical effect that causes non-homogenous of the system is included in μ_B. By substituting $\mu_B = kTln\gamma_B X_B$, we have:

$$\begin{aligned} J_B &= C_B \frac{D_B^*}{kT}\left(-\frac{\partial \mu_B}{\partial X_B}\frac{\partial X_B}{\partial x}\right) \\ &= \frac{X_B}{\Omega}\frac{D_B^*}{kT}\frac{\partial X_B}{\partial x}\frac{\partial}{\partial X_B}\left(kT \ln X_B + kT \ln \gamma_B\right) \\ &= \frac{X_B}{\Omega}\frac{D_B^*}{kT}\frac{\partial X_B}{\partial x}\left[\frac{kT}{X_B}\left(1+\frac{\partial \ln \gamma_B}{\partial \ln X_B}\right)\right] \end{aligned}$$

$$J_B = -D_B^*\left(1+\frac{\partial \ln \gamma_B}{\partial \ln X_B}\right)\frac{\partial C_B}{\partial x} = -D_B \frac{\partial C_B}{\partial x} \qquad \text{--- (2.8)}$$

where Ω is the atomic volume. From equation 2.8, we can see the relationship between tracer diffusivity and intrinsic diffusivity as:

$$D_B = D_B^*\left(1+\frac{\partial \ln \gamma_B}{\partial \ln X_B}\right) = D_B^*\phi \qquad \text{--- (2.9)}$$

where ϕ is defined as thermodynamic factor for diffusion; if we follow the same derivation for diffusion of A atom, we can obtain:

$$D_A = D_A^*\left(1+\frac{\partial \ln \gamma_A}{\partial \ln X_A}\right) = D_A^*\phi \qquad \text{--- (2.10)}$$

In a binary system, the thermodynamic factors for both atoms are the same (will show in next session); therefore, we can express the interdiffusion coefficient in another form:

$$\tilde{D} = X_B D_A + X_A D_B = \left(X_B D_A^* + X_A D_B^*\right)\phi \qquad \text{--- (2.11)}$$

In equation 2.11, we can see that $\tilde{D}$ consists of two parts, the thermodynamic part and the kinetic part. The thermodynamic part, ϕ, is the driving force of diffusion and includes chemical effect. On the other hand, the term inside parentheses can be determined by measuring the tracer diffusivities of A atoms and B atoms inside the AB alloy. This is because the chemical effect has been singled out in thermodynamic factor; the behavior inside the parenthesis is just like ideal solution. Nevertheless, it is worth to note that the tracer diffusivities vary with the alloy composition, and they are related to the activation barrier of diffusion.

2.3 **Chemical effect on diffusion in the intermetallic compounds**

For an intermetallic compound formation, it is intuitively to think that there's strong chemical effect between A atom and B atom is strong. We can take advantage of this fact to conquer the obstacle we encountered in the diffusion analysis [29]. First we can depict the chemical interaction between A atom and B atom in free energy diagram of A (α-phase), B (β-phase) and an intermetallic compound (i-phase) as shown in Fig. 2.3. The upper line across g_A and g_B represents the mechanical mixing without any chemical effect between the atoms, and we can have Gibbs free energy in mechanical mixing as:

$$G = \mu_A N_A + \mu_B N_B \qquad \text{--- (2.12)}$$

where N_A and N_B are number of A and B atoms respectively. In mechanical mixing, μ_A and μ_B represent the chemical potentials of A and B atoms in pure metals so that they are constants due to the lack of chemical effect. If we assume total numbers of atoms, $N= N_A + N_B$, we can take $g = G/N$ as Gibbs free energy per atom as:

$$g = \mu_A X_A + \mu_B X_B \qquad \text{--- (2.13)}$$

where $X_A=N_A/N$ and $X_B=N_B/N$ are the molar fraction of A and B in the binary system and $X_A + X_B = 1$. In the analysis of intermetallic compound, μ_A and μ_B vary with the concentration; that is to say, μ_A and μ_B are function of X_A and X_B. Given these facts, we can have:

$$dg\Big|_{T,p} = (\mu_A - \mu_B) X_A \qquad \text{--- (2.14)}$$

and

$$\mu_A = g + X_B \frac{\partial g}{\partial X_A}$$
$$\mu_B = g - X_A \frac{\partial g}{\partial X_A} \qquad \text{--- (2.15)}$$

By further partial differentiation, we get:

$$\frac{\partial \mu_A}{\partial X_A} = \frac{\partial g}{\partial X_A} + \frac{\partial X_B}{\partial X_A}\frac{\partial g}{\partial X_A} + X_B \frac{\partial^2 g}{\partial X_A^2} = X_B \frac{\partial^2 g}{\partial X_A^2} = X_B g''$$
$$\frac{\partial \mu_B}{\partial X_A} = \frac{\partial g}{\partial X_A} - \frac{\partial X_A}{\partial X_A}\frac{\partial g}{\partial X_A} - X_A \frac{\partial^2 g}{\partial X_A^2} = X_A \frac{\partial^2 g}{\partial X_A^2} = -X_A g'' \qquad \text{--- (2.16)}$$

From our previous discussion, thermodynamic factor stands for the chemical effect in a system, thus we should express it as:

$$\phi_A = \frac{X_A}{kT}\frac{\partial \mu_A}{\partial X_A} = \frac{X_A X_B}{kT} g''$$
$$\phi_B = \frac{X_B}{kT}\frac{\partial \mu_B}{\partial X_B} = \frac{X_B}{kT}\frac{-\partial \mu_B}{\partial X_A}\frac{X_A X_B}{kT} g'' \qquad \text{--- (2.17)}$$

Noted that in a binary system, the thermodynamic factor for both atoms are the same because the chemical effect is the chemical interaction between two atoms. To obtain the thermodynamic factor, we can use graphical method in Fig. 2.3; we first draw two common tangent line from A (α-phase) and B (β-phase) to the i-phase. The tangential point at i-phase for the common tangent line of the α-phase and the i-phase is X_L while the one for the common tangent line of the β-phase and the i-phase is X_R. The meaning of the tangent line is that the system is at the thermodynamic equilibrium along (same Gibbs free energy per atom) the line. From the figure, we can define:

$$\frac{\left.\frac{\partial g}{\partial X}\right|_{X_R} - \left.\frac{\partial g}{\partial X}\right|_{X_L}}{X_R - X_L} \approx \frac{\partial^2 g}{\partial X^2} = g^{"} \qquad \text{--- (2.18)}$$

where $\Delta X = X_R - X_L$. We can further express:

$$\begin{aligned} g^{"}\Delta X &= \left.\frac{\partial g}{\partial X}\right|_{X_R} - \left.\frac{\partial g}{\partial X}\right|_{X_L} = \frac{g_B - g_i}{1 - X_i} - \frac{g_i - g_A}{X_i - 0} \\ &= \frac{\left[g_B X_i - g_A\left(1 - X_i\right)\right] - g_i}{\left(1 - X_i\right)X_i} = \frac{g - g_i}{\left(1 - X_i\right)X_i} = \frac{\Delta g_i}{X_A X_B} \end{aligned} \qquad \text{--- (2.19)}$$

where $X_i \approx X_L \approx X_R$ and the square bracket term is equal to g by the lever rule. Thus,

$$\Delta g_i = X_A X_B g^{"}\Delta X \qquad \text{--- (2.20)}$$

We can take $(g - g_i) = \Delta g_i$ to be the intermetallic compound formation energy per atom. Now we can replace the thermodynamic term in equation 2.11 and get:

$$\begin{aligned} \tilde{D} &= (X_A D_B^* + X_B D_A^*)\phi = (X_A D_B^* + X_B D_A^*)\frac{X_A X_B}{kT} g^{"} \\ &= (X_A D_B^* + X_B D_A^*)\frac{\Delta g_i}{kT\Delta X} \end{aligned} \qquad \text{--- (2.21)}$$

By rearranging, we obtain:

$$\tilde{D}\Delta X = (X_A D_B^* + X_B D_A^*)\frac{\Delta g_i}{kT} \qquad \text{--- (2.22)}$$

Although ΔX is immeasurable according to the previous discussion; however, the product $\tilde{D}\Delta X$ is measurable since we can easily know the formation energy of the intermetallic compound per atom. Moreover, knowing that $\Delta X = \Omega \Delta C$ where Ω is the atomic volume, we get:

$$\tilde{D}\Delta C = (X_A D_B^* + X_B D_A^*)\frac{\Delta g_i}{\Omega kT} \quad \text{--- (2.23)}$$

Then we can substituting equation 2.23 into equation 2.2, we have:

$$x_i^2 - x_0^2 = 2\frac{(C_A)}{\Omega(C_A - C^{(i)})C^{(i)}}(X_A D_B^* + X_B D_A^*)\frac{\Delta g_i}{kT}t \quad \text{--- (2.24)}$$

Now we have equation 2.24 as our first equation to obtain tracer diffusivities in the intermetallic compound. It is worth mentioning that after we have corrected the chemical effect, we can regard the intrinsic diffusivities as the tracer diffusivities.

2.4 Wagner diffusivity

Wagner diffusivity describes the abilities of atomic diffusion inside the intermetallic compound [30], including the chemical potential gradient and tracer diffusivity; that is to say, the diffusion driving force plus the diffusion ability of an atom inside a material. To understand more about Wagner diffusivity, we should start from analyzing the interdiffusivity on the steady-state intermetallic compound growth. Intermetallic compound has narrow concentration range as we discussed earlier, we can describe the flux inside the intermetallic compound as:

$$J_{IMC} = -C\tilde{D}(X_B(x))\frac{\partial X_B}{\partial x} \quad \text{--- (2.25)}$$

Although interdiffusivity is a function of concentration (X_B), we can introduce the average interdiffusivity (equation 2.26) or treat it as a constant due to the fact that concentration difference across the IMC is small.

$$< \tilde{D} >= \frac{\int_{x_L}^{x_R} \tilde{D}(X_B) dX_B}{x_R - x_L} \approx \tilde{D} \qquad \text{--- (2.26)}$$

Then we can express the flux in the IMC as:

$$J_{IMC} = -C \frac{\int_{x_L}^{x_R} \tilde{D}(X_B) dX_B}{x_R - x_L} = -C \frac{< \tilde{D} > \Delta X_B}{x_R - x_L} \approx \text{constant} \qquad \text{--- (2.27)}$$

However, in case of compound growth this expression for flux is not convenient, because the flux is finite for sure, and the concentration range for compound is often immeasurable, formally tending to zero. Then it means that average interdiffusivity should tend to infinity – also immeasurable. It seems useless to use the infinitely small and infinitely large quantities for analysis of experimental facts. Nevertheless, it is useful to use the product of immeasurably large parameter and immeasurably small parameter which is quite measurable and called Wagner diffusivity:

$$< \tilde{D} > \Delta X_B = \int_{x_L}^{x_R} \tilde{D}(X_B) dX_B \qquad \text{--- (2.28)}$$

We can interpret Wagner diffusivity using Darken's expression:

$$< \tilde{D} > \Delta X_B = \int_{x_L}^{x_R} \tilde{D}(X_B) dX_B = \int_{x_L}^{x_R} (X_A D_B^* + X_B D_A^*) \frac{X_A X_B}{kT} \frac{\partial^2 g}{\partial X_B^2} dX_B \qquad \text{--- (2.29)}$$

Since the concentration difference is tiny, we can consider the concentration across the intermetallic as a constant and transform equation 2.29 further into:

$$\begin{aligned} < \tilde{D} > \Delta X_B &= \left(X_A < D_B^* > + X_B < D_A^* > \right) \frac{X_A X_B}{kT} \int_{x_L}^{x_R} \frac{\partial^2 g}{\partial X_B^2} dX_B \\ &= \left(X_A < D_B^* > + X_B < D_A^* > \right) \frac{X_A X_B}{kT} \times \left(\left. \frac{\partial g}{\partial X_B} \right|_{X_R} - \left. \frac{\partial g}{\partial X_B} \right|_{X_L} \right) \end{aligned} \qquad \text{--- (2.30)}$$

Then we can get equation 2.23 by using graphical method discussed before.

2.5 Hybrid bonding in the intermetallic compounds

The bonding of alloys composed of metallic elements is naturally expected to be metallic and the mechanical property is expected to be ductile since there are delocalized electrons in metallic bonds to contribute the movement of the lattice. On the other hand, ceramic material such as SiO_2 is not electrical conductive and brittle because the bonding between Si atom and O atom is ionic bonding, which confines the electrons in local positions. However, for intermetallic compounds, we found out it is electrical conductive but brittle; thus the bonding between the two elements in the intermetallic compound is of interest and it is intuitively think that the bonding behavior should lie in between metallic or ionic.

To understand more, we first take a look at intermetallic compounds formed by transition metals and polyvalent main-group elements such a Al or Si because they can form strong hybridization covalent bond and result in bandgap formation at Fermi level, causing the semiconducting and brittle property of the material. Out of all possible intermetallic compounds formed by transition metals and polyvalent main-group elements, Al_3V is most representative and has the most interesting properties [31-33]. From the electronic spectrum of Al_3V calculated from First principle model as shown in Fig. 2.4, we can observe that there is a very deep pseudogap in the DOS close to the Fermi level. At the left of the bandgap represents the bonding behavior while at the right of the bandgap represents the anti-bonding behavior, which is the

typical covalent bonding behavior (e.g, σ-σ bond and σ*-σ* bond). This important feature infers that the p orbital in Al and the d orbital in V have strong hybridization effect in Al_3V.

The framework of Friedel–Anderson virtual bound states (VBSs) model [34-35] is the basic theory usually used to illustrate the physical property of transition metallic aluminides. In the theory, the overlap between d-d orbital between the transition metal is very small due to the atomic distance is large compared to the radius of d-orbital in the atom. The virtual bond state is formed owing to the hybridization of d-orbital with the conduction band, leads to the resonance at the Fermi level; and VBS creates asymmetric narrow peak around the Fermi level. Yet in Al_3V system, it is not totally the case, we need to use an alternative framework is followed by the Hume–Rothery rule [36-37]. The theory correlates the compound lattice structure and the average number of electrons per atom, which can refer to strong directional bonding in the intermetallic compound and the fail of free-electron model.

The Al_3V intermetallic compound has the modified face center cubic crystal structure, which is also known as DO_{22} (Al_3Ti) lattice structure as shown in Fig. 2.5. The elementary cell is orthorhombic and consists of two primitive cells, which contains four atoms. Moreover, The elementary cell consists of two fcc unit stacked along the z-direction all atoms in the primitive cells are located on the sites of a fcc lattice. The crystal symmetry plays a significant role for the deep pseudogap formation in density of state shown in Fig. 2.4. Normally, the bonding in an intermetallic compound is very complicated, but the high symmetry crystal structure can help us to analyze the bonding mechanism and identify the hybridized orbital

more easily. To have a deeper understanding, we focus on the V-Al2 bond, their hybridized orbitals oriented along the bonds, and projected density of state onto bonding and anti bonding calculated by Hafner et al. [38].

According to the interpretations of Hafner, the vanadium atom is bonded with two Al2 atoms, and the Al2 atoms have four V neighbors located at the vertices of a tetrahedron in Al_3V intermetallic compound. The symmetrized orbitals on the Al2 atoms are thus sp^3 hybrids formed by s, p_X, p_Y and p_Z orbitals. Hafner also verified through calculation that d^4 hybrid orbitals formed by the d_Z^2 , $d_X^2{-}_Y^2$, d_{ZX}, d_{YZ} states (or sd^3 hybridization if we consider the s orbital instead of the d_Z2) dominate the bonding. Therefore, $V(d^4)$–$Al2(sp^3)$ are orbitals which plays dominant roles in V–Al2 bonding. Furthermore, we can also see the strong directional bonding behavior from the electronic density projection picture in Fig. 2.6, which is another strong evidence of strong covalent Al–V bonds due to the orbital hybridization between Al(s, p) and V(d).

In order to see the symmetry effect on bonding and the electronic distribution in the lattice, Hafner also do the First principle simulation by assuming $L1_2$ crystal structure of Al_3V as shown in Fig. 2.7; where is a similar modified face center cubic structure with different symmetric system. The orbital energy diagram in Fig. 2.8 shows that the gap at the Fermi level is shallower, which suggests less covalent bonding behavior and higher electrical conductivity property. This fact gives us a clear picture about the partial covalent bonding behavior in intermetallic compound.

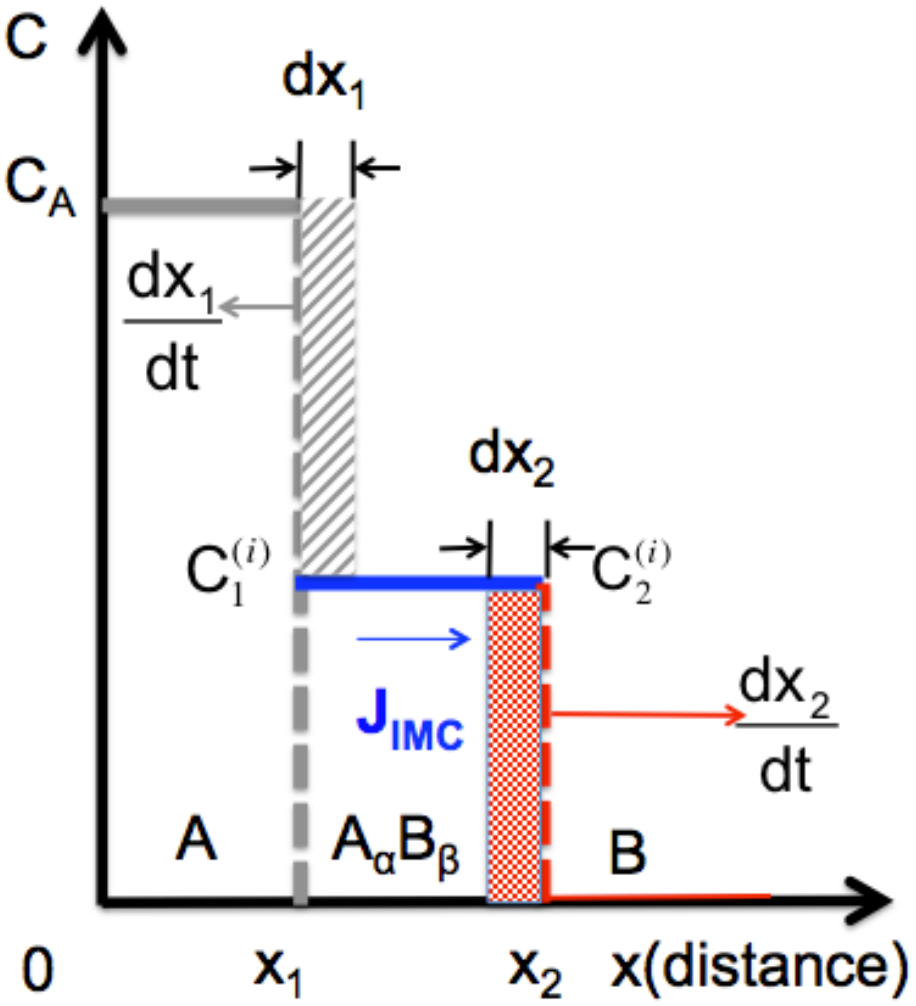

Figure 2.1 Concentration profile of A versus the x direction of the A/IMC/B diffusion couple

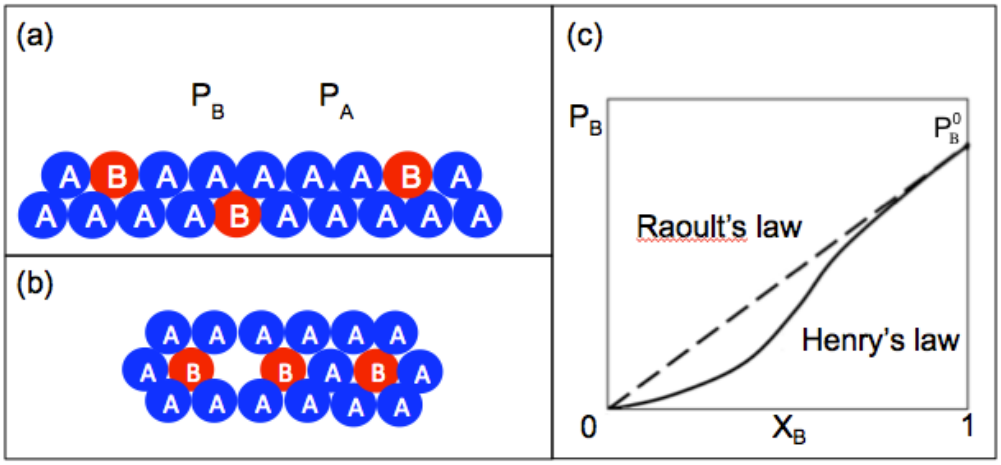

Figure 2.2 Atomic schematic diagrams with low B concentration (a) at the surface (b) inside the lattice (c) partial pressure of B versus concentration of B

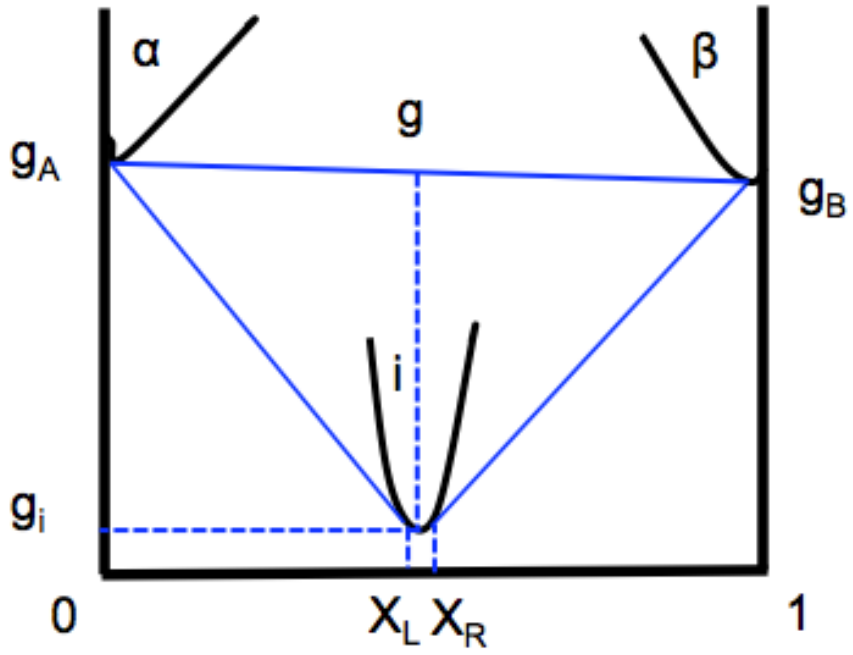

Figure 2.3 Gibbs free energy diagram of A (a-phase) and B (b-phase) and an intermetallic compound (i-phase)

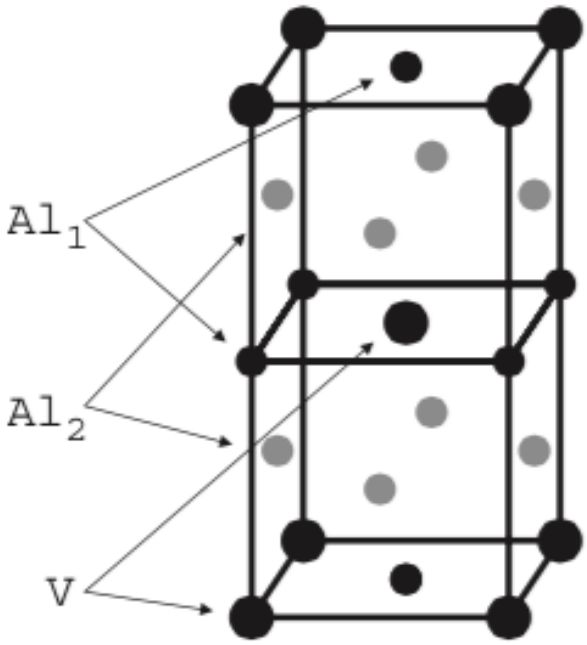

Figure 2.4 Lattice structure of Al_3V elementary cell with DO_{22} structure

© 2002 IOP Publishing Ltd
J. Phys.: Condens. Matter **14** (2002)

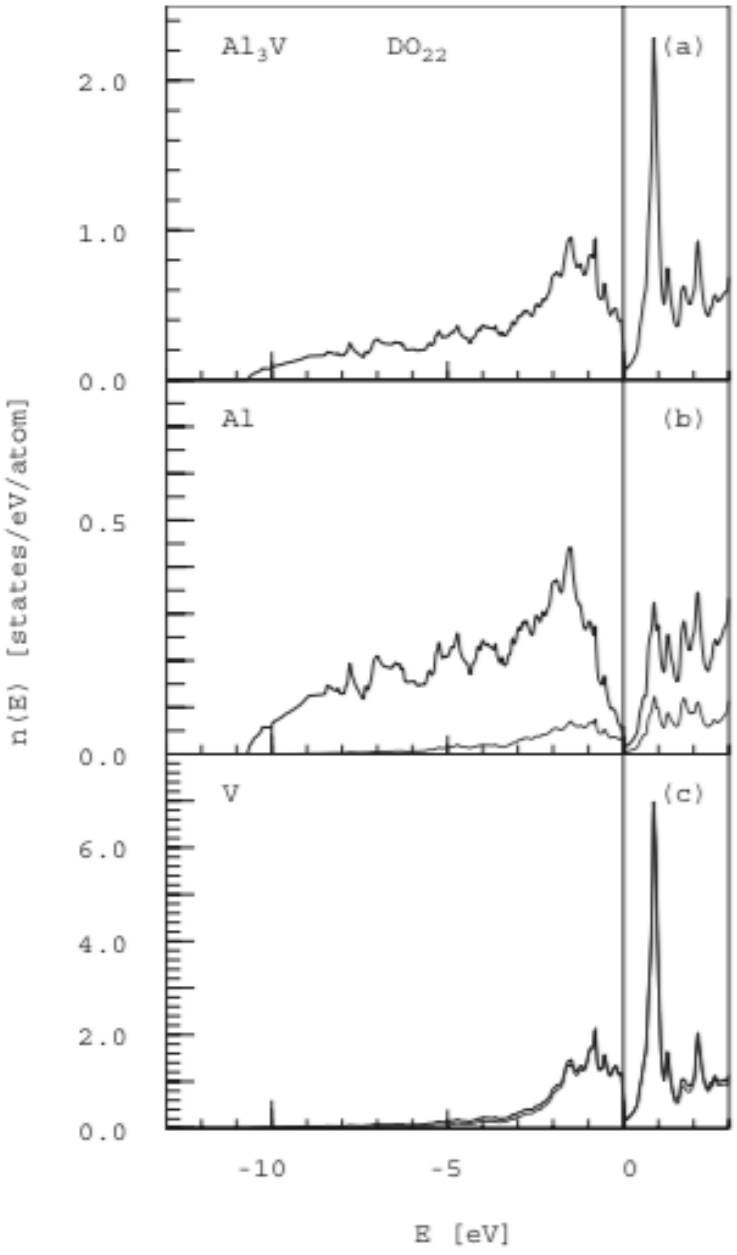

Figure 2.5 Density of states (DOS) of Al_3V with DO_{22} structure versus the energy of the orbital, and E=0 is set to Fermi level (a) Total DOS in the lattice, (b) DOS of Al, (c) DOS of V

© 2002 IOP Publishing Ltd
J. Phys.: Condens. Matter **14** (2002)

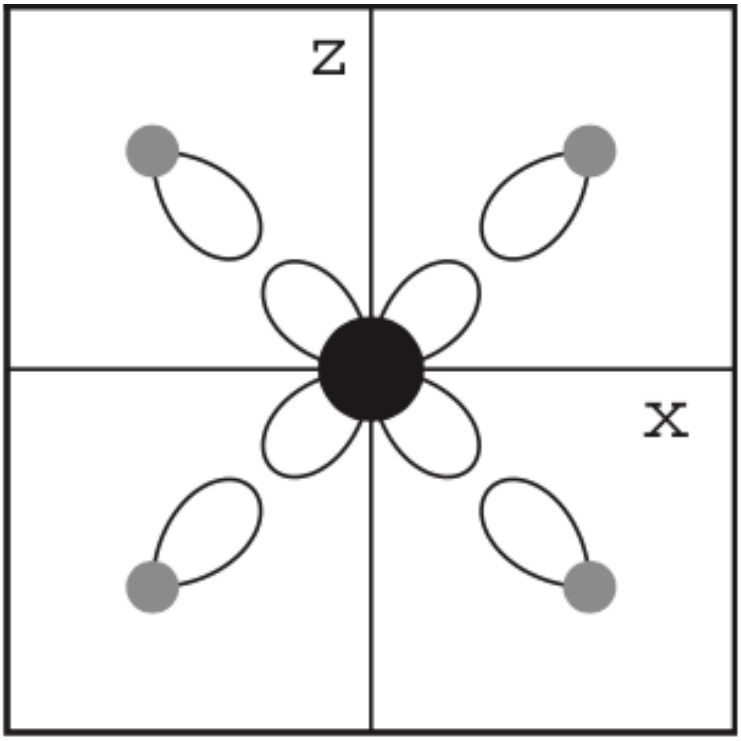

Figure 2.6 The atomic orbitals projection on x-z plane, the large black atom at the center is V atom and the small grey atoms at the corner are Al atoms

© 2002 IOP Publishing Ltd
J. Phys.: Condens. Matter **14** (2002)

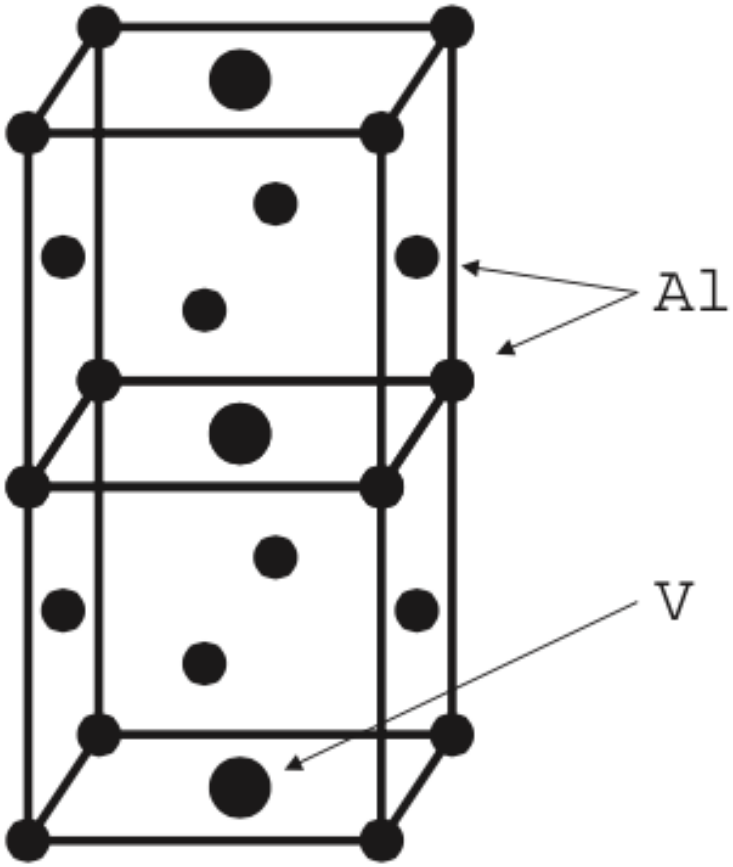

Figure 2.7 Lattice structures of two Al_3V elementary cells with $L1_2$ structure

© 2002 IOP Publishing Ltd
J. Phys.: Condens. Matter **14** (2002)

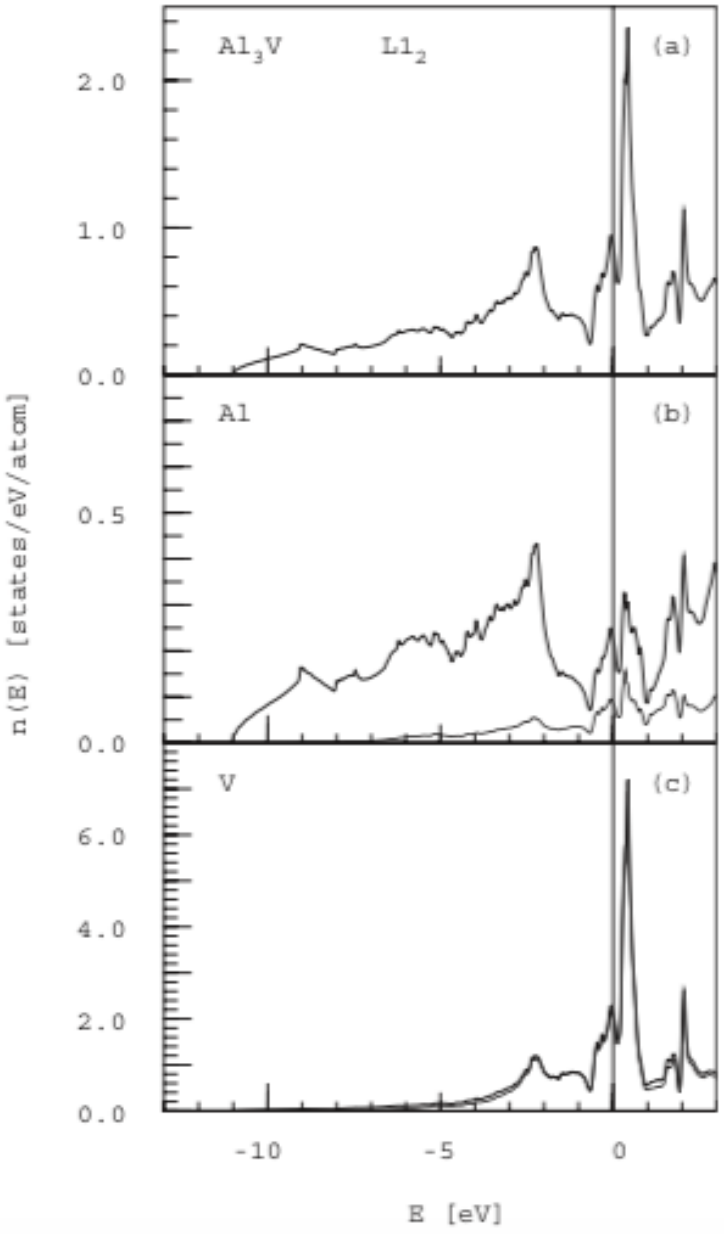

Fig. 2.8 Density of states (DOS) of Al_3V with $L1_2$ structure versus the energy of the orbital, and E=0 is set to Fermi level (a) Total DOS in the lattice, (b) DOS of Al, (c) DOS of V

© 2002 IOP Publishing Ltd
J. Phys.: Condens. Matter **14** (2002)

Chapter 3 Marker Design and Analysis for the IMC

3.1 Maker analysis in the intermetallic compounds

Figure 3.1(a) depicts the cross-section of an A-B diffusion couple with A_2B IMC in between and an array of markers placed on the IMC. Figure 3.1(b) depicts the growth of the IMC after annealing for a certain amount of time, and the markers have moved owing to the vacancy flux caused by the unbalancing flux between the diffusion of A atoms and B atoms. Every two A atoms travel across the IMC to B side can form one molecule of A_2B, contributing the growth of the IMC at the right side of the markers, which equals to $\Delta(x_2 - x_m)$. Similarly, every B atoms diffuse to A side can form one molecule of A_2B, contributing the growth of the IMC at the left side of the markers, which equals to $\Delta(x_m - x_1)$. If we ignore the molar volume change, we can have an equation related to the flux ratio as shown in equation 3.1. Noted that the factor of 2 and 1 in the equation may change if the composition of the IMC is different.

$$\frac{J_A}{J_B} = \frac{\Delta(x_2 - x_m)\times 2}{\Delta(x_m - x_1)} \qquad \text{--- (3.1)}$$

Along with the basic diffusion equations from Fick's 1st Law where D is intrinsic diffusivity,

$$J_A = -D_A \frac{\partial C_A}{\partial x} \quad \text{and} \quad J_B = -D_B \frac{\partial C_B}{\partial x} \qquad \text{--- (3.2)}$$

we can obtain the ratio of the diffusivity of A to the diffusivity of B in A_2B in equation 3.3. And now we know whether A atom or B atom is the faster diffusing species in the IMC on the basis of the ratio.

$$\frac{D_A}{D_B} = \frac{\Delta(x_2 - x_m)\times 2}{\Delta(x_m - x_1)} \quad \text{--- (3.3)}$$

3.2 Conventional marker designs

Marker experiments enable us to observe the faster diffusing species since marker will move in the opposite direction of the dominant diffusing atoms. The traditional way of marker study is to place inert metal wire at the interface of the diffusion couple. The most representative one is Kirkendall experiment [39], the Mo wires are put at the interfaces between pure Cu and Brass (Cu and Zn alloy) as shown in Fig. 3.2. When the interdiffusion occurs, Mo markers will move forward to the direction with the vacancy flux. However, the smallest diameter of the commercial wire is around 10 μm, but the intermetallic compound grows very slowly in solder joints and it might have crack formation [40] over 10 μm in thickness. Furthermore, there might be the dragging effect [41] that influences the diffusion of the atom (e.g, the growth of the IMC around the marker grows slower) if the marker dimension is too close to the IMC.

On the other hand, down to submicron level in thin film samples, people used inert gas particles as markers together with Rutherford backscattering technique to track them [42-43]. The inert gas marker is first used in observe the diffusion in metal silicide compound. Foe example, Ni thin film is first deposited onto Si substrate as shown in Fig. 3.3, and then Xe gas is implanted into the Si/Ni interface by calculating the appropriate implantation energy. The backscattering technique with

high-energy He^+ ions is used to observe the location in-depth of the Xe gas and the relative movement of the diffusion species can be determined as shown in Fig. 3.4. Nevertheless, the backscattering technique can only detect the atoms within 1 μm thickness and it is not easy to prepare thin film samples down to that dimension in solder joint cases. Thus, we need to develop a marker technique and experiment that fits the dimension for our diffusion couples.

3.3 Novel marker design by FIB milling

We developed the FIB marker technique that can be applied to 1-10 μm intermetallic compounds to achieve the marker analysis based on the marker analysis of IMC. The markers on the cross-sectional surface of the diffusion couples were made with the assistance of Focus Ion Beam (FIB). FIB uses finely focus Gallium ions beam at high current to sputter the materials away from the target as shown in Fig. 3.5.

The Focus Ion Beam was applied onto IMC layer and circular holes were created with diameter of 0.5 μm and depth around 5 μm as moving markers as shown in Fig. 3.6. There were also larger rectangular markers with 5 μm side length and 5 μm depth made away from the IMC side to serve as fixed markers in order to measure the movement of FIB markers on the IMC. To measure the growth contribution of the atoms, $\Delta(x_m - x_1)$ and $\Delta(x_2 - x_m)$, we treat the position of the center of the marker as x_m, the A/IMC and B/IMC interfaces are x_1 and x_2 respectively. Noted that

some IMC might not grow entirely smooth, we then use computer software to calculate the average length away from the x_m position through out the interface.

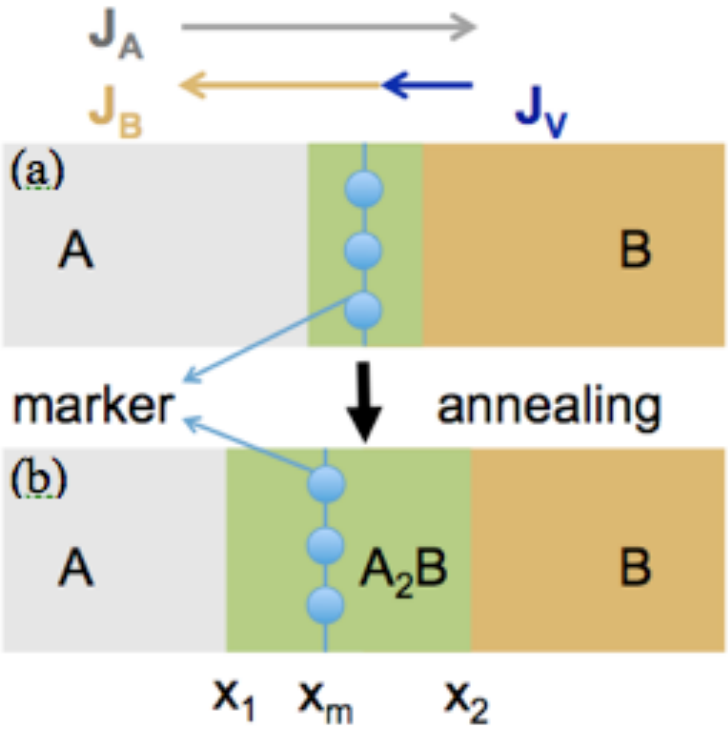

Figure 3.1 Schematic diagrams of A-B diffusion couple with the intermetallic compound and the markers in between (a) before annealing (b) after annealing

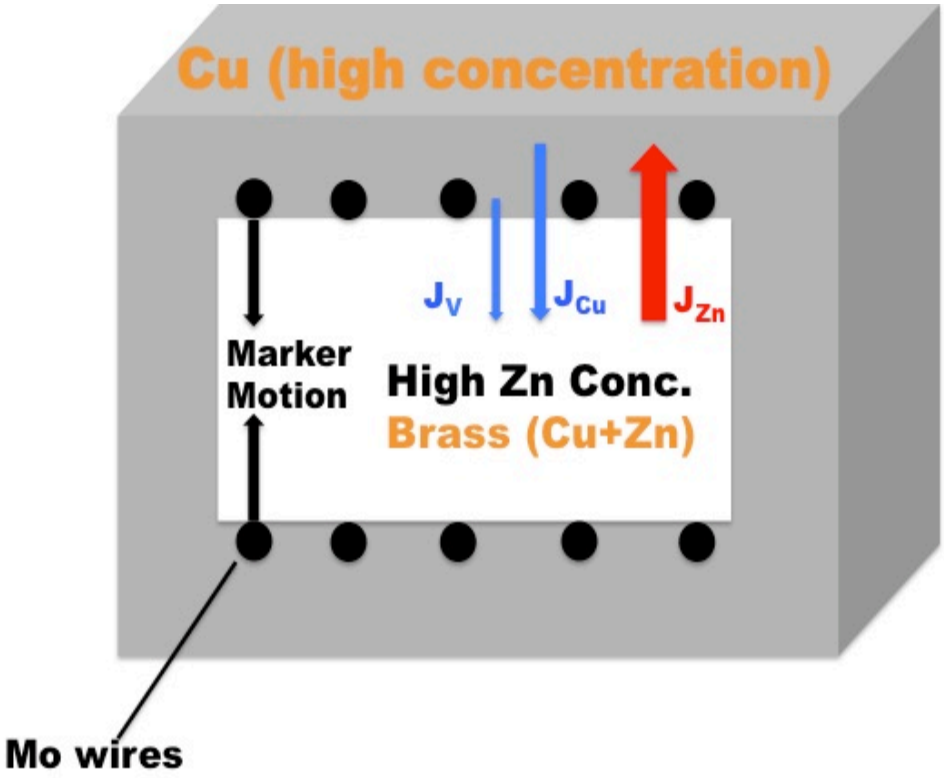

Figure 3.2 Schematic diagram of brass-pure Cu diffusion couple with the Mo markers in between, the markers move to the same direction as the vacancy flux

(Image from https://en.wikipedia.org/wiki/Kirkendall_effect)

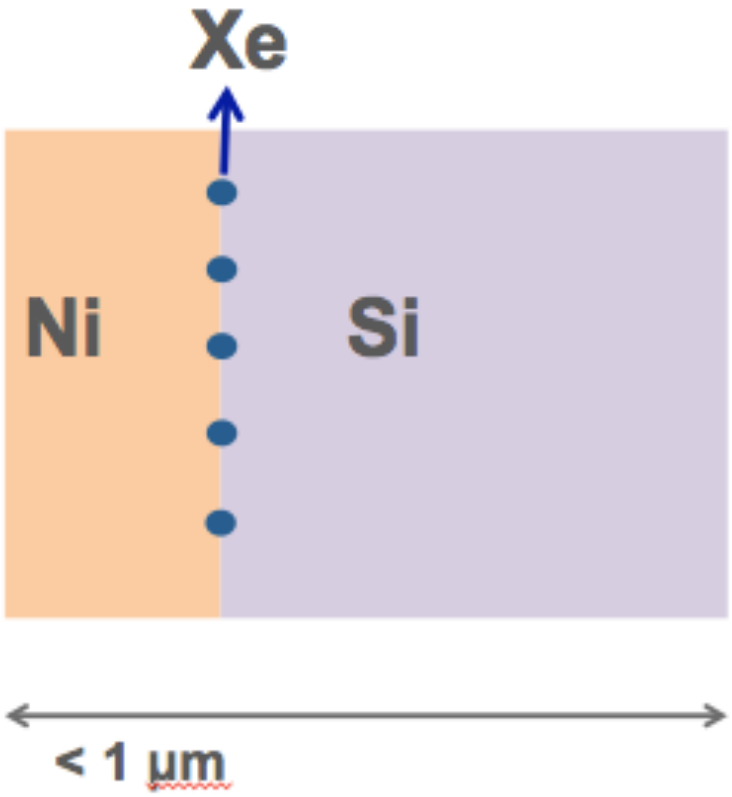

Figure 3.3 Schematic diagram of Ni thin film sputtered on Si substrate as diffusion couple, and the Xe gas bubbles are implanted in between as markers

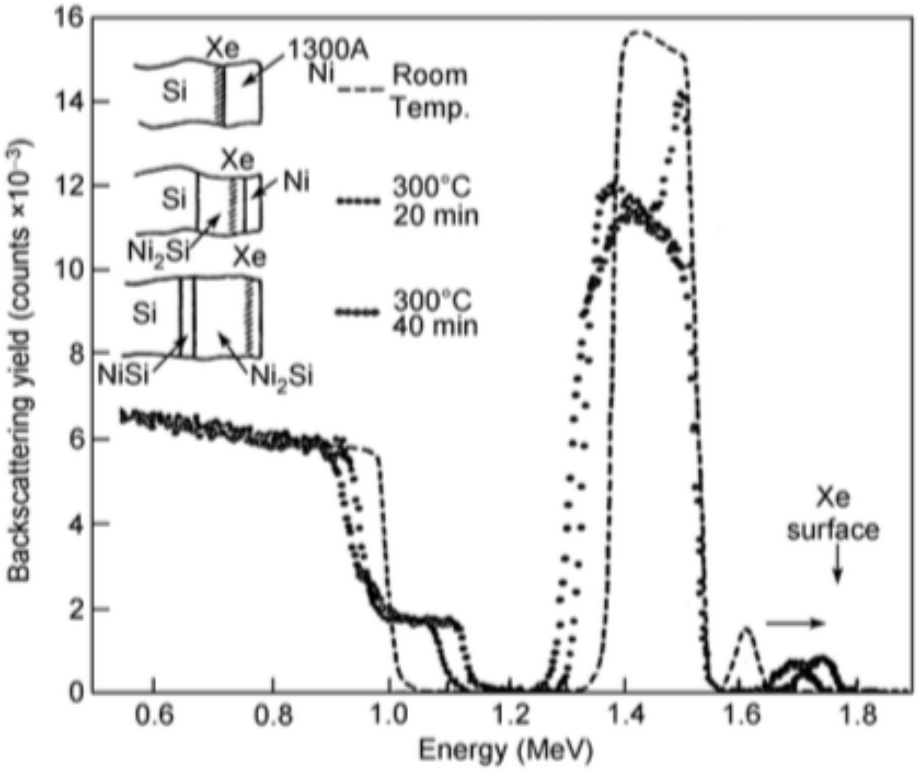

Figure 3.4 High-energy ion backscattering spectrum to detect the position of the Xe gas markers

© Science China Press and Springer-Verlag Berlin Heidelberg 2014

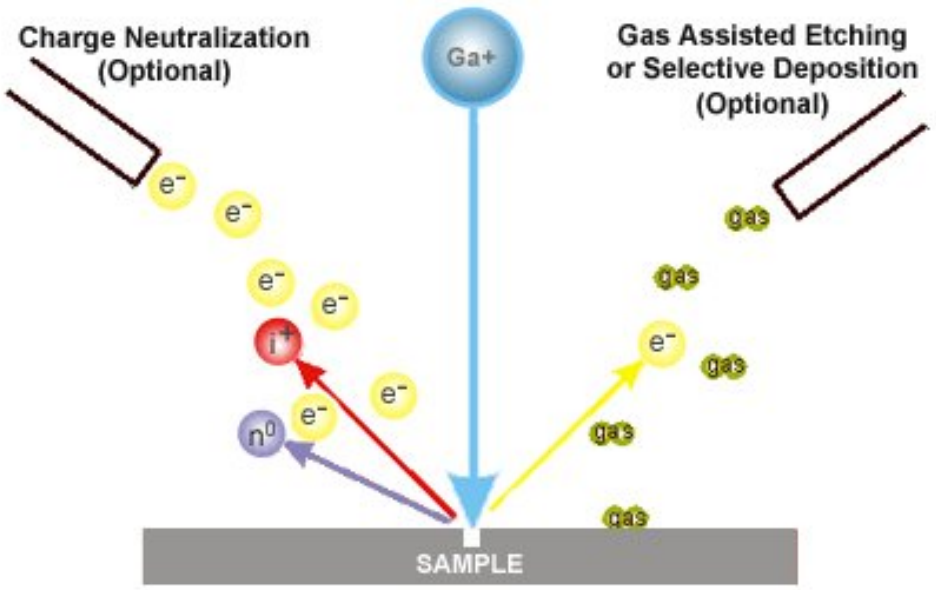

Figure 3.5 Focus ion beam sputtering using Gallium ion beam

(Image from http://www.wikiwand.com/en/Focused_ion_beam)

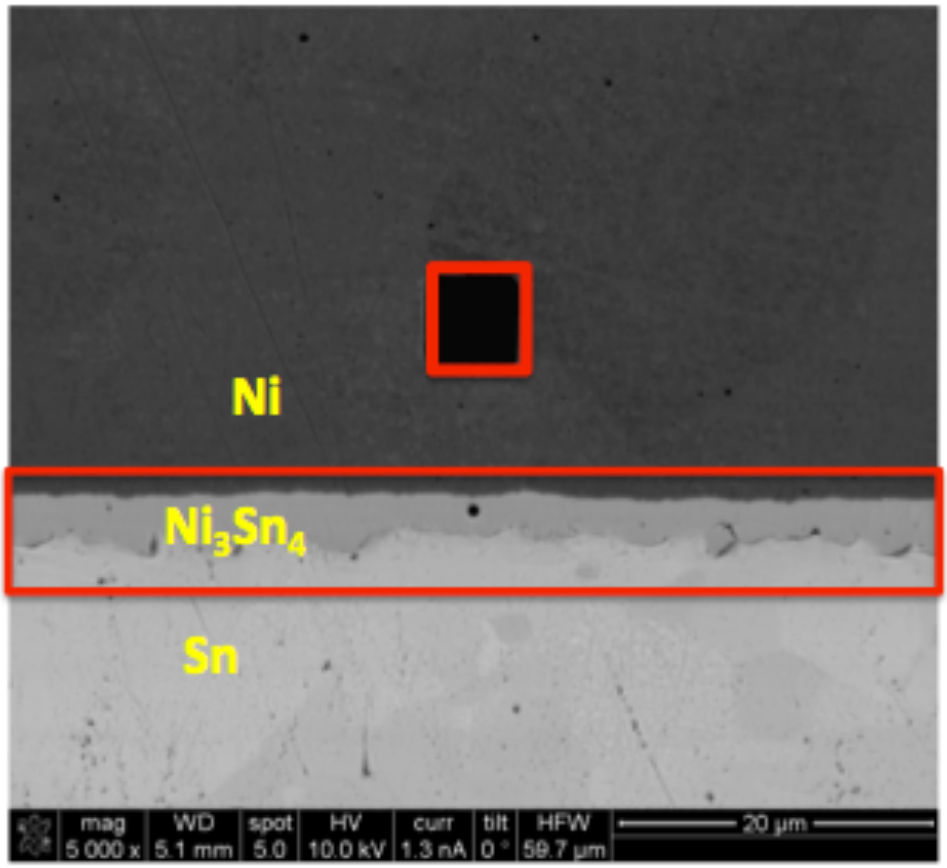

Figure 3.6 Ni/Ni_3Sn_4/Sn diffusion couple with a moving circular marker and a fixed rectangular marker

Chapter 4 Chemical Effect on Ni_3Sn_4 Intermetallic Compound

4.1 Sn-Ni intermetallic compounds

Tin and Nickel are common materials used in electronic packaging industry; Sn is used as solder joint and Ni is used as under bump metallization. During the liquid state reaction process in packaging, Sn will react with Ni and form intermetallic compound (IMC) to bond the chips onto the substrate. The IMC between them play a significant role in the reliability and electrical properties of the device, thus to know what types of the IMC formed is very important. According to Sn-Ni phase diagram shown in Fig. 4.1, we can see that there are three different kinds of intermetallic compounds may formed which are Ni_3Sn, Ni_3Sn_2 and Ni_3Sn_4. These three phases are all thermodynamically stable; however, at temperature below 260 °C with IMC layer less than 15 μm, only Ni_3Sn_4 is observed at the interface between Sn based solder and Ni under bump metallization [44-46]. It can be explained by the competitive growth of the intermetallic compounds in growth kinetics point of view.

The kinetics of the competitive growth is first proposed by Gosele and Tu [47] in 1981; but Gusak and Guror proposed the similar theory with different approach at almost the same time [48]. The competitive growth is owing to the interfacial reaction barrier under thin compound layer formation (usually below 10 μm); noted that there are two types of growth process to determine the kinetics of the growth of the compound layer, diffusion control and interfacial control. Diffusion control means that the diffusion of the atoms across the compound is the rate limiting process

for the compound growth, and the atomic diffusion flux decreases as the layer thickness increases; additionally, the layer thickness, x, increases proportional to the square root of time, t, ($x \propto \sqrt{t}$). On the other hand, interfacial control infers that the reaction or the rearrangement of the atoms at the interfaces involves reaction barrier that limit the rate of the compound growth, and the compound layer thickness increases linearly with time ($x \propto t$).

To correlate diffusion control and interfacial control to suppression of thermodynamically stable compound formation, we first consider the simplest situation in Fig. 4.2. We have three compounds, $A_\alpha B$ (α phase), $A_\beta B$ (β phase) and $A_\gamma B$ (γ phase), where α > β > γ; if we take α = 1 and γ = 0, then the left side will be pure A and the right side will be pure B. The dash line in Fig. 4.2 represents the concentration of A at the interfaces in $A_\beta B$ without the interfacial reaction barrier while the solid line means the concentration of A at the interfaces with the concentration barrier. From Kidson's derivation [49], we can get:

$$\left(C_{\alpha\beta}^{eq} - C_{\beta\alpha}\right)\frac{dx_{\alpha\beta}}{dt} = \tilde{D}_\beta\left(\frac{dC_\beta}{dx}\right)_{\alpha\beta} \qquad \text{--- (4.1)}$$

$$\left(C_{\beta\gamma} - C_{\beta\alpha}^{eq}\right)\frac{dx_{\beta\gamma}}{dt} = -\tilde{D}_\beta\left(\frac{dC_\beta}{dx}\right)_{\beta\gamma} \qquad \text{--- (4.2)}$$

where C_β is the concentration of A in β phase and $\tilde{D}_\beta$ is the interdiffusion coefficient in β phase. By assuming steady state diffusion and the interface-only compound formation, we can obtain the atomic diffusion flux of A in $A_\beta B$:

$$J_\beta = -\tilde{D}_\beta\frac{C_{\beta\alpha} - C_{\beta\gamma}}{x_\beta} \qquad \text{--- (4.3)}$$

The flux J_β can also impressed with respect to reaction constant $\kappa_{\alpha\beta}$ and $\kappa_{\beta\gamma}$ at the to interfaces as:

$$J_\beta = \kappa_{\beta\alpha}\left(C^{eq}_{\beta\alpha} - C_{\beta\alpha}\right) = \kappa_{\beta\gamma}\left(C_{\beta\gamma} - C^{eq}_{\beta\gamma}\right) \quad \text{--- (4.4)}$$

Combining equation 4.3 and equation 4.4 with the expression of time-independent value $\Delta C^{eq}_\beta = C^{eq}_{\beta\alpha} - C^{eq}_{\beta\gamma}$ we can have:

$$J_\beta = \Delta C^{eq}_\beta \kappa^{eff}_\beta / \left(1 + x_\beta \kappa^{eff}_\beta / \tilde{D}_\beta\right) \quad \text{--- (4.5)}$$

where κ^{eff}_β is the effective interfacial reaction barrier in $A_\beta B$ and can be expressed as $1/\kappa^{eff}_\beta = 1/\kappa^{eff}_\beta + 1/\kappa^{eff}_\beta$. Finally, we can combine equation 4.1, 4.2 and 4.5 to obtain the growth rate of $A_\beta B$ layer, x_β as:

$$\frac{dx_\beta}{dt} = \left(\frac{1}{C^{eq}_{\alpha\beta} - C_{\beta\alpha}} + \frac{1}{C_{\beta\gamma} - C^{eq}_{\gamma\beta}}\right)\Delta C^{eq}_\beta \kappa^{eff}_\beta / \left(1 + \frac{x_\beta \kappa^{eff}_\beta}{\tilde{D}_\beta}\right)$$

$$\frac{dx_\beta}{dt} = G_B \Delta C^{eq}_\beta \kappa^{eff}_\beta / \left(1 + x_\beta \frac{\kappa^{eff}_\beta}{\tilde{D}_\beta}\right) \quad \text{--- (4.6)}$$

where G_B is a constant. We now assume a critical thickness $x^*_\beta = \tilde{D}_\beta / \kappa^{eff}_\beta$, and from equation 4.6, we can obtain the relations:

$$\frac{dx_\beta}{dt} \approx G_B \Delta C^{eq}_\beta \kappa^{eff}, \text{ for } x_\beta << x^*_\beta \quad \text{--- (4.7a)}$$

$$\frac{dx_\beta}{dt} \approx \frac{G_B \Delta C^{eq}_\beta \tilde{D}_\beta}{x_\beta}, \text{ for } x_\beta >> x^*_\beta \quad \text{--- (4.7b)}$$

If we integrate both sides, we can observe:

$$x_\beta \propto t, \text{ for } x_\beta << x^*_\beta$$
$$x_\beta \propto t^2, \text{ for } x_\beta << x^*_\beta \quad \text{--- (4.8)}$$

This infers that when the compound thickness is much less than the critical thickness (just begin to grow), the growth of the compound is governed by interfacial reaction

control. However, when the thickness of the compound layer is large enough, the growth mechanism will be changed to diffusion control.

We should now consider a model with two intermediate compound layer growths in between two saturated layers as shown in Fig. 4.3. We have $A_\alpha B$ (α phase), $A_\beta B$ (β phase), $A_\gamma B$ (γ phase) and $A_\delta B$ (δ phase), and we would like to observe the growth behavior of $A_\beta B$ and $A_\gamma B$, assuming that the thickness of $A_\alpha B$ and $A_\delta B$ are infinite large. Following the similar derivation in previous discussion, we can obtain the variation of the thickness of $A_\beta B$ layer and $A_\gamma B$ layer with time t:

$$\frac{dx_\beta}{dt} = G_\beta J_\beta - G_{\beta\gamma} J_\gamma \qquad \text{--- (4.9a)}$$

$$\frac{dx_\gamma}{dt} = G_\gamma J_\gamma - G_{\gamma\beta} J_\beta \qquad \text{--- (4.9b)}$$

where G_β, $G_{\beta\gamma}$, $G_{\gamma\beta}$, and G_γ are some constants determined by the value of α, β, γ and δ. Additionally, J_β and J_γ are the flux of A atoms in $A_\beta B$ layer and $A_\gamma B$ layer. In order to have $A_\beta B$ layer grow, we need to have $\frac{dx_\beta}{dt} > 0$; and we can express the consition in the ratio r to see a clearer picture.

$$r = \frac{J_\beta}{J_\gamma} \qquad \text{--- (4.10)}$$

From equation 4.9a, $A_\beta B$ grow when $\frac{dx_\beta}{dt} > 0$; and this is equals to:

$$r > \frac{G_{\beta\gamma}}{G_\beta} = r_1 \qquad \text{--- (4.11a)}$$

Similarly, for the growth of $A_\gamma B$ layer, we have:

$$r < \frac{G_\gamma}{G_{\gamma\beta}} = r_2 \qquad \text{--- (4.11b)}$$

We can see that $A_\beta B$ layer and $A_\gamma B$ layer can both grow only when $r_1 < r < r_2$; if $r > r_2$, then $A_\beta B$ layer can grow but $A_\gamma B$ layer will shrink; similarly, if $r > r_2$, then $A_\gamma B$ layer can grow but $A_\beta B$ layer will shrink. We can summarize the effect that $A_\beta B$ layer and $A_\gamma B$ layer may shrink or grow with various r values in Fig. 4.4.

In the case of Ni-Sn system, we start from pure Ni and pure Sn; which means the thickness of the compounds are zero, much less than the critical thickness. When the interdiffusion begins, certain intermetallic compounds may grow depending on the flux ratios. The flux ratios will keep constant until the compound reaches the critical thickness because it is interfacial reaction control when $x << x^*$. After the certain compound reaches the critical thickness, the flux ratio will change and it will result in other compounds formation as shown in Fig. 4.5. Back to Ni-Sn system, owing to the fact that r value lies at the Ni_3Sn_4 growth-only region and it does not reach its critical thickness, we only observe this phase in electronic packaging and the research of our solder alloy system.

4.2 Experimental procedure

The diffusion couples of Ni and Sn were made through liquid state reaction process. The commercial Ni (99.9%) sheets with 1mm thickness were served as substrate and cut by diamond-saw machine to 1 cm^2 pieces and then well polished through alumina colloid with particle size less than 0.05 μm. The Ni substrates were then put into ultrasonic bath with DI water and acetone to clean the surface. During the liquid state reaction process, the Ni substrates were heated up to 260 $^\circ$C on a hot

plate and then 2 ml flux was dropped onto the substrate to remove the native oxide layers; then a pure tiny Sn solder ball was placed onto the Ni substrate to react for 60 seconds. The solder ball wetted and reacted with the substrate immediately and formed a hemisphere cap. After the wetting process, the solder cap sample was put into ultrasonic bath with DI water and acetone to clean up the flux residues, then annealed at 190 $^{\circ}$C for 1 day to enable the ensuing steady state of solid-state reaction to form a planar Ni_3Sn_4 IMC. Finally, the solder cap sample was polished vertically to expose the cross-section of Sn-Ni_3Sn_4-Ni interface.

The markers on the cross-section surface were made with FIB, using a finely focus Gallium ions beam at a high current for sputtering. The FIB was applied to the IMC layer and circular holes were created to serve as moving markers with depth around 3 μm. Also there were larger rectangular markers made on the Ni side to serve as fixed markers in order to measure the movement of markers on the IMC. After the markers have been placed on the diffusion couples, the diffusion couples were annealed at 150, 170, 190 and 210^{o}C for different periods to observe the IMC growth and the marker motion.

To characterize the IMC, back-scattered electron (BSE) microscope and dispersive X-ray spectroscopy (EDX) are used. The cross sections of each diffusion couple after placing markers and after annealing at different times and temperatures were lightly polished for measuring the thickness of IMC by BSE and for confirming the composition by EDX. For measuring the IMC thickness, the average height of Ni_3Sn_4 perpendicular to Ni sheet is calculated by the software called ImageJ from BSE image. Moreover, to analyze the microstructure of the IMC, the cross-section

samples after the pre-annealing and after the final annealing were polished by colloidal polishing solution for additional 30 minutes to reveal the clear grain microstructure. Additionally, plan-view samples were also prepared to see the morphology of Ni_3Sn_4; the samples were first polished to remove most of the unreacted tin, and then dipped into 10 vol. % hydrochloric acid and 90 vol. % methanol for 20 hours to remove the unreacted tin.

To examine the chemical interaction between Ni and Sn atoms in Ni3Sn4 lattice, X-ray photoelectron spectroscopy (AXIS Ultra DLD) was used to measure the chemical shift of core electrons' bonding energy for Ni atoms and Sn atoms. Besides, the Ni_3Sn_4 lattice model was constructed by VESTA software with the FIZ Karlsruhe ICSD database. Furthermore, the atomic vibrational pattern and the atomic outer shell electron energy were simulated by First principle model.

4.3 *Microstructure of Ni_3Sn_4* intermetallic compound

Microstructure plays an important role in atomic diffusion. The grain size and morphology may determine the path of atomic diffusion. For example, the growth of scallop-type Cu_6Sn_5 IMC in liquid state solder reaction has time exponent n = 0.33 because the presence of fast diffusion channel between scallops, while a layer- type Cu_6Sn_5 has time exponent n = 0.5 in solid state reaction. Furthermore, using different substrates, different solder materials and different reaction times might also cause the formation of various microstructures of IMC. Thus we have examined the microstructure of Ni_3Sn_4 to confirm the diffusion path of the atoms. It has been

reported that Ni_3Sn_4 has elongated, rod-like shape with fast diffusion channels between them [50]. This kind of microstructure may affect the solid-state diffusion due to the existence of fast diffusion paths. Therefore, the diffusion couples in this study were undergone 1 day annealing at 190^{o}C right after wetting in order to reach a steady state of solid-state diffusion. The cross section of the diffusion couples after one day annealing at 190^{o}C is shown in Fig. 4.6; the top is the bulk Ni while the bottom is the bulk Sn. Additionally, the middle layer is Ni_3Sn_4, which is identified by EDX and XRD (Fig. 4.7). Moreover, we can see that the IMC layer is flat and compact, and there is no apparent channels appeared in the plan-view of the Ni_3Sn_4 as shown in Fig. 4.8. In the samples, the shapes of the densely compacted polygons are displayed. The BSE picture in Fig. 4.9 demonstrates the grains of Ni_3Sn_4; there is an obvious grain size distribution with a gradient of larger grains at Sn side and small grains at Ni side. At the Ni/IMC interface, the grains tend to nucleate, and the grains at Sn/IMC interface tend to grow. During the solid-state reaction, Sn atoms diffuse to Ni side and nucleate IMC grains at Ni side, while the grains that formed earlier are pushed towards to Sn side and have grown slowly accompanied by ripening [51]. On the other hand, Ni atoms diffuse to Sn side and let the grains at the interface grow larger. This behavior causes the special microstructure having a grain size gradient of Ni_3Sn_4.

4.4 *Solid-state growth of Ni_3Sn_4* intermetallic compound

In order to measure the layer-type growth of Ni_3Sn_4 with high accuracy, the moving markers were always centered when taking their SEM images. The purpose is

to measure the thickness of the same sets of Ni_3Sn_4 grains at different times, thus we can eliminate the original thickness variation of Ni_3Sn_4 and obtain the precise growth profile of Ni_3Sn_4. The growth profile of Ni_3Sn_4 IMC is shown in Fig. 4.10 at several temperatures. The growth of Ni_3Sn_4 meets solid-state diffusion model [52] very well with the coefficient of determination (R^2) of linear regression around 0.99 and the time exponent is 0.5.

Additionally, the linear regression slope of the data at 210 ^oC, 190 ^oC, 170 ^oC and 150 ^oC are 1, 0.2, 0.03, 0.007 μm^2/hour respectively. Noted that the growth rate drops very fast (~ 10^2) from 210 ^oC to 150 ^oC; it took only few hours to observe the growth of Ni_3Sn_4 at 210 ^oC, but it took a few days for annealing at 150 ^oC to do so. Furthermore, Fig. 4.11 shows the logarithm of the growth rate versus the reverse temperature and we can measure the activation energy of Ni_3Sn_4 growth from the slope. The activation energy of Ni_3Sn_4 growth in this study is 140 kJ/mole, which matches the results from previous reports [53-54]. Noted that there are other groups reported a different value of diffusion activation energy for Ni_3Sn_4, yet the time exponents of them were between 0.3 - 0.5 [55-56]; which suggests they might not be in steady state of solid-state diffusion.

4.5 Marker analysis

There are two kinds of markers presents in the diffusion couples as shown in Fig. 4.12; one is square marker on Ni and the other is circular marker on Ni_3Sn_4. The square markers are fixed because they are not involved in the interdiffusion of the two

species and the circular markers tend to move with the IMC growth. We can locate the center of both markers and observe the relative motion between them, so that we can determine the moving direction of circular markers as well as the velocity of motion. Once we know them, the fast diffusion species in IMC under certain temperature can be determined. Moreover, the circular marker can also be considered as the reference point of Sn and Ni diffusion as we discussed before.

The results of the marker experiment annealing at 210^{o}C is shown in Fig. 4.12, we can see that the circular marker moved towards Sn side clearly, which suggests that there are net vacancies moved toward the Sn side. That is to say, there are more Sn atoms traveling through the IMC to the other side than the opposite Ni atoms. Noted that the moving marker shrinks a little bit from time to time, this is because the aspect ratio of the circular hole is large so that focus ion beam cannot sputter away IMC efficiently; the bottom material cannot fly away and accumulate at the wall, causing the shape tapered toward the bottom like a circular cone instead of a circular pillar. Furthermore, since the sample was polished after different annealing time to avoid the effect of surface diffusion, the circular marker seems getting smaller. Nevertheless, the center of the circle is always the same, thus we can use the center as the marker's position. Fig. 4.13 and Fig. 4.14 also show that the circular marker moved toward Sn side, thus Sn is also the dominant diffusion species when annealing at 190^{o}C and 170^{o}C. However, the marker motion is not obvious at 150^{o}C as shown in Fig. 4.15 because the diffusion rate is too slow to allow enough marker motion to occur.

A horizontal line is drawn across the center of the moving marker and the ratio of diffusion of Sn atoms and Ni atoms can be determined by measuring the IMC growth above and below the horizontal line; that is to say, the growth of Ni_3Sn_4 above the line is contributed to the Sn diffusion while the IMC below is contributed to the Ni diffusion. Moreover, the ratio needs to be adjusted by multiplying some constants owing to the fact that three Ni atoms traveling across the marker to Sn/Ni_3Sn_4 interface can form one molecule of Ni_3Sn_4 and four Sn atoms traveling across the marker to Ni/Ni_3Sn_4 interface can form one molecule of Ni_3Sn_4. The results are presented in Table 1, and it shows that Sn atoms diffused faster than Ni atoms from 210 ^{o}C to 150 ^{o}C; the ratios at 210 ^{o}C, 190 ^{o}C, 170 ^{o}C and 150 ^{o}C are 6±1, 3.9±0.7, 1.9±0.3 and 1.5±0.2 respectively.

4.6 Tracer diffusivities of Sn and Ni in Ni_3Sn_4

To remove the chemical effect so that we can calculate the tracer diffusivities, we recall the two equations in chapter 2 and modify them to fit our system as:

$$slope = \frac{x_t^2 - x_0^2}{t} = 2\frac{1}{(1-X_{Ni})X_{Ni}}(X_{Ni}D_{Sn}^{*} + X_{Sn}D_{Ni}^{*})\frac{\Delta g_t}{kT} \qquad \text{--- (4.12)}$$

$$\frac{D_{Ni}^{*}}{D_{Sn}^{*}} = \frac{3\Delta(x_2 - x_m)}{4\Delta(x_m - x_1)} \qquad \text{--- (4.13)}$$

we take X_{Ni}=3/7, X_{Sn}=4/7 in and put all the values into equation 4.12 and equation 4.13 such as slopes, ratio at different temperatures from our analysis earlier. The formation energy of IMC per atom can be acquired from published paper [57], which is equal to 25 kJ/mol. The tracer diffusivities of Sn and Ni in Ni_3Sn_4 at several

temperatures are shown in Table 1. We can plot the tracer diffusivities of Sn and Ni versus the reverse temperature in Fig. 4.16 and obtain the activation enthalpy of diffusion for Ni and Sn in Ni_3Sn_4, which are 120 and 150 kJ/mole, respectively. The activation enthalpy of diffusion for Ni is smaller than Sn, and it suggests that the diffusion pre-factor for Sn is much larger than that of Ni in Ni_3Sn_4 because Sn is the dominant diffusion species in this temperature region. Additionally, we can also obtain the diffusion pre-factor from extrapolate of the curve, and we know that the diffusion pre-factor of Sn is at the order of 10^4 larger than the diffusion pre-factor of Ni. For discussion, we shall examine below the crystal structure of Ni_3Sn_4.

4.7 Crystal structure of monoclinic Ni_3Sn_4

In Fig 4.17, we present the complex C-centered monoclinic crystal structure of Ni_3Sn_4, which is reported in the literature [58-59]. In the lattice, it contains two crystallographically independent Sn sites and two crystallographically independent Ni sites. Additionally, Sn atoms tend to have more abnormal and open structure in the lattice, as shown in Fig. 4.18(a) to 4.18(e), where Sn1 is bonded to 5 Ni atoms at one side with one Sn1 atom and 2 Sn2 atoms at the other side while Sn2 is bonded to 5 Ni atoms, 2 Sn1 atoms and 2 Sn2 atoms. On the other hand, Ni atoms are packed more condensed in the lattice; Ni1 is bonded to six Sn atoms with the traditional octahedral coordination while Ni2 is bonded to 7 Sn atoms and 2 Ni2 atoms with complicated polyhedral coordination. In other words, Ni atoms on the average have 6.5 Ni-Sn bonds and 1 Ni-Ni bond, and Sn atoms have on the average 5 Ni-Sn bonds and 3.5 Sn-Sn bonds. This suggests that the bonding strength of Ni atoms in Ni_3Sn_4 lattice is

higher than Sn atoms because Sn-Ni bond is stronger than Sn-Sn bond and Ni-Ni bond. In turn, it indicates the diffusion of Ni is harder than that of Sn.

To illustrate the higher activation enthalpy of diffusion for Sn atoms, we can decompose the calculated activation enthalpy into two terms, the activation enthalpy of formation of vacancies and activation enthalpy of atomic motion, due to the fact that the diffusion inside Ni_3Sn_4 is substitutional diffusion. Although Sn atoms are less closed-packed than Ni atoms, the volume of Sn atom is twice larger than that of Ni atom; which leads to a larger lattice distortion while moving inside the lattice. Thus, the activation enthalpy of motion for Sn atoms is higher than Ni atoms. On the other hand, formation enthalpy of vacancies is related to the binding energy of the atoms and how the surrounding atoms reposition themselves. It seems that it is harder to remove a Ni atom to form a vacancy because it has higher binding energy; however, it is smaller and locked in an octahedral position so that there is less energy increase to the system for the lattice reposition. On the other hand, the energy may increase a lot more when an Sn atom is removed to form a vacancy. For example, Sn1 has highly unsymmetrical bonding with three Sn atoms on one side and 5 Ni atoms on the other side. If a vacancy formed at Sn1 position, all the surrounding atoms will lose the brace and the total energy of the lattice will be increased. With the result of the experiment in this study, it is concluded that the enthalpy of atomic motion outweighs the enthalpy of vacancy formation, and results in higher activation enthalpy of diffusion for Sn atoms.

Even though Sn has higher activation enthalpy in diffusion, it is the dominant diffusion species in temperature region from 150 ^{o}C to 210 ^{o}C. This implies that the

prefactor in diffusivity of Sn is much higher than that of Ni. If we extrapolate the lines in Fig. 4.16, we can obtain the pre-factor of diffusion for Sn and Ni atoms in Ni_3Sn_4, D_{0Sn} and D_{0Ni}, and D_{0Sn} is about the order of 10^4 larger than D_{0Ni}. To understand more about this large difference between the diffusion pre-factors of Ni and Sn in Ni_3Sn_4, we need to take a deeper look into diffusion pre-factor. Diffusion pre-factor consists of three parts as shown in equation 4.14:

$$D_0 = \delta^2 f \nu n \exp(\frac{\Delta S}{k}) \quad \text{--- (4.14)}$$

They are jump distance (δ), jump correlation factor (*f*), jump frequency (ν), number of nearest neighbors (n), and entropy change (ΔS) [60]. The lattice distance is almost the same, the nearest Ni for Ni1 is 283pm and Ni2 is 255pm; while the nearest Sn for Sn1 and Sn2 are 285pm and 309pm respectively. Jump correlation factor is considered approaching 1 for Ni and Sn atoms if they jump to their own sublattices sites [60]. However, there might be chances that they jump to the sublattice of other atoms. It is relatively hard for Sn jumping to a Ni position because Sn is 50 % larger and the Ni position is very compact. On the other hand, the possibility for Ni jumping to Sn position is high and it seems that there are more moving paths for Ni. However, Ni is not stable at the location of Sn because the strong Sn-Ni bonds will be replaced by the weaker Ni-Ni bonds; this is also called antistructural disorder [61-62] and the atoms jump reverse to the original position immediately when it happened, resulting in extremely small (~0) correlation factor for this type of jumping. Therefore, we don't need to consider the situation where atoms jump from "right" sublattice to "wrong" sublattice.

The jumping frequency for pure metals is usually at the order of 10^{13} Hz; for example, the Debye frequency [63] is 4.31×10^{13} Hz for pure Sn and 9.88×10^{13} Hz for

pure Ni. In intermetallic compound, Sn atoms and Ni atoms are mostly bonded to foreign atoms (Ni and Sn respectively); moreover, atomic vibration pattern has lots to do with surrounding atoms. Therefore, we expect that the vibrational (jump) frequency for Sn and Ni in Ni_3Sn_4 will not vary a lot because their vibration should be correlated. We can see the possible vibrational frequencies in Ni_3Sn_4 from first principle simulation in Fig. 4.19, all the vibrational frequencies (modes) have their correspondent Sn and Ni atoms, thus we can suggest that vibrational frequency for Sn and Ni in Ni_3Sn_4 are very close.

On the number of nearest neighbors, the difference between an atom of Sn and Ni is not big. Finally, on entropy change, we believe the disorder induced by the diffusion of an atom of Sn is much larger than that of the diffusion of a Ni atom due to the fact that Sn atom is much larger than Ni atom. The entropy change for solid-state diffusion is normally less than $10k_B$, and the entropy term is inside and the exponential term; if ΔS is $7k_B$, the influence on diffusion pre-factor will be 10^3. Therefore, the entropy change in diffusion is believed to be the most phenomenal factor causing the large diffusion pre-factor difference between Ni and Sn in Ni_3Sn_4. The chemical effects on diffusion in Ni_3Sn_4 are summarized in Table 2.

4.8 *XPS analysis and Simulation of the Energy of Outer Electrons of Atoms*

The interactions between outer electrons of Sn and Ni atoms cause the chemical effect between atoms. The bonding stronger than metallic bond such as covalent bond is expected between two foreign atoms in intermetallic to release large

amount of energy during intermetallic compound formation. The outer electrons of both Sn and Ni atoms are expected to share the same orbitals; moreover, the outer orbital for Ni atom is 4s and for Sn atom is 5p, since they have different energy level, they are expected to form hybrid orbital like sp^3 or sp^2 hybrid orbitals to have the same orbital energy for the electrons.

We did XPS characterization on pure Ni, pure Sn and Ni_3Sn_4 IMC in order to understand the chemical interactions between Ni and Sn atoms. For instance, when Ni forms NiO_2, the O atom will attract the outer electrons from Ni atom due to the larger electronegativity; this makes bonding change for Ni atom in transforming from metallic bonding to ionic bonding. If there is a chemical shift for an element between pure material and compound, we expect that there is electrons redistribution; hence it will influence the bonding behavior. The influence of electron redistribution on chemical shift varies from element to element; for example, there is only less than 0.2 eV shift for Sn in SnO and SnO_2 [64]. Yet, on the other hand, the chemical shift for NiO and NiO_2 is 2 eV [65]. Since the effect of chemical shift on Ni atom is much larger than Sn atoms, plus the fact that the electronegativity difference between Ni and Sn is very small (only 0.1), thus we should focus on the XPS result on Ni element.

From Fig. 4.20, we can see the binding energy of Ni 2p electrons for Ni in pure Ni and in Ni_3Sn_4. The result of two peaks is due to spin orbital splitting effect; the right peak stands for $2p_{1/2}$ and the left peak stands for $2p_{3/2}$. By comparing the two peaks for pure Ni and Ni_3Sn_4, we observe that there is no obvious chemical shift between pure Ni and Ni_3Sn_4; however, we can observe the difference and the shift of

satellite peaks for both $2p_{1/2}$ and $2p_{3/2}$. This suggests that the states of Ni ion in pure Ni and Ni_3Sn_4 are different due to the change of surrounding atoms and bonds.

To know more about the energy of outer shells of atoms, First-principles calculation was used to simulate the atomic orbital energies around Fermi-level in Ni_3Sn_4 intermetallic compound. The outer atomic orbitals of Ni and Sn are expressed by the diagrams of density of state (DOS) versus energy (set E=0 at Fermi level) as shown in Fig. 4.21 and Fig. 4.22.

After comparing different atomic orbitals in Ni atom and Sn atom, we found that Sn 5d orbital and Ni 4s orbital are correlated as shown in Fig. 4.23. The upper curve represents the Sn 5d electrons and the lower curve represents the Ni 4s electrons. We can see that they have the similar pattern; the orbitals are across Fermi level (E=0) and there are two peaks on each side (E>0, E<0) which represents the bonding and anti-bonding behavior with a shallow gap at the Fermi level.

This implies the similar behavior of hybrid bond with the bonding (E<0) and anti-bonding (E>0) as we discussed in chapter 2; that is to say, the outer electrons of Ni and Sn atoms are in the same hybrid orbital and this is the chemical effect of Ni and Sn atoms in Ni_3Sn_4 intermetallic compound. Since the orbitals are only half filled and crossed Fermi-level, the electron can contribute to the electrical conduction; moreover, the hybrid bonding property caused the bonding directional and may contribute to the brittle behavior of the Ni_3Sn_4 IMC. Furthermore, owing to the fact that hybrid bond has covalent bond property, which makes Ni-Sn bond stronger than

pure metallic Sn-Sn and Ni-Ni bond, results in a large decrease in Gibbs free energy when forming Ni_3Sn_4.

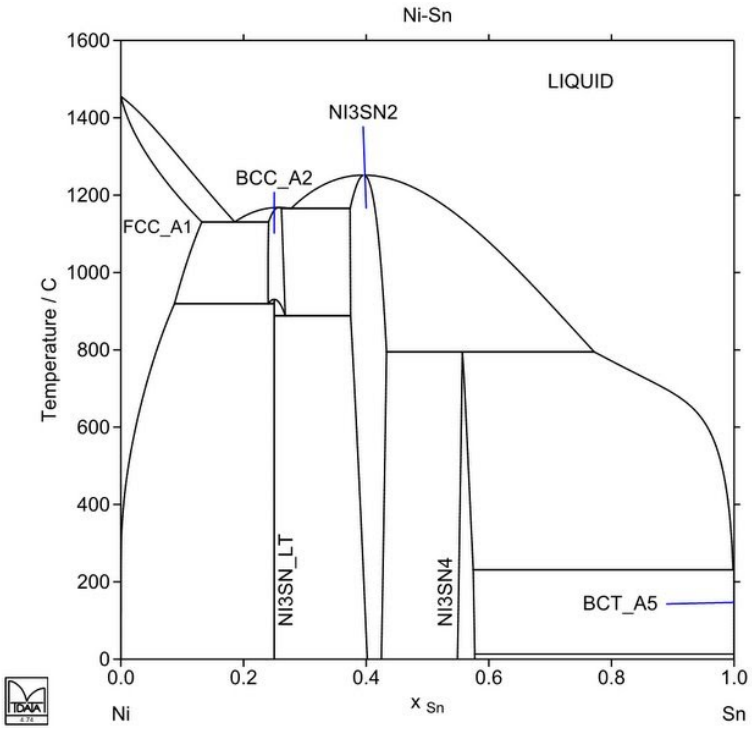

Figure 4.1 Phase diagram of Sn-Ni binary system

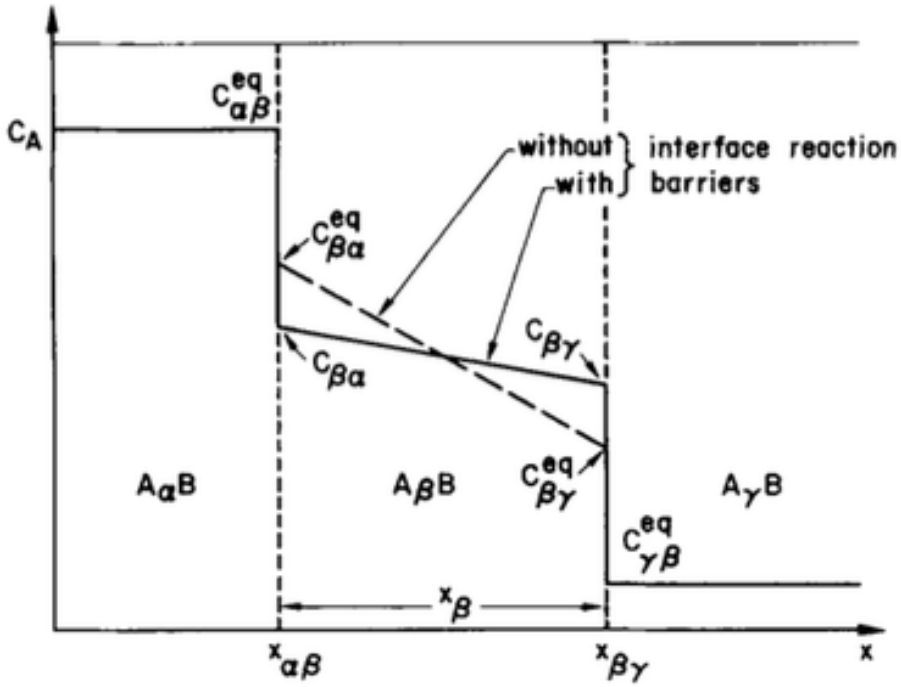

Figure 4.2 Concentration of A atoms along the $A_\alpha B/A_\beta B/A_\gamma B$ diffusion couple

© 1982 American Institute of Physics
J, AppL Phys. 53(4), April 1982

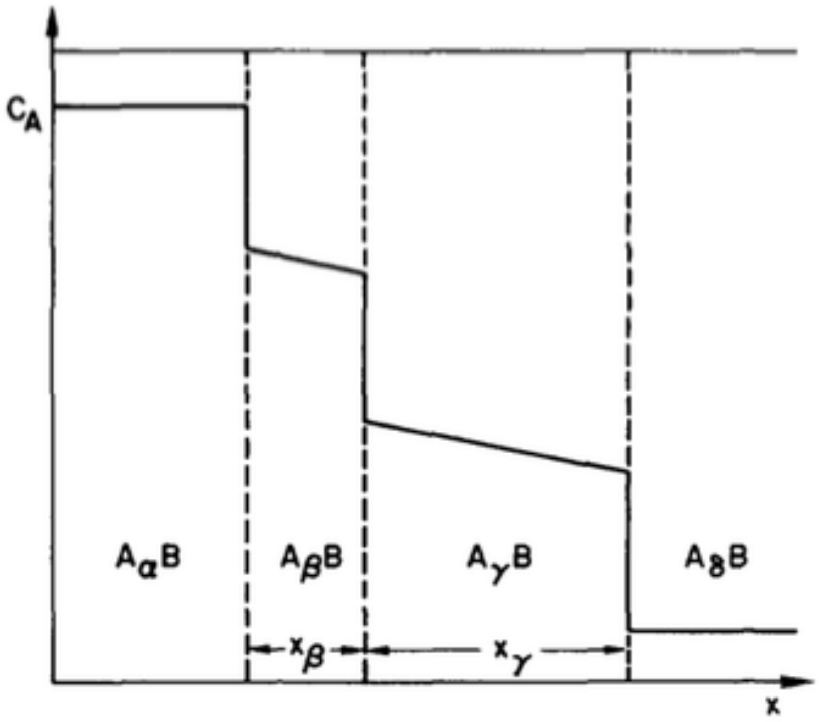

Figure 4.3 Concentration of A atoms along the $A_\alpha B/A_\beta B/A_\gamma B/A_\delta B$ diffusion couple

© 1982 American Institute of Physics
J, AppL Phys. 53(4), April 1982

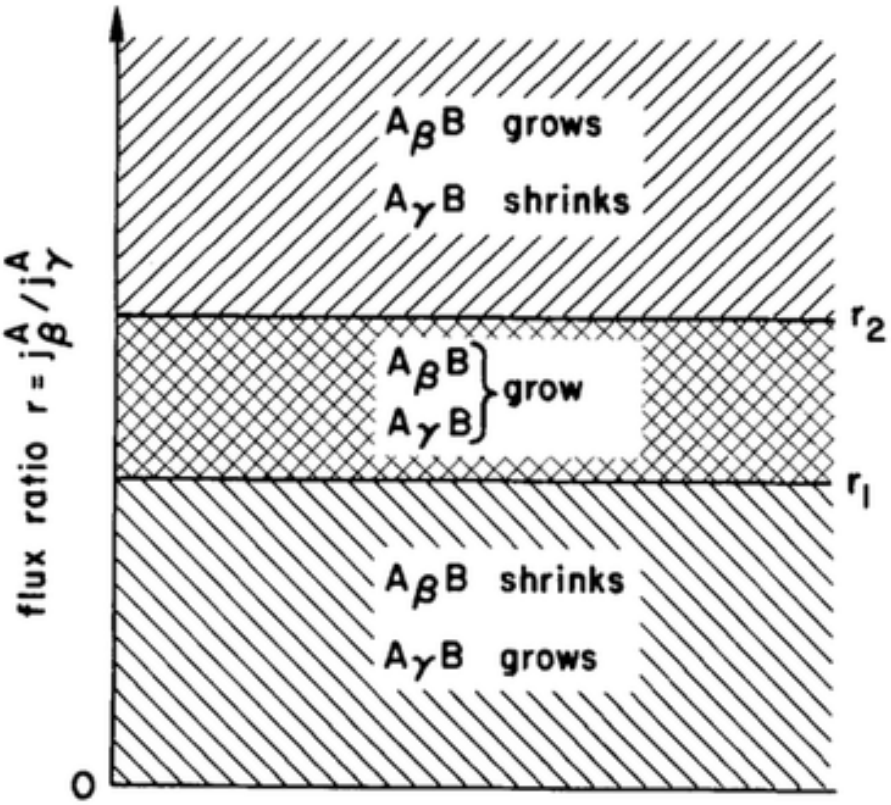

Figure 4.4 Compound growth behaviors with different r value

© 1982 American Institute of Physics
J, AppL Phys. 53(4), April 1982

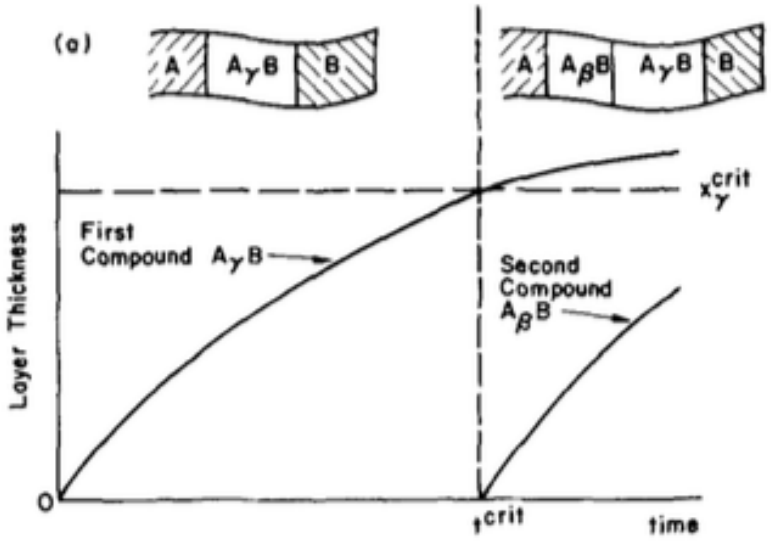

Figure 4.5 Schematic diagram of competitive compounds growth with time

© 1982 American Institute of Physics
J, AppL Phys. 53(4), April 1982

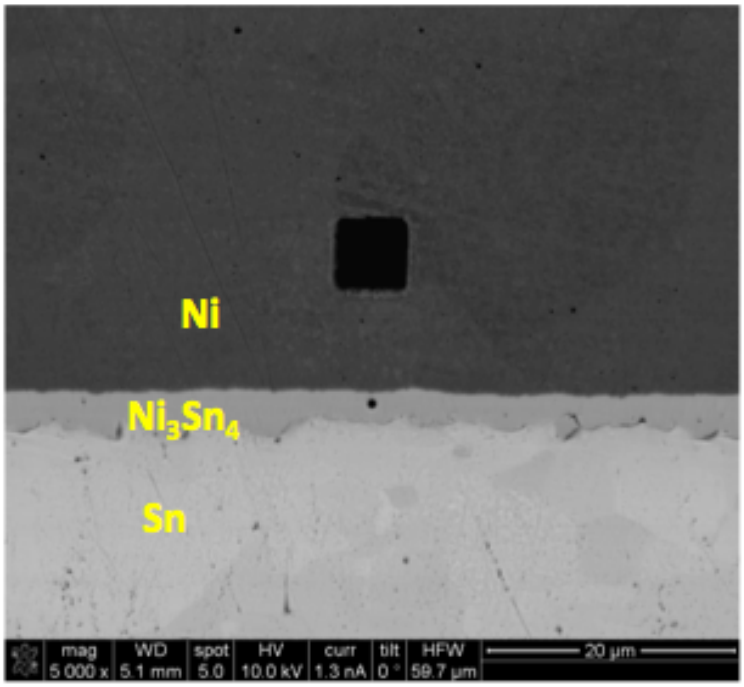

Figure 4.6 BSE image of the cross section of Ni/Ni_3Sn_4/Ni diffusion couple

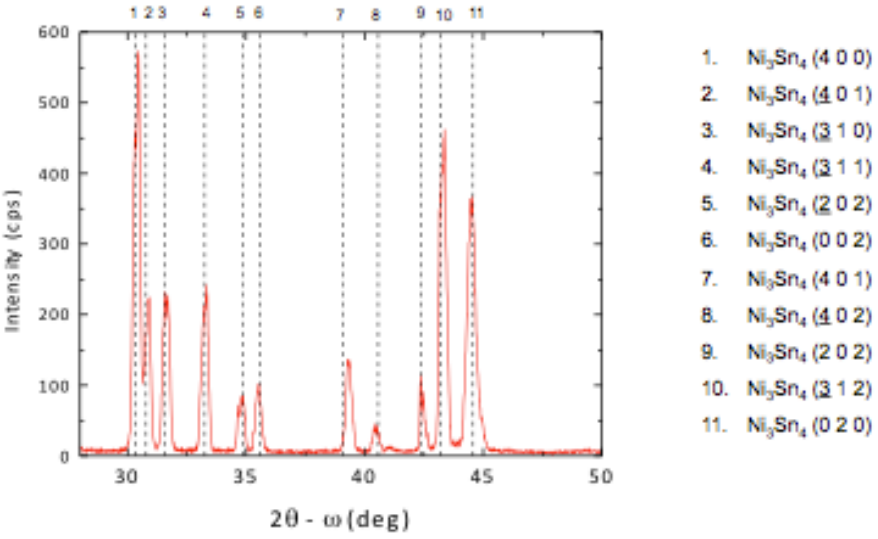

Figure 4.7 XRD characterization of Ni_3Sn_4 layer

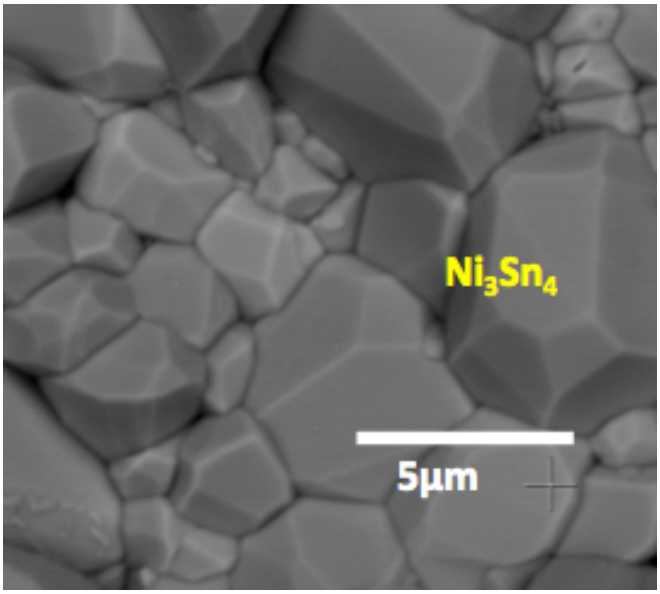

Figure 4.8 BSE image of the top-down view of the Ni_3Sn_4 in the diffusion couple (Sn has been etched away)

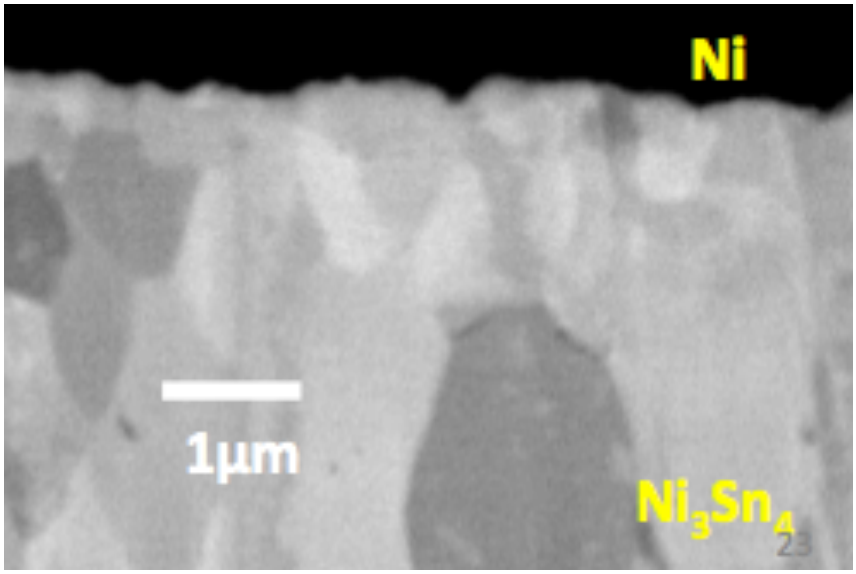

Figure 4.9 BSE image of the Ni_3Sn_4 grains in the diffusion couple, which shows grain size gradient

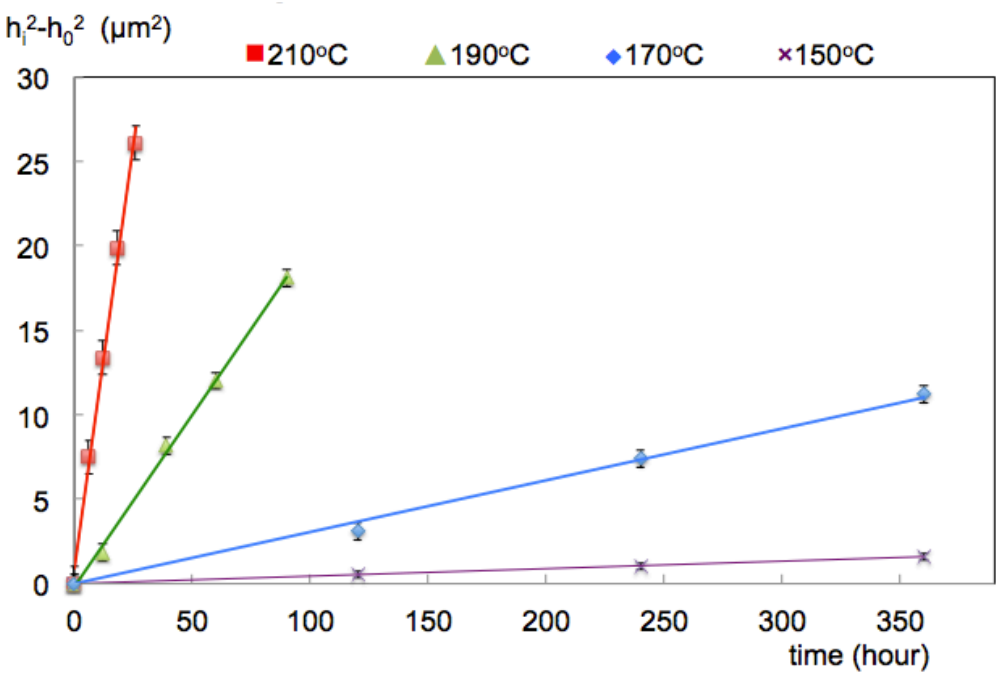

Figure 4.10 Growth profiles of the diffusion couples, the x-axis is time (hour) and the y-axis is the square difference of IMC thickness

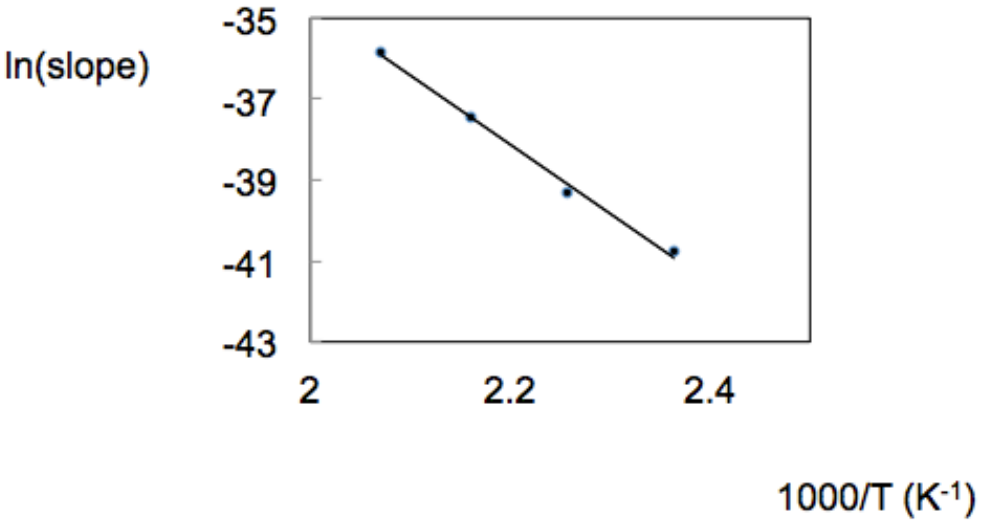

Figure 4.11 Logarithm of growth slope of the diffusion couples versus the reverse temperature

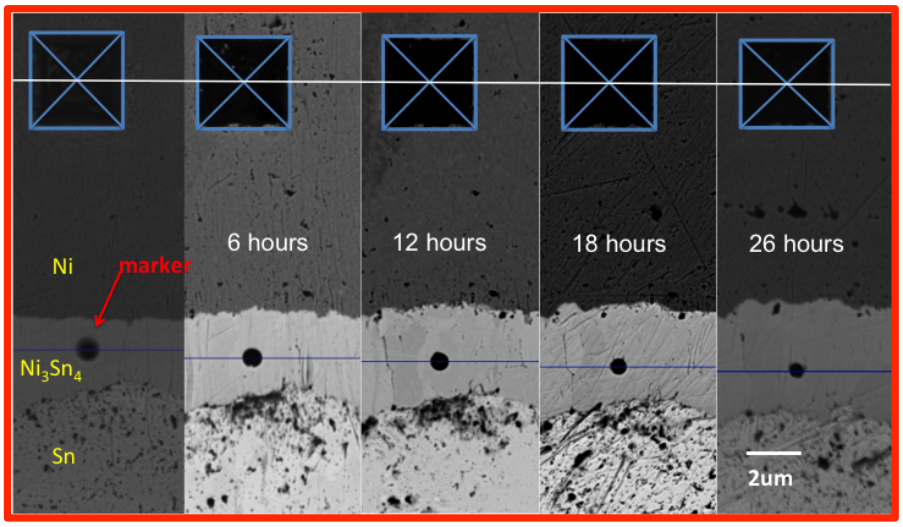

Figure 4.12 Marker analysis on Ni/Ni_3Sn_4/Sn diffusion couple annealed at 210 °C

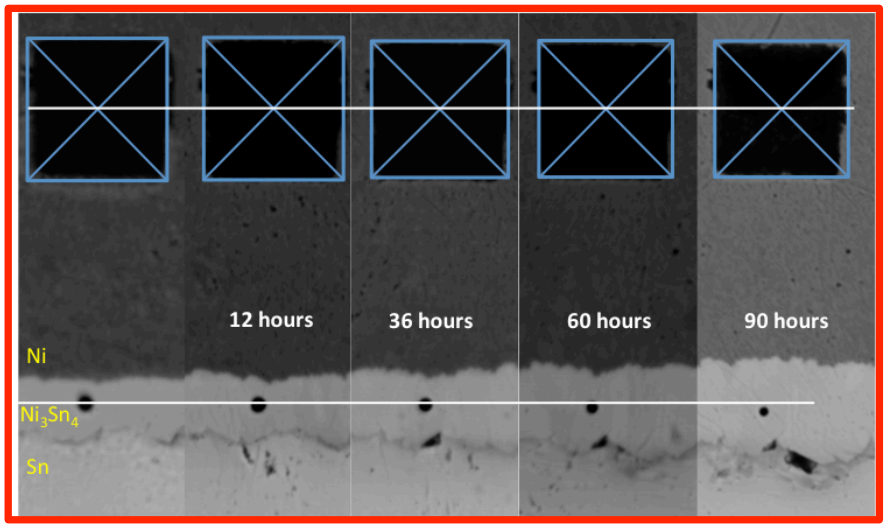

Figure 4.13 Marker analysis on Ni/Ni_3Sn_4/Sn diffusion couple annealed at 190 °C

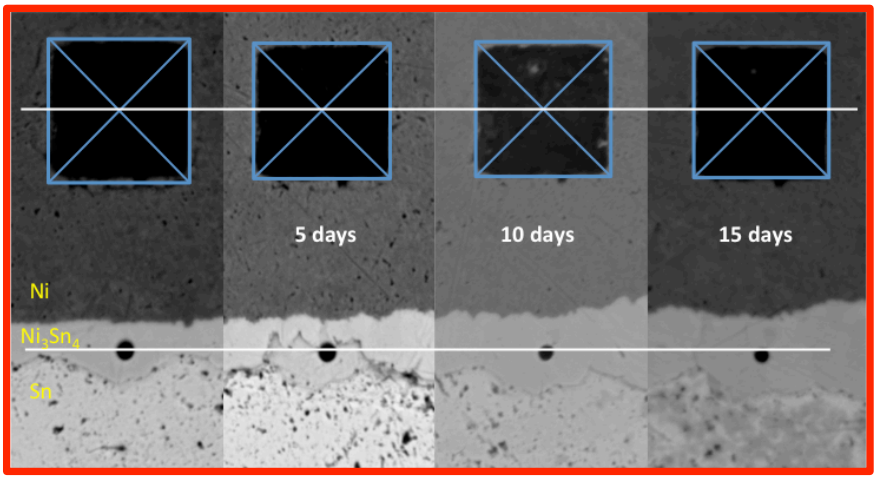

Figure 4.14 Marker analysis on Ni/Ni_3Sn_4/Sn diffusion couple annealed at 170 °C

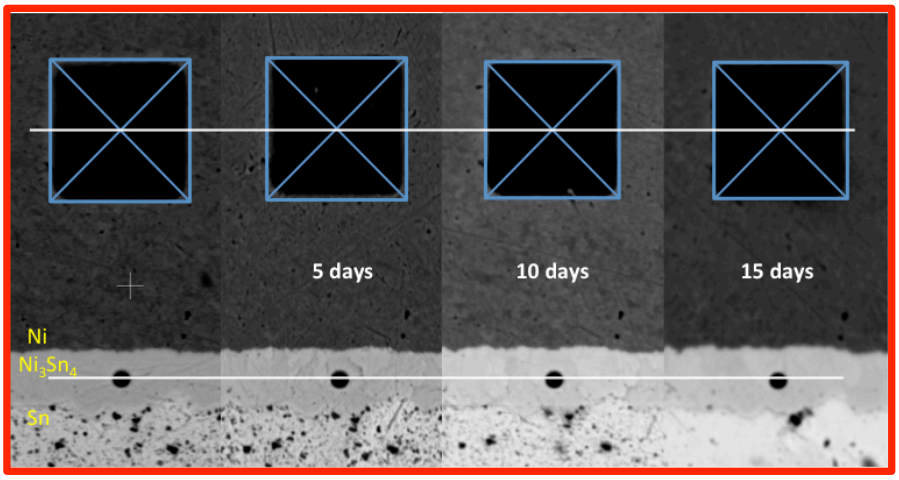

Figure 4.15 Marker analysis on $Ni/Ni_3Sn_4/Sn$ diffusion couple annealed at 150 °C

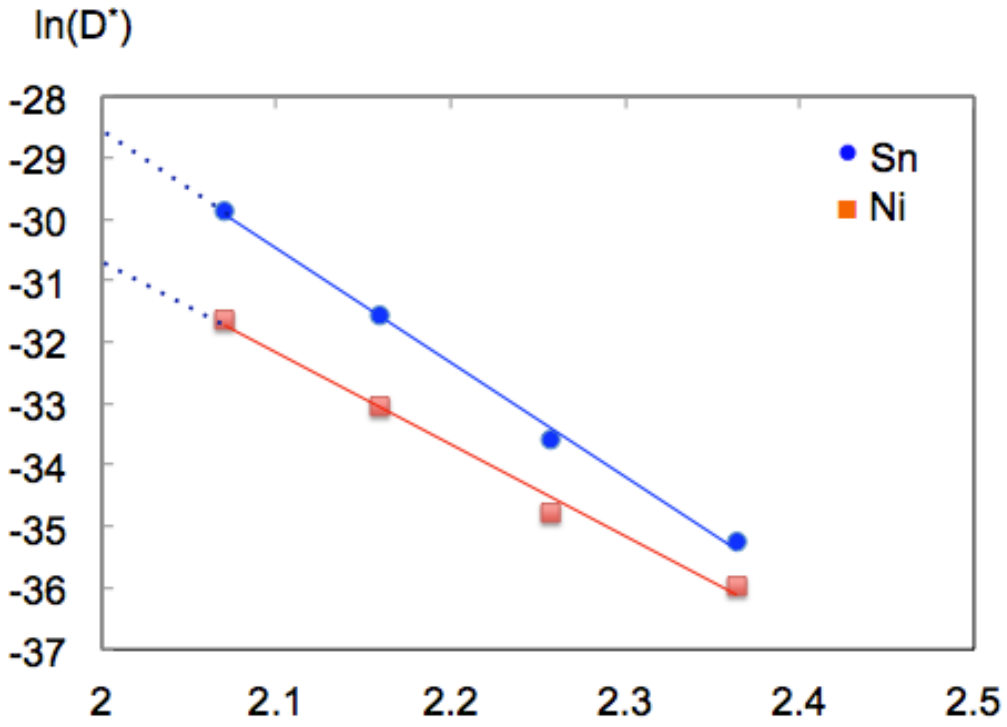

Figure 4.16 Logarithm of the tracer diffusivities of Ni and Sn in Ni_3Sn_4 versus the reverse temperature

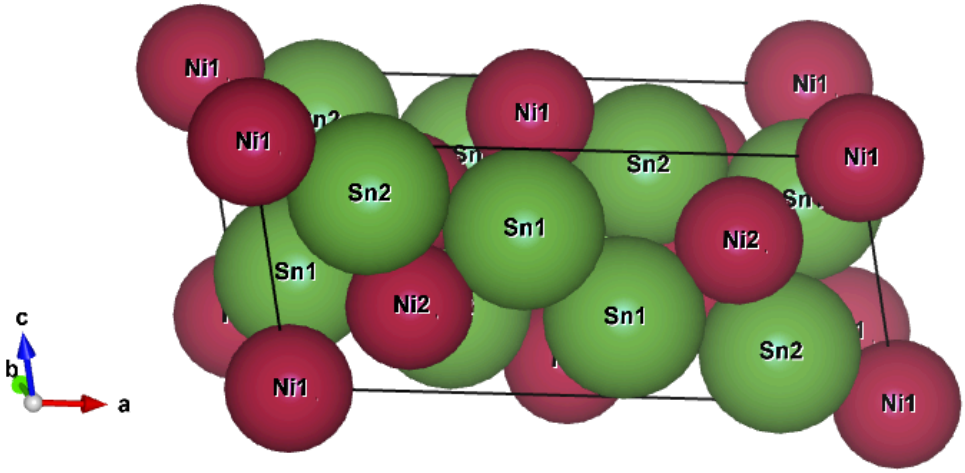

Figure 4.17 The lattice structure of monoclinic Ni_3Sn_4

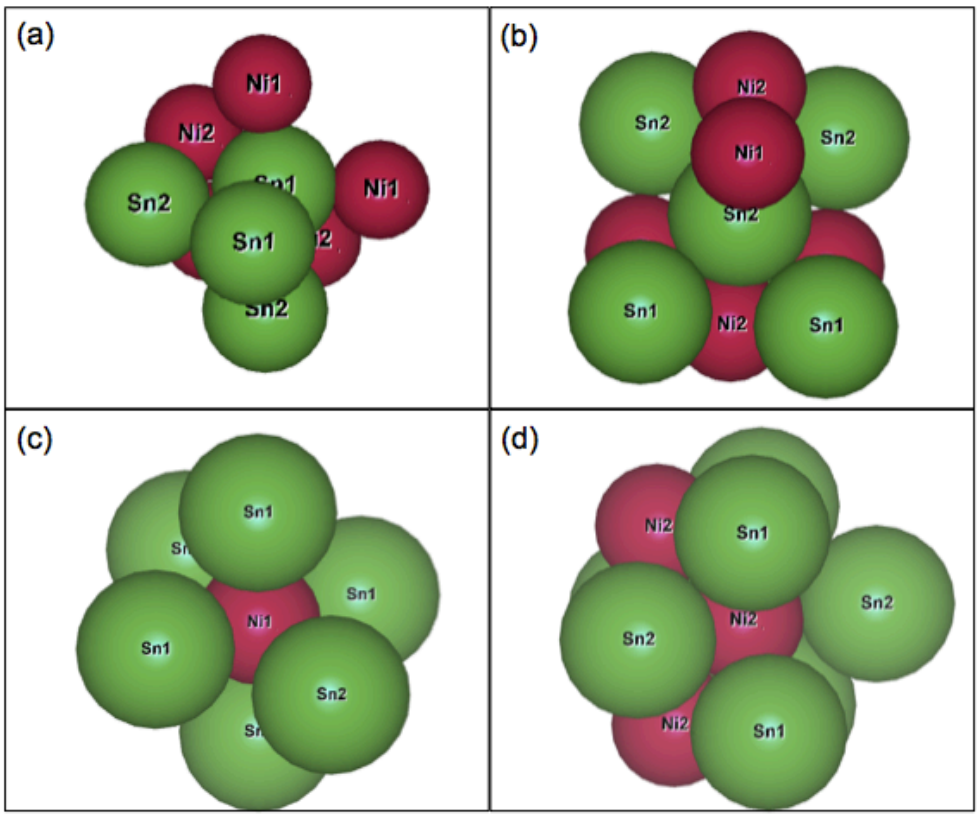

Figure 4.18 Atomic bonding of (a) Sn1 atom (b) Sn2 atom (c) Ni1 atom (d) Ni2 atom in Ni_3Sn_4

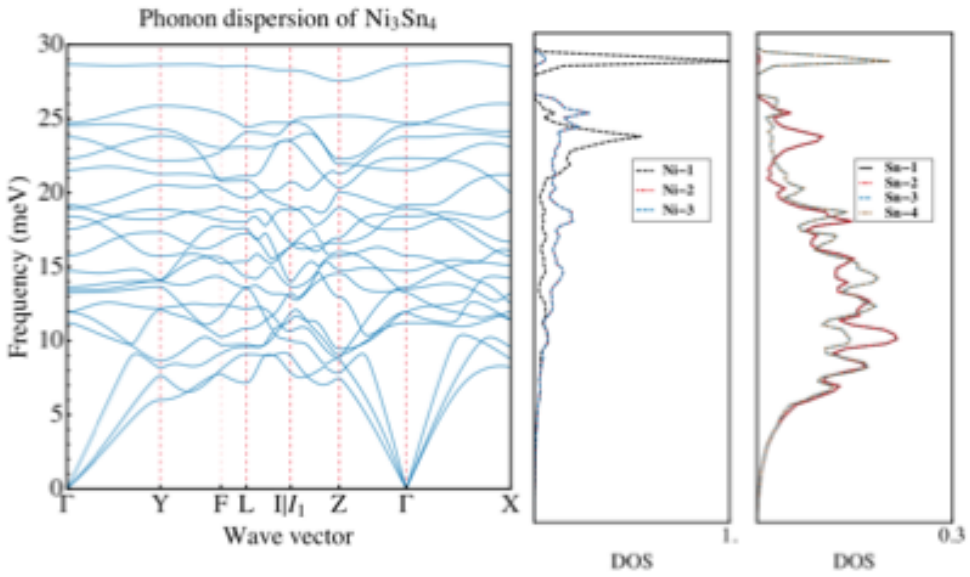

Figure 4.19 The First-principle simulation of atomic vibration frequency of the Ni and Sn atoms in Ni_3Sn_4

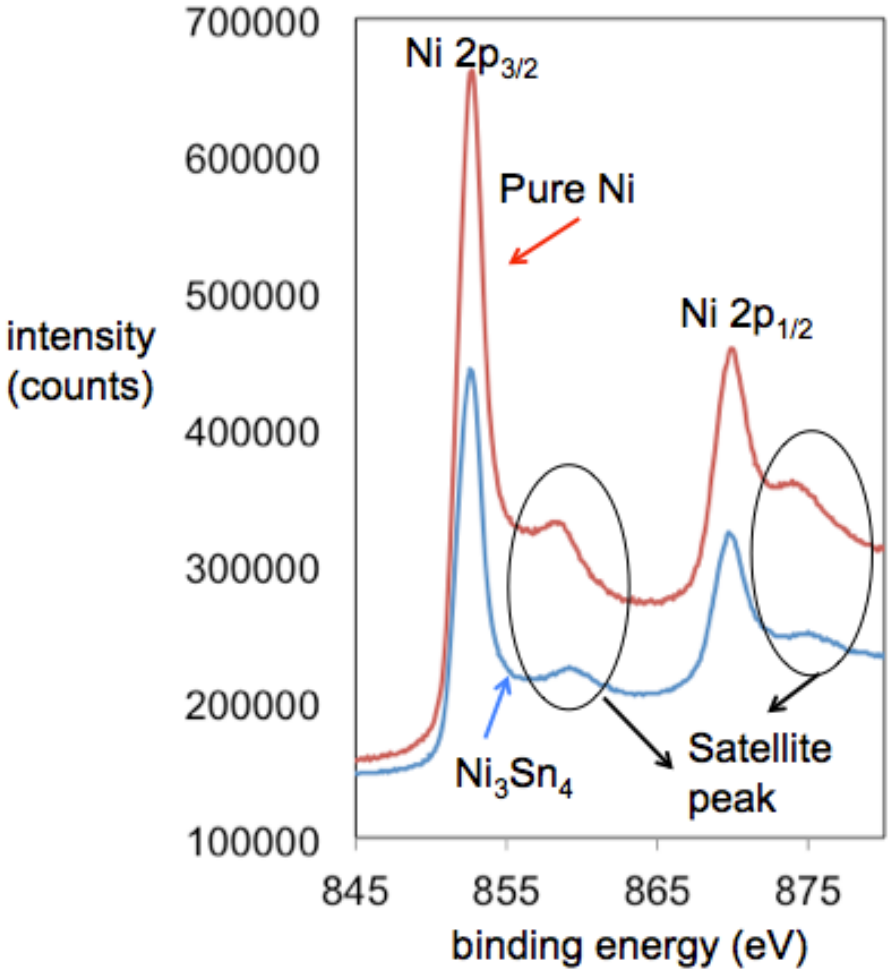

Figure 4.20 XPS spectrum of the binding energy of Ni 2p electrons in pure Ni and Ni_3Sn_4

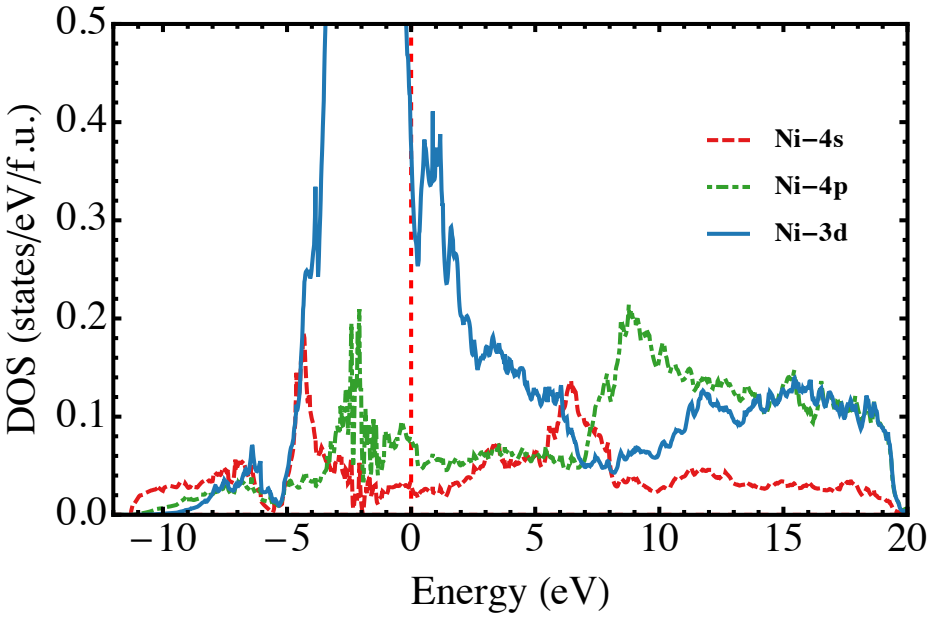

Figure 4.21 The simulation of outer electrons' energy for Ni atoms in Ni_3Sn_4

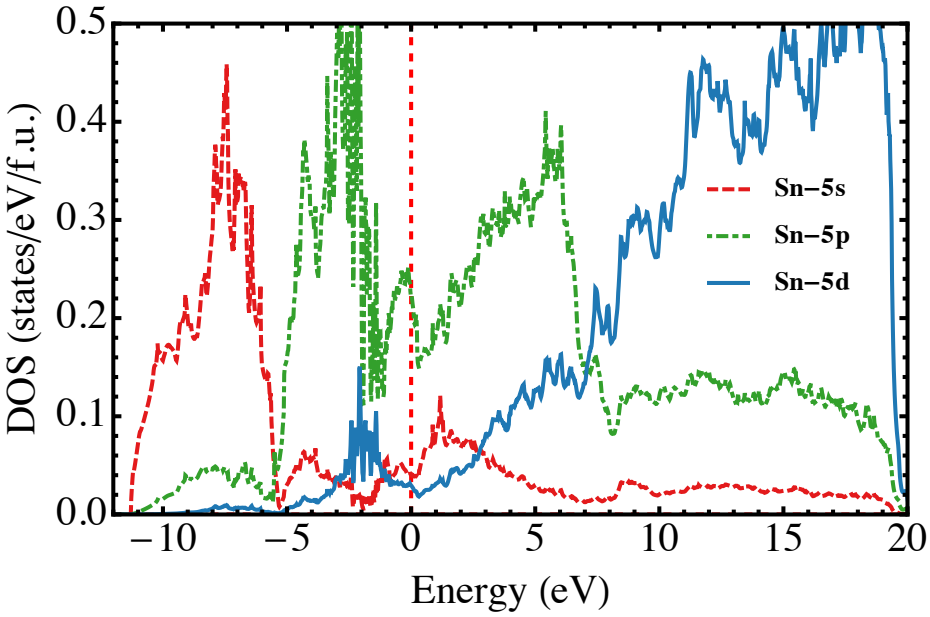

Figure 4.22 The simulation of outer electrons' energy for Sn atoms in Ni_3Sn_4

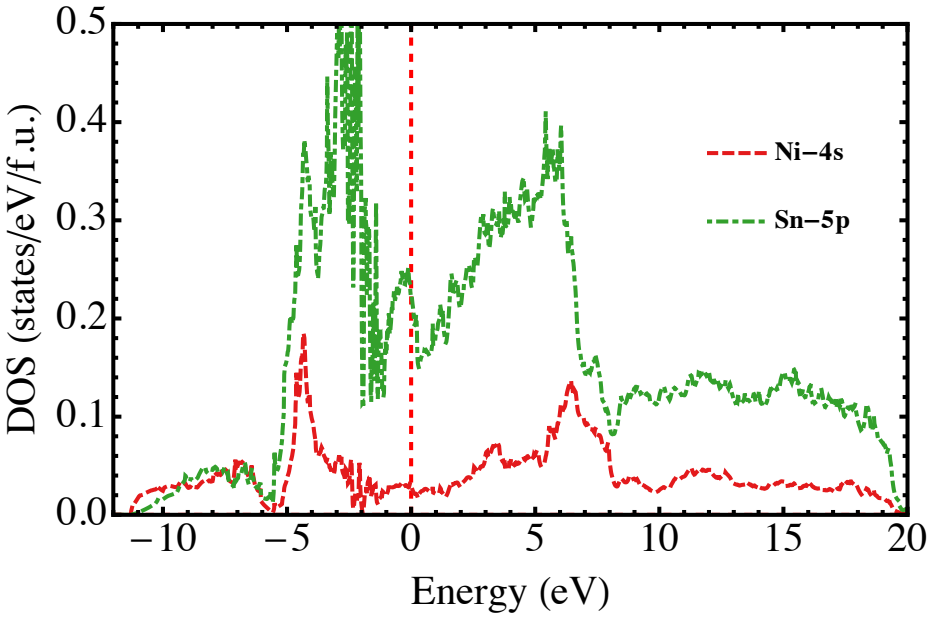

Figure 4.22 The simulation of the energy for Ni 4s orbital and Sn 5p orbital in Ni_3Sn_4

T (^{o}C)	150	170	190	210
D_{Ni} (cm^2/s)	2.9×10^{-16}	1.1×10^{-15}	4.8×10^{-15}	1.8×10^{-14}
D_{Sn} (cm^2/s)	4.3×10^{-16}	2.1×10^{-15}	1.9×10^{-14}	1.1×10^{-13}

Table 4.1 Tracer diffusivities of Ni and Sn in Ni_3Sn_4 at different temperatures

	Bonding strength	Jumping attempt frequency, ν	Diffusion prefactor, D_o	Atomic volume	ΔS	ΔH_f
Sn		–	✔	✔	✔	✔
Ni	✔	–				

Table 4.2 Factors influence diffusivities of atoms

Chapter 5 Chemical Effect on Cu_3Sn Intermetallic Compound

5.1 Cu-Sn intermetallic compounds

There are various intermetallic compounds may form in Cu-Sn system; however, under the temperature of interests in electronic packaging (below 300°C), only Cu_6Sn_5 and Cu_3Sn will form as shown in Cu-Sn phase diagram (Fig. 5.1).

The systematic model to obtain the tracer diffusivities in the intermetallic compound is for one compound formation only; if there's multiple compounds formed in the diffusion couple, the unknown will increase and more equations are needed to solve the unknowns. For example, in the Cu-Sn case, there is two compounds formed (Fig. 5.2) [66-68] so that there will be four unknowns, which are the tracer diffusivities of Sn atoms and Cu atoms in Cu_6Sn_5 and Cu_3Sn. This infers that we need two more equations to solve the problem, yet to drive further equations in the diffusion couples is hard and complicated. Therefore, it is not a best option to do the experiment on pure Sn and pure Cu because several compounds will form. We then conduct the experiment on IMC/pure metal diffusion; for instance, we can prepare Cu/Cu_6Sn_5 and Sn/Cu_3Sn diffusion couples to examine the diffusivities of atoms in Cu_3Sn and Cu_6Sn_5 respectively as shown in Fig. 5.3. In this chapter, we will focus on the Cu/Cu_6Sn_5 diffusion couple and the diffusivities of Cu atoms and Sn atoms in Cu_3Sn intermetallic compound.

5.2 Experimental Procedure

To prepare the diffusion couple of Cu_6Sn_5/ Cu_3Sn /Cu, we need to have bulk sample of pure Cu_6Sn_5. Owing to the fact that the sample is not east to prepare, we collaborated with Professor Liu's group in National Central University, Taiwan, to obtain the bulk Cu_6Sn_5 sample. The samples were made by a novel way called liquid-phase electroepitaxy (LPEE) developed by the group [69]. High temperature (400 °C) and high current (1A) are used in the process; there are two Cu bar squeezing the liquid Sn, and the electrical current stressed the Cu atoms, making them move from the cathode to the anode and form Cu_6Sn_5 intermetallic compound at the anode side. If the time is long enough, the whole liquid Sn in the middle can all transform into Cu_6Sn_5 intermetallic compound as shown in Fig. 5.4.

We first used diamond-saw machine to cut a bulk-type pure Cu_6Sn_5 sample into 1 cm^2 pieces with thickness around 1 mm. Then the Cu_6Sn_5 pieces were carefully polished by alumina powder with final polishing particle size less than 0.05 μm. After polishing, the Cu_6Sn_5 pieces were dipped into 20% HCl solution to remove the oxide on the surface, and followed by putting into $CuSO_4$ water solution for electroplating of copper. The electroplating process was undergone in 500 mL 0.8 $CuSO_4$ solution with 25 mL H_2SO_4; and the current density was 0.05 A/cm^2. The samples were electroplated for one hour to grow a 100 μm thick copper layer. After that, the electroplated samples were placed in oven and annealed for 1 day at 170°C in order to grow a layer of Cu_3Sn between the Cu_6Sn_5 and Cu. Finally, the samples were polished to expose the interfaces in the cross-section of Cu_6Sn_5/ Cu_3Sn /Cu.

The markers on the cross-sectional surface were made with FIB, using a finely focus gallium ions beam at a high current for sputtering. The FIB was applied to the Cu_3Sn layer, and circular holes, with diameter around 1μm and depth around 3 μm, were created to serve as moving markers. Also there were larger rectangular markers made on the Cu_6Sn_5 side to serve as fixed markers for the measurement of the motion of markers on the IMC. After the placement of markers, the diffusion couples were annealed at 110 °C, 130 °C, 150 °C and 170 °C for different periods to allow the IMC growth and the marker motion.

To characterize the IMC, back-scattered electron (BSE) microscope and dispersive X-ray spectroscopy (EDX) were used. The cross-section of each diffusion couple after placing markers and after annealing at different times and temperatures were lightly polished for measuring the thickness of IMC by BSE and for confirming the composition by EDX. For measuring the IMC thickness, the average height of Cu_3Sn perpendicular to the Cu layer is calculated by the software called ImageJ from BSE image. To examine the chemical interaction between Cu and Sn atoms in Cu_3Sn lattice, X-ray photoelectron spectroscopy (AXIS Ultra DLD) was used to measure the chemical shift of core electrons' bonding energy for Cu atoms and Sn atoms.

5.3 Solid state growth of Cu_3Sn intermetallic compound

The growth profile of Cu_3Sn intermetallic compound annealed at 110 °C, 130 °C, 150 °C and 170 °C is shown in Fig. 5.5. The growth of Cu_3Sn meets solid-state diffusion model very well with the coefficient of determination (R^2) of linear

regression around 0.99 and the time exponent is 0.5. Additionally, the linear regression slope of the data at 110 °C, 130 °C, 150 °C and 170 °C are 0.012, 0.04, 0.07 and 0.15 μm^2/hour, respectively. Furthermore, Fig. 5.6 shows the logarithm of the growth rate versus the reverse temperature and the activation energy of Cu_3Sn growth can be measured from the slope. The activation energy of Cu_3Sn growth in this study is 57 kJ/mole, which matches the results from previous reports [70-72].

There are two kinds of markers presents in the diffusion couples as shown in Fig. 5.7; one is square marker on Cu_6Sn_5 and the other is circular marker on Cu_3Sn. The square markers are fixed because they are not involved in the interdiffusion of the two species, and the circular markers tend to move with the growth of Cu_3Sn. We can locate the center of both markers and observe the relative motion between them, so that we can determine the moving direction of circular markers as well as the velocity of motion. In turn, the fast diffusion species in IMC under annealing can be determined. Moreover, the circular marker can also be considered as the reference point of Sn and Cu diffusion.

The results of the marker motion experiment at the 170 °C annealing are shown in Fig. 5.7(a), we can see clearly that the circular marker moved towards the Cu side, which suggests that there are net vacancies moved toward the Cu side. That is to say, there are more Cu atoms traveling through the IMC to the other side than the opposite Sn atoms. Noted that the moving marker shrinks a little bit from time to time, this is because the aspect ratio of the circular hole is large so that focus ion beam cannot sputter away IMC efficiently; the bottom material cannot fly away and accumulate at the wall, causing the shape tapered toward the bottom like a circular

cone instead of a circular pillar. Furthermore, since the sample was polished after different annealing time to avoid the effect of surface diffusion, the circular marker seems getting smaller. Nevertheless, the center of the circle is always the same, thus we can use the center as the marker's position. The marker motion at 150 °C and 130 °C annealing temperatures also show that the circular marker moved toward Cu side, thus Cu is the dominant diffusion species. However, the marker motion is not obvious at 110 °C because the diffusion rate is too slow to allow enough marker motion to occur.

A horizontal line is drawn across the center of the moving marker and the ratio of diffusion of Sn atoms and Cu atoms can be determined by measuring the IMC growth above and below the horizontal line; that is to say, the growth of Cu_3Sn above the line is due to the Cu diffusion while the growth of Cu_3Sn below the line is due to the Sn diffusion. Moreover, the ratio needs to be adjusted by multiplying some constants owing to different reaction mechanisms that will be discussed later. The results are presented in Table 1, and it shows that Cu atoms diffused much faster than Sn atoms from 170 °C to 110 °C; moreover, the ratios at 170 °C, 150 °C, 130 °C and 110°C are 100, 40, 30 and 20, respectively.

5.4 Tracer diffusivities of Sn atoms and Cu atoms in Cu_3Sn IMC

5.4.1 Kinetic theory to determine the tracer diffusivities of atoms in an intermetallic compound

From the previous work in our group, we develop a way to determine the tracer diffusivities of atoms in intermetallic compound by considering the chemical effect in it. The large chemical effect means that the bonding between Cu atom and Sn atom is much larger than half of Cu-Cu bond plus Sn-Sn bond; thus breaking the Cu-Sn bonds will affect the diffusion of both Cu and Sn atoms. By taking into account this effect, we can apply Wagner diffusivity and marker analysis in the previous discussion to separate the chemical effect in order to calculate the tracer diffusivities of atoms in IMC.

We recall that the graphical method is used to transform the immeasurable parameter to a measurable one; since we have two intermetallic compounds in Gibbs free energy diagram now as shown in Fig. 5.8, the revision of the equation is needed. We should start from equation 2.19 to determine the second derivative of Gibbs free energy at composition equal Cu_3Sn, and we can obtain:

$$\begin{aligned} g''(X_R - X_L) = g''\Delta X &= \left.\frac{\partial g}{\partial X}\right|_{X_R} - \left.\frac{\partial g}{\partial X}\right|_{X_L} \\ &= \frac{g_{65} - g_{31}}{X_{65} - X_{31}} - \frac{g_{31} - g_{Cu}}{X_{31} - 0} \quad (X_{31} \approx X_R \approx X_L) \\ &= \frac{X_{31}g_{65} + (X_{65} - X_{31})g_{Cu} - X_{65}g_{31}}{(X_{65} - X_{31})X_{31}} \end{aligned} \qquad \text{--- (5.1)}$$

where g_{65}, g_{31} and g_{Cu} are the Gibbs free energy of Cu_6Sn_5, Cu_3Sn, and Cu; moreover, X_{65}, X_{31} and X_{Cu} are the molar ratio of Sn in Cu_6Sn_5, Cu_3Sn, and pure Cu respectively. We can put it back to the diffusion equation and obtain:

$$\frac{x_i^2 - x_0^2}{t} = 2(X_{31}D_{Cu}^* + (1 - X_{31})D_{Sn}^*)\frac{X_{31}(1 - X_{31})\Delta g_r}{(X_{65} - X_{31})X_{31}} \qquad \text{--- (5.2)}$$

where x_0 is the initial thickness of the IMC, x_i is the thickness of the IMC after annealing, X is the molar ratio in the IMC, D^* is the tracer diffusivities of atoms in

IMC, k is Boltzmann constant, T is annealing temperature, t is annealing time and Δg_r is the reaction energy of $0.25Cu_{0.55}Sn_{0.45} + (0.45 - 0.25)Cu \rightarrow 0.45Cu_{0.75}Sn_{0.25}$; which is equal to $Cu_6Sn_5 + 9Cu \rightarrow 5Cu_3Sn$ with Cu_6Sn_5 and Cu_3Sn in the form of $Cu_{0.55}Sn_{0.45}$ and $Cu_{0.75}Sn_{0.25}$ respectively.

The second equation we can recall the flux ratio and the tracer diffusivity ratio of A atoms and B atoms in equation 2.20 and have:

$$\frac{J_{Sn}}{J_{Cu}} = \frac{D^*_{Sn}}{D^*_{Cu}} = \frac{\alpha\Delta(x_2 - x_m)}{\beta\Delta(x_m - x_1)} \quad \text{--- (5.3)}$$

where J is the flux of the atoms in the IMC, x_2 is the location of Cu and Cu_3Sn interface, x_1 is the location of Cu_6Sn_5 and Cu_3Sn interface, and x_m is the location of the marker. Thus, $\Delta(x_2-x_m)$ represents the growth of the IMC contributed by Sn atom diffusion and $\Delta(x_m-x_1)$ represents the growth of the IMC contributed by Sn atom diffusion; α and β are the correction factor owing to the fact that one layer of Cu atoms diffuse to Cu_6Sn_5 does not form exactly one Cu_3Sn layer, vice versa. We shall discuss the value of them in the case of Cu_6Sn_5/ Cu_3Sn /Cu diffusion couple below.

From the reaction $Cu_6Sn_5 + 9Cu \rightarrow 5Cu_3Sn$, we know that 9 Cu atoms traveling to Cu_6Sn_5 side can form 5 Cu_3Sn molecules; therefore, β here is equal to 9/5. On the other hand, the correction term of Sn is more complicated because the diffusion of Sn atoms involves the decomposition of Cu_6Sn_5. If we assume that 3 Sn atoms from one Cu_6Sn_5 diffuse away to the Cu side, there will be 3 Cu_3Sn formed at the Cu_3Sn /Cu interface, and the remaining Cu_6Sn_5 will form 2 Cu_3Sn at the Cu_6Sn_5/ Cu_3Sn interface. Thus, we should take α equals to 1 because 1 Sn atom diffuses to Cu side can form one Cu_3Sn. Furthermore, since the diffusion of Sn somehow assist the

growth at Cu_6Sn_5/ Cu_3Sn interface, the real Cu_3Sn growth contributed by Cu diffusion should be $\Delta(x_m-x_1) - 2/3\Delta(x_2-x_m)$. And we have Equation (5.4) to replace equation (5.3).

$$\frac{J_{Sn}}{J_{Cu}} = \frac{D^*_{Sn}}{D^*_{Cu}} = \frac{\Delta(x_2 - x_m)}{\frac{9}{5}[\Delta(x_m - x_1) - \frac{2}{3}\Delta(x_2 - x_m)]} \quad \text{--- (5.4)}$$

5.4.2 Tracer diffusivities of Cu and Sn in Cu_3Sn

To remove the chemical effect so that we can calculate the tracer diffusivities, we take $X_{Cu}=3/4$, $X_{Sn}=1/4$ in equation (5.3) and put all the values into equation (5.3) and (5.4) such as slopes, ratio at different temperatures from our analysis earlier. The reaction energy of IMC per atom can be calculated from published paper [77], which is equal to 2.1 kJ/g-atom. The tracer diffusivities of Sn and Cu in Cu_3Sn at several temperatures are shown in Table 2. We can plot the tracer diffusivities of Sn and Cu versus the reverse temperature in Fig. 5.9 and obtain the activation enthalpy of diffusion for Cu and Sn in Cu_3Sn, which are 59 and 96 kJ/mole, respectively. The activation enthalpy of diffusion for Sn is much higher than Cu, which leads to the higher diffusivities of Cu atoms than Sn atoms in Cu_3Sn. For more discussion on the diffusion behavior, we shall examine below XPS and the crystal structure of Cu_3Sn.

5.5 Chemical effect in Cu_3Sn

We performed XPS characterization on pure Cu, Cu_6Sn_5 and Cu_3Sn IMC in order to understand the chemical interactions between Cu and Sn atoms. For instance,

when Cu forms CuO, the O atom will attract the outer electrons from Cu atom due to the larger electronegativity; this makes bonding change for Cu atom in transforming from metallic bonding to ionic bonding. If there is a chemical shift for an element between its states in pure element and in compound formation, we expect that there is electrons redistribution; hence it will influence the bonding behavior. The influence of electron redistribution on chemical shift varies from element to element; for example, there is only less than 0.2 eV shift for Sn in SnO and SnO_2. Yet, on the other hand, the chemical shift for Cu in CuO and CuO_2 is 2 eV [73]. Since the effect of chemical shift on Cu atom is much larger than Sn atoms, plus the fact that the electronegativity difference between Cu and Sn is very small (only 0.1), thus we should focus on the XPS result on Cu element.

From Fig. 5.10, we can see the binding energy of Cu 2p electrons for Cu in pure Cu, Cu_6Sn_5 and Cu_3Sn. The result of two peaks is due to spin orbital splitting effect; the right peak stands for $2p_{1/2}$ and the left peak stands for $2p_{3/2}$. By comparing the two peaks for pure Cu, Cu_6Sn_5 and Cu_3Sn, we can see that the chemical shift for Cu_6Sn_5 and Cu_3Sn relative to pure Cu is 0.3 eV and 0.1eV, respectively. The existence of the chemical shift implies the outer electrons of Cu in Cu_6Sn_5 and Cu_3Sn are in some degree have moved to Sn. This behavior increases slightly the valence charge of Cu and decreases the valance charge of Sn, resulting in partial covalent bonding between Cu and Sn atoms in Cu_3Sn. The partial covalent property makes Cu-Sn bond stronger than pure metallic Sn-Sn and Cu-Cu bond, which means there are chemical interactions between Cu and Sn atoms.

5.6 Lattice structure model of Cu_3Sn

Fig. 5.11 shows the lattice structure of Cu_3Sn with one Sn position and two Cu positions. Due to the fact that Cu_3Sn consists of 75 atomic percent Cu, Cu has long range sub-lattice to diffuse in all the directions. Moreover, from Fig. 5.12, we can see that Cu has average 7.5 Cu-Cu bonds and 4 Cu-Sn bonds; the large amount of Cu-Cu bonds provides a perfect path for atomic diffusion of Cu. On the other hand, we can observe that Sn atoms do not form bond with themselves (no Sn-Sn bonds), this makes it extremely hard to diffuse in the lattice.

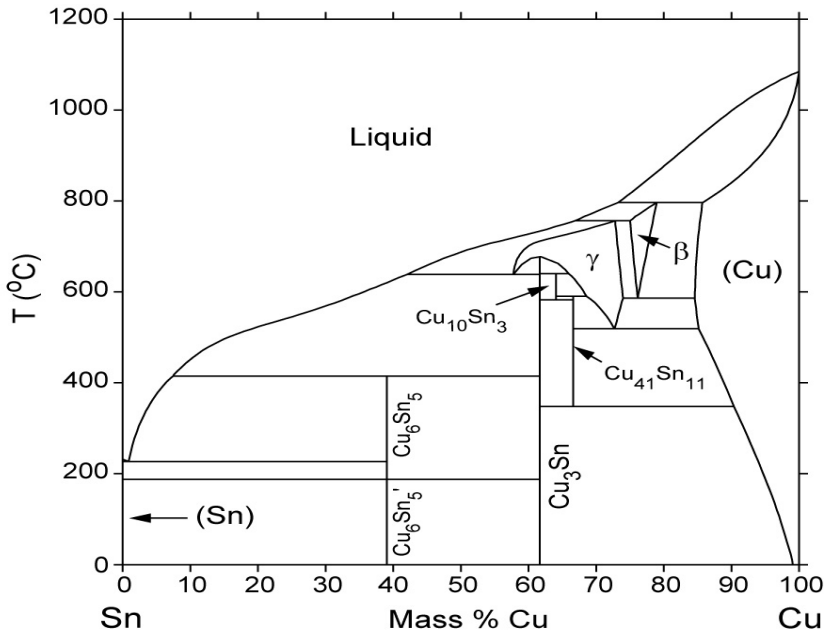

Figure 5.1 Phase diagram of Cu and Sn binary system

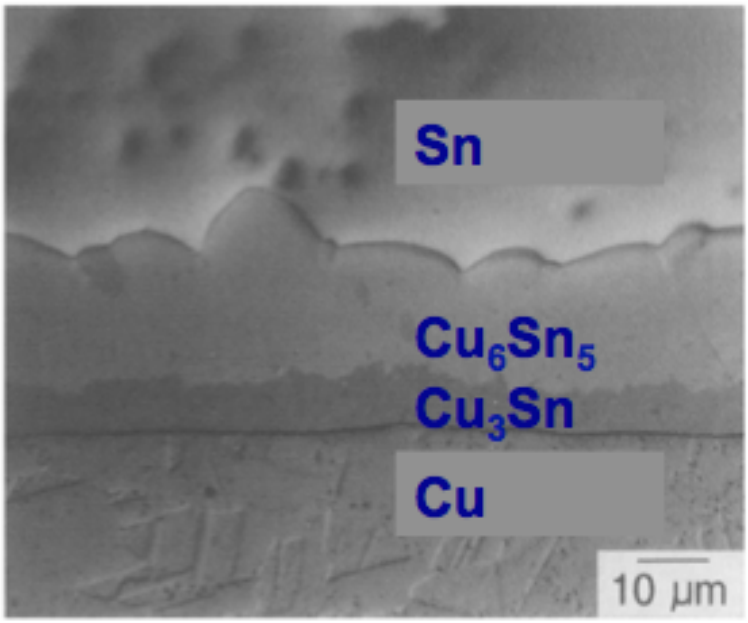

Figure 5.2 Intermetallic compounds formation at 200 °C annealing between pure Sn and pure Cu

©*P.T. Vianco et al. /* Journal of Electronic Materials Vol. 23 No. 8 1994

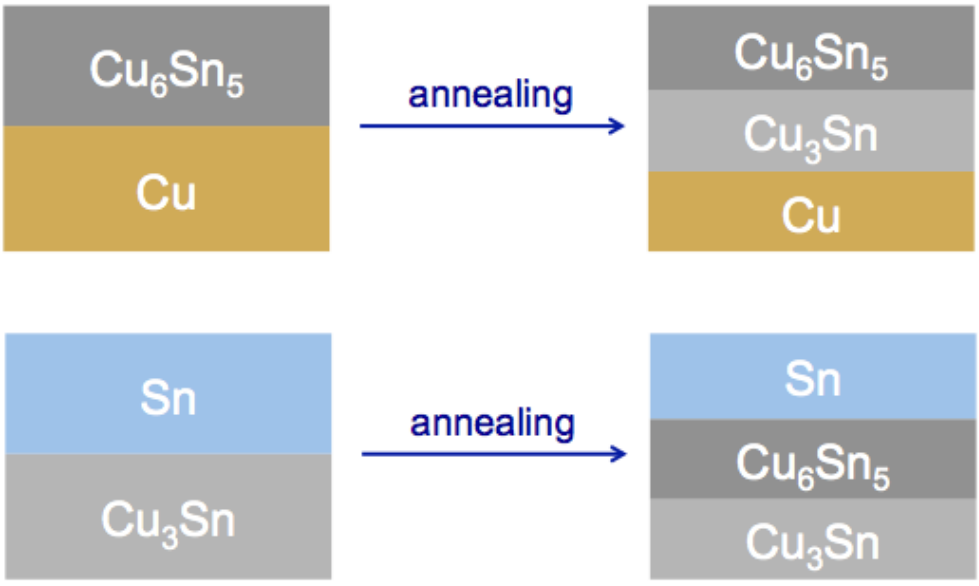

Figure 5.3 Schematic diagrams of IMC/pure metal diffusion couple to observe the growth behavior of the other IMC

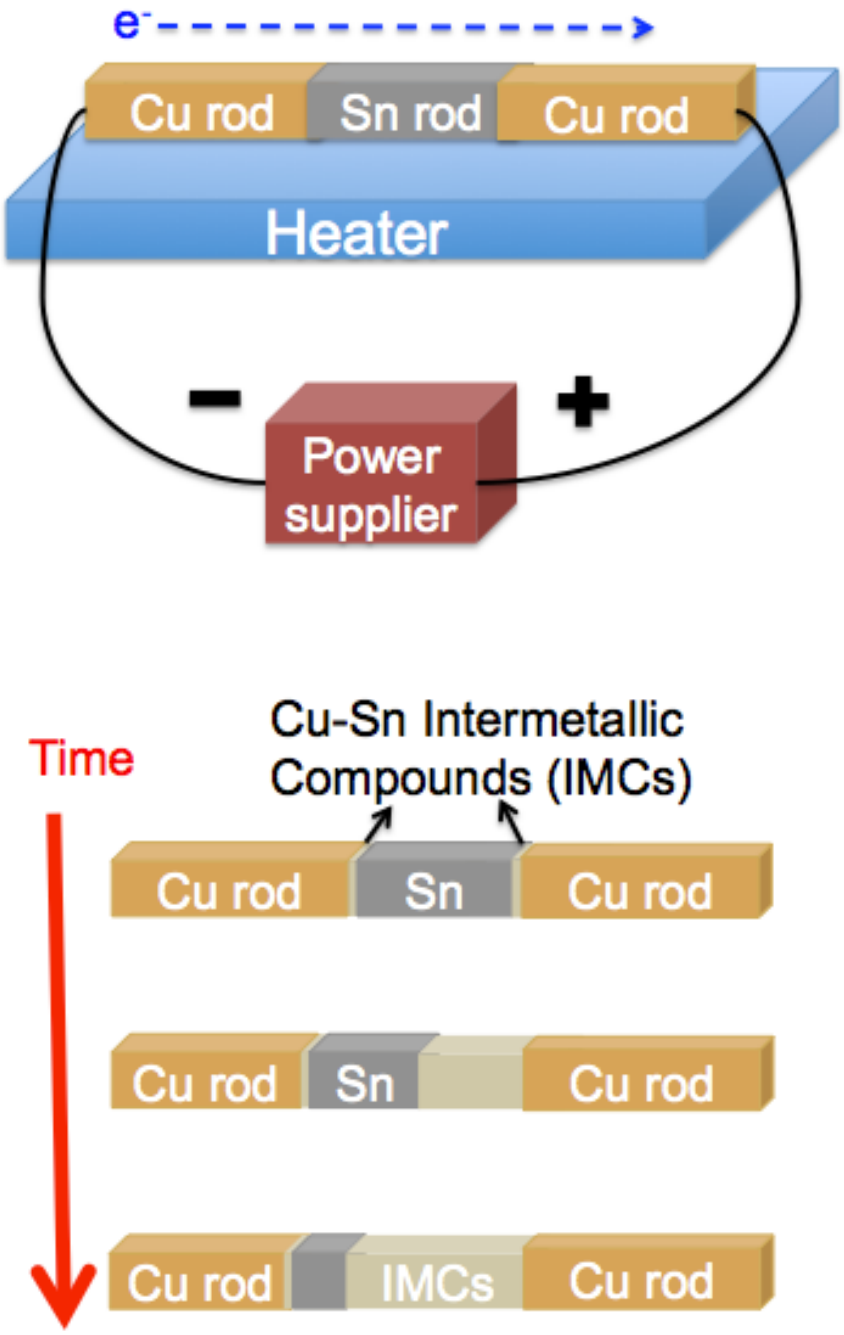

Figure 5.4 The Schematic diagrams of the setup and the process for LPEE bulk IMC fabrication

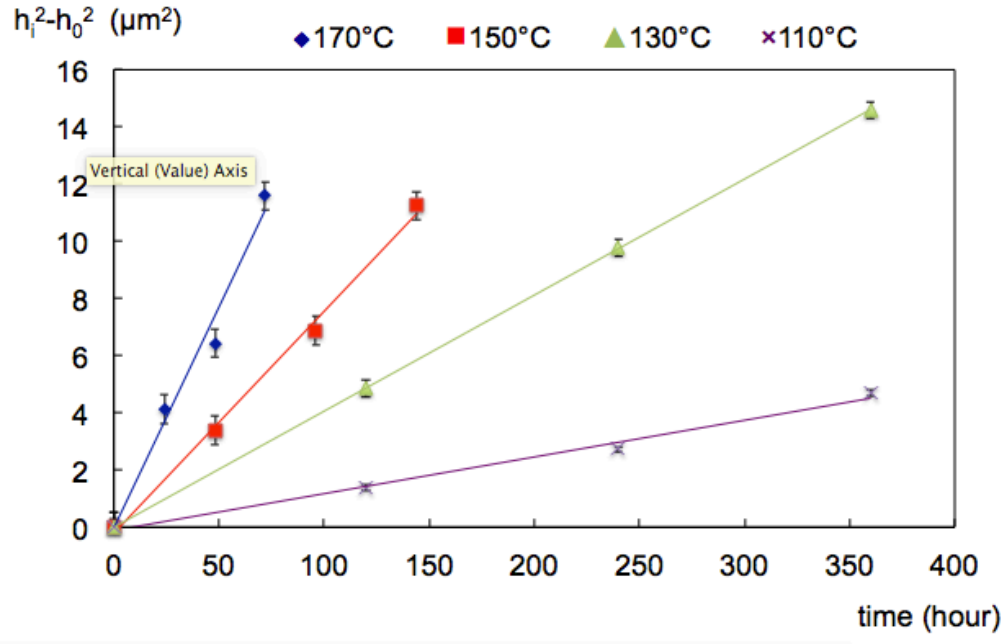

Figure 5.5 Growth profile of Cu_3Sn between Cu and Cu_6Sn_5 at several different temperatures

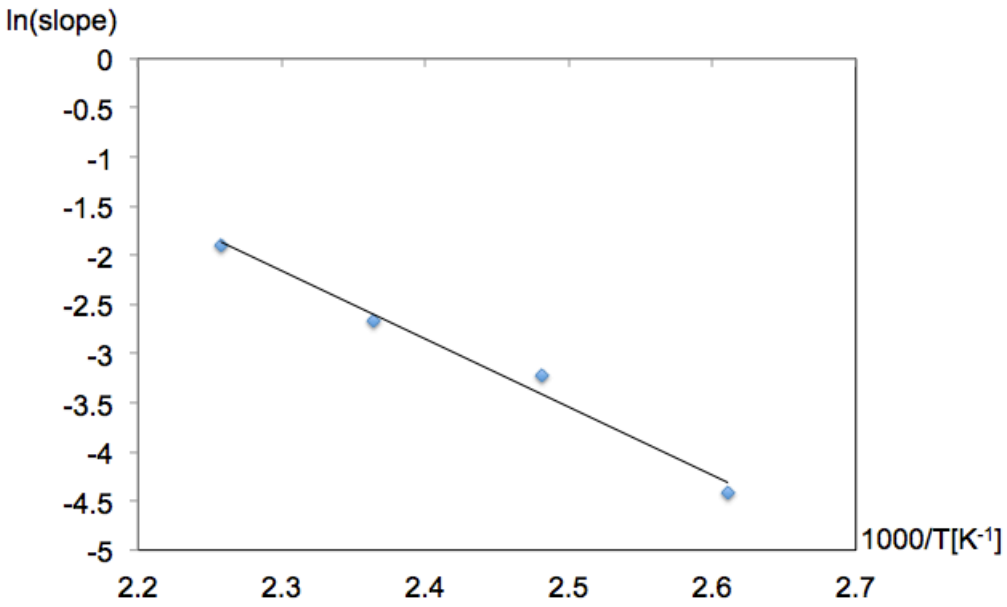

Figure 5.6 Logarithm of the growth slope versus the inverse temperature to get diffusion activation energy

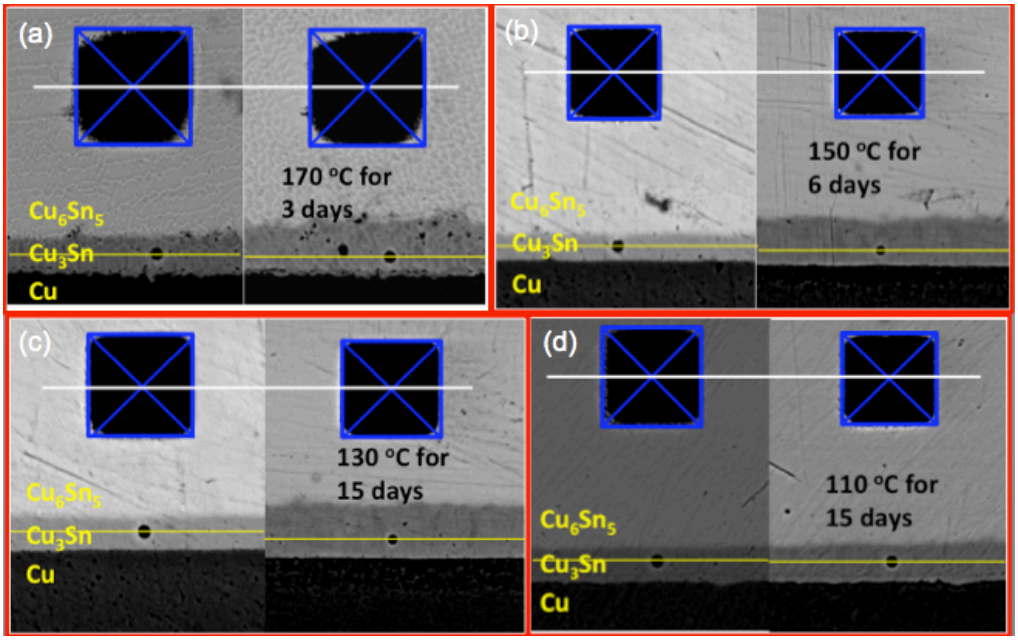

Figure 5.7 Marker analysis on $Cu_6Sn_5/Cu_3Sn/Cu$ diffusion couple at (a) 170 °C, (b) 150 °C, (c) 130 °C and (d) 110 °C

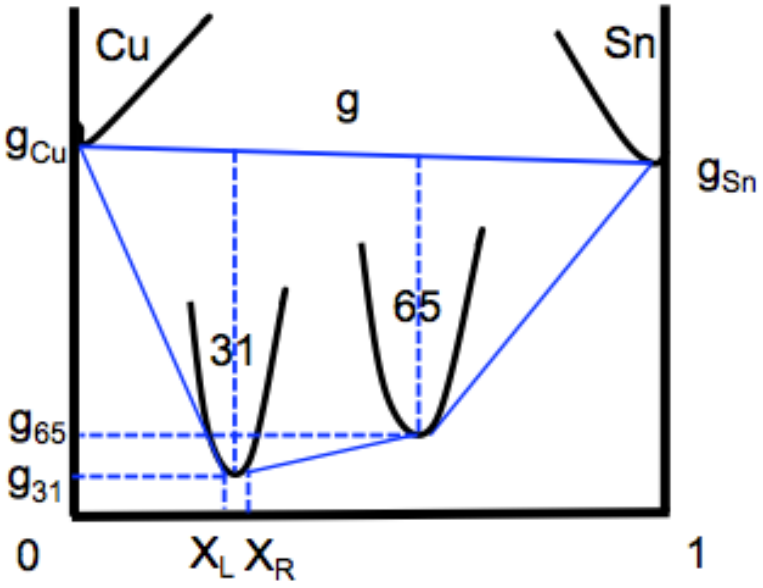

Figure 5.8 Schematic diagram of Gibbs free energy versus Sn concentration in Cu-Sn binary system

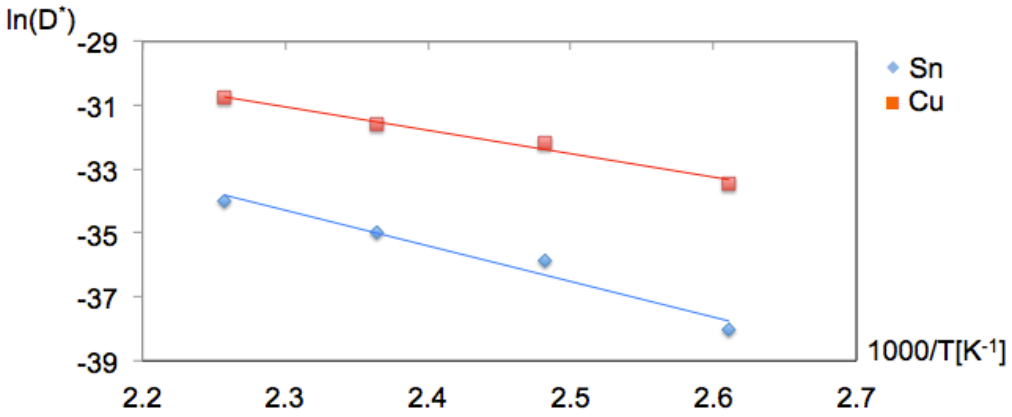

Figure 5.9 Logarithm of tracer diffusivities of atoms versus the inverse diffusion temperature

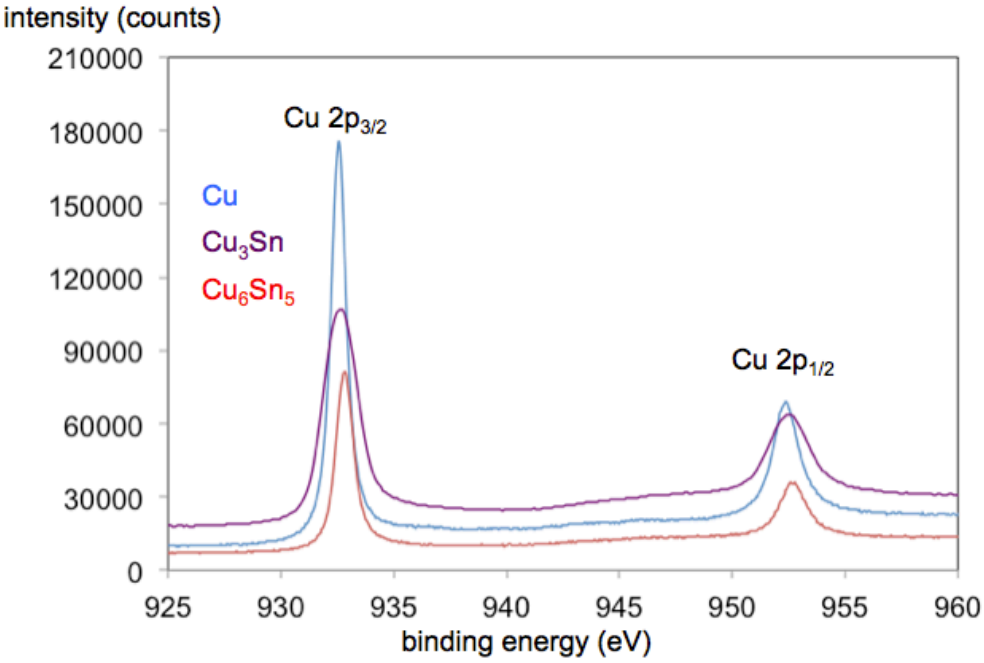

Figure 5.10 XPS spectrum for Cu 2p electrons in pure Cu, Cu_3Sn and Cu_6Sn_5

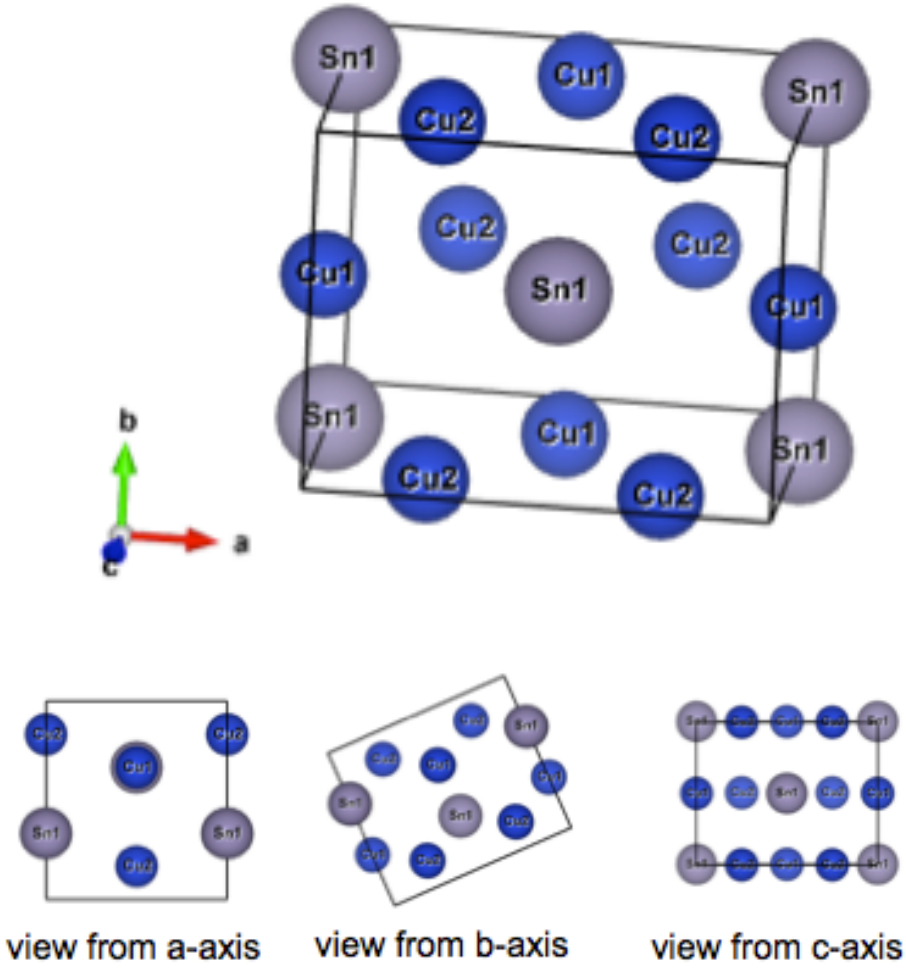

Figure 5.11 Lattice structure of Cu_3Sn intermetallic compound

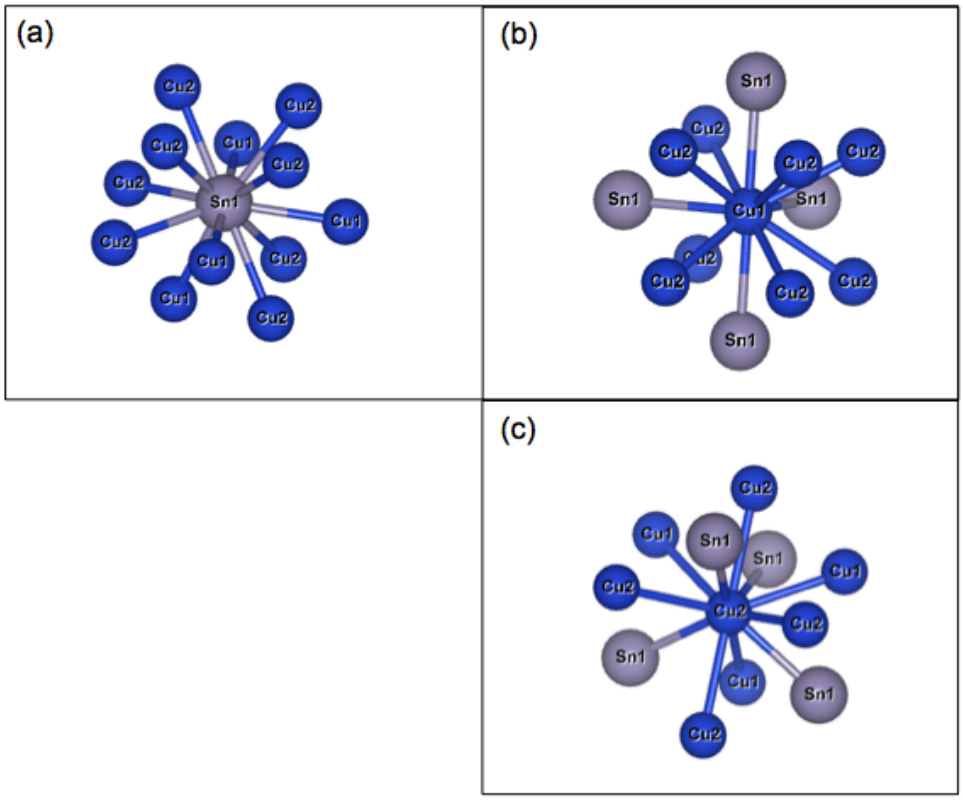

Figure 5.12 Atomic bonding diagram in Cu_3Sn for (a) Sn atom (b) Cu1 atom and (c) Cu2 atom

T (^{o}C)	110	130	150	170
D_{Cu} (cm^2/s)	3×10^{-15}	1.05×10^{-14}	1.93×10^{-14}	4.33×10^{-14}
D_{Sn} (cm^2/s)	$<3\times10^{-17}$	2×10^{-16}	6×10^{-16}	1×10^{-15}
ratio	>100	40	30	25

Table 5.1 Tracer diffusivities of Cu and Sn atoms in Cu_3Sn with various temperatures

Chapter 6 Summary

In this work, chemical effect on diffusion in IMC was studied; with the novel FIB marker design and the introduction of Wagner diffusivity, the tracer diffusivities of atoms inside an IMC can be obtained. This systematic way was applied on Ni_3Sn_4 and Cu_3Sn, which are two of the most important intermetallic compounds in electronic packaging industry.

Tracer diffusivities of Ni and Sn in Ni_3Sn_4 were calculated at 210 °C, 190 °C, 170 °C and 150 °C by applying correction of chemical effects on intrinsic diffusivities in the IMC and by combining marker analysis designed for sub-micron dimension reactions. In the diffusion model, the immeasurable parameter of the concentration gradient across the IMC interfaces was replaced by the formation energy of the IMC owing to the fact that the chemical potential driving force of diffusion is much larger than concentration gradient driving force in IMC. The XPS and the First principle simulation results implied the hybrid covalent bonding nature for Ni-Sn bond in Ni_3Sn_4, which explained the large Gibbs free energy decrease when forming the IMC.

Furthermore, Sn is observed to be the dominant diffusing species in Ni_3Sn_4 under the temperature range studied; however, the activation energy of diffusion for Sn is higher than that for Ni, which suggests a larger prefactor of diffusion for Sn. Since the atomic volume of Sn is about twice larger than that of Ni, it is assumed that the large atomic volume will squeeze the lattice more hence the activation energy is

higher. On the other hand, it is assumed that the diffusion prefactor of Sn is much larger than that of Ni owing to the large distortion and entropy gain during diffusion.

Additionally, we investigated the chemical effect on intrinsic diffusion in IMC of Cu_3Sn. In order to remove the chemical effect so that we can obtain tracer diffusivity of Cu and Sn in Cu_3Sn, we use Wagner's model to overcome the difficulty of a near zero concentration gradient across a stoichiometric compound layer during its growth. Then, marker analysis was performed to show that Cu is the dominant diffusing species in Cu_3Sn in the temperature range from 110 °C to 170 °C. The diffusion activation energy of Sn atoms is measured to be 50% higher than that of Cu atoms. Furthermore, we did XPS analysis to observe the chemical shift in Cu-Sn IMC and deduced that Cu-Sn bonding has a partial covalent bonding nature. Moreover, the simulation model of the lattice structure of Cu_3Sn implied that the Cu atoms have a long range sub-lattice in all directions for fast diffusion in Cu_3Sn.

References

1. http://en.wikipedia.org/wiki/Electronic_package
2. https://en.wikipedia.org/wiki/Three-dimensional_integrated_circuit
3. H. P. R. Frederikse, R. J. Fields and A. Feldman, "Thermal and electrical properties of copper-tin and nickel-tin intermetallics," J. Appl. Phys. 72, 2879 (1992).
4. Sinn-Wen Chen, Shou-Wei Lee and Ming-Chuen Yip, "Mechanical Properties and Intermetallic Compound Formation at the Sn/Ni and Sn-0.7wt.%Cu/Ni Joints," Journal of Electronic Materials, Vol. 32, No. 11, (2003).
5. G. Ghosh, Elastic properties, "hardness, and indentation fracture toughness of intermetallic relevant to electronic packaging," J. Mater. Res., Vol. 19, No. 5, May (2004).
6. Ping-Feng Yang, Yi-Shao Lai, Sheng-Rui Jian and Jiunn Chen, "Mechanical Properties of Cu6Sn5, Cu3Sn, and Ni3Sn4 Intermetallic Compounds Measured by Nanoindentation," Electronic Packaging Technology, 2007. ICEPT 8th International Conference.
7. Li-Jung Tai, Iting Tsai and E. Wu, "Mechanical Properties of Ni_3Sn_4 and Cu_3Sn Determined by Inverse Method," Components and Packaging Technologies, IEEE Transactions on (Volume:31 , Issue: 2)
8. S. K. Kang, W. K. Choi, M. J. Yim and D. Y. Shih, "Studies of the mechanical and electrical properties of lead-free solder joints," Journal of Electronic Materials, Vol. 31, No. 11, 2002

9. R.R. Chromik, R.P. Vinci, S.L. Allen, and M.R. Notis, “Measuring the mechanical properties of Pb-free solder and Sn-based intermetallics by nanoindentation,” JOM Volume 55, Issue 6, 2003 pp 66-69
10. Iuliana Panchenko et al., “Degradation of Cu_6Sn_5 Intermetallic Compound by Pore Formation in Solid–liquid Interdiffusion Cu/Sn Microbump Interconnects,” Microelectronic Engineering 117 (1) (2014), 26–34.
11. Yingxia Liu et al., “A Metastable Phase of Tin in 3D Integrated Circuit Solder Microbumps,” Scripta Materialia,” 102 (2015), 39–42.
12. A.D. Smigelskas and E.O. Kirkendall, “Zinc Diffusion in Alpha Brass,” *Trans. AIME,* 171 (1947), pp. 130-142.
13. Matano and Chujiro, “On the Relation between the Diffusion-Coefficients and Concentrations of Solid Metals (The Nickel-Copper System)”, Japanese Journal of Physics (1933)
14. David A. Porter, “Phase transformations in metals and alloys”, (1981)
15. https://en.wikipedia.org/wiki/Fick%27s_laws_of_diffusion
16. P. Heitjans and J. Karger, “*Diffusion in condensed matter: Methods, Materials, Models* 2nd ed.”. Birkhauser (2005)“
17. http://mmrc.caltech.edu/SS_XPS/XPS_PPT/XPS_Slides.pdf
18. https://en.wikipedia.org/wiki/X-ray_photoelectron_spectroscopy
19. N. Ikeo et al., “Handbook of X-ray Photoelectron Spectroscopy,” JEOL, 1991
20. C. C. Chusuei , M. A. Brookshier , and D. W. Goodman, “Correlation of Relative X-ray Photoelectron Spectroscopy Shake-up Intensity with CuO Particle Size,” Langmuir, 1999, 15 (8), pp 2806–280

21. Mark C. Biesinger et al., “Resolving surface chemical states in XPS analysis of first row transition metals, oxides and hydroxides: Sc, Ti, V, Cu and Zn8,” Applied Surface Science 257 (2010) 887–898
22. Mark C. Biesinger et al., “Resolving surface chemical states in XPS analysis of first row transition metals, oxides and hydroxides: Cr, Mn, Fe, Co and Ni,” Applied Surface Science 257 (2011) 2717–2730
23. http://www.cpi.com/capabilities/fpm.html
24. http://cmt.dur.ac.uk/sjc/thesis_mcg/node6.html
25. M D Segall et al., “First-principles simulation: ideas, illustrations and the CASTEP code,” J. Phys.: Condens. Matter 14 (2002) 2717–2744
26. https://en.wikipedia.org/wiki/Density_functional_theory
27. IU. M. Popov, “Stoichiometry in Crystal Compounds and Its Influence on Their Physical Properties”, 6-11
28. K. N. Tu and Wei Tang, Metallurgical microstructure control in metal-silicon reactions, Sci China Tech Sci January (2014) Vol.57 No.1 pp 1 -15
29. King-Ning Tu and Andriy M. Gusak, Kinetics in Nanoscale Materials, Wiley, New York, 2014
30. Gusak, A. M. and M. V. Yarmolenko, “A simple way of describing the diffusion phase growth in cylindrical and spherical samples,” *Journal of applied physics* 73.10 (1993) 4881-4884
31. T. Hong and A.J. Freeman, “Effect of antiphase boundaries on the electronic structure and bonding character of intermetallic systems: NiAl,” Physical Review B 43 (8) (1991) 6446-6459

32. Dobrina Iotova et al., “Electronic structure and elastic properties of the Ni3X ,X=Mn, Al, Ga, Si, Ge... intermetallic,” Physical Review B 54 (20) (1996) 413-422
33. Andrei L. Lyubimtsev et al., “The structure and bonding of Ni3Sn,” Journal of Alloys and Compounds 340 (2002) 167–172
34. P. Bruno, “Physical mechanism of oscillatory interlayer exchange coupling ,” Journal of Magnetism and Magnetic Materials 116 (1992) L13-Ll7
35. C. Papastaikoudis and D. Papadimitropoulos, “Influence of the virtual bound state on the low-field Hall coefficient. II. Dilute alloys of Sc, Ti, V, Co, and Ni in Al,” Phys. Rev. B 24 (1981) 3108
36. Hume–Rothery W. 1J.Inst.Met. 35 (295) 1926
37. Jones H. Proc.Phys.Soc. 49 (250) 1937
38. J Hafner, and M Krajci, “Covalent bonding and bandgap formation in intermetallic compounds: a case study for Al3V,” J. Phys.: Condens. Matter 14 (2002) 1865–1879
39. A.D. Smigelskas and E.O. Kirkendall, "Zinc Diffusion in Alpha Brass," *Trans. AIME,* 171 (1947), 130-142.
40. Olsen D, Wright R, and Berg, “H. Effects of intermetallics on the reliability of tin coated Cu, Ag and Ni parts.” Thirteenth annual proceedings on reliability physics (1975) 80-86.
41. M Enomoto, “Influence of Solute Drag on the Growth of Proeutectoid Ferrite in Fe–C–Mn alloy,” Acta mater., 47 (13) (1999), 3533-3540.
42. K. N. Tu et al., “Implanted Noble Gas Atoms as Diffusion Markers in Silicide Formation,” Thin Solid Films, 25 (2) (1975), 393-402.

43. E.G. Colgan and J.W. Mayer, “Diffusion Markers in Al/metal Thin-film Reactions,” Nuclear instruments and methods in physics research B, 17 (3) (1986), 242-249.
44. P. G. Kim et al., “Interfacial reaction and wetting behavior in eutectic SnPb solder on Ni/Ti thin films and Ni foils”, Journal of Applied Physics 86 (1999) 6746-6751
45. G. Ghosh, “Coarsening kinetics of Ni 3 Sn 4 scallops during interfacial reaction between liquid eutectic solders and Cu/Ni/Pd metallization,” J. Appl. Phys. **88**, 6887 (2000)
46. Henry Leidheiser Jr. et al., “Mössbauer Spectroscopy of Electrodeposited Tin‐Nickel Alloys and Thermally Prepared Ni3Sn2, NiSn, and Ni3Sn4,” J. Electrochem. Soc. 126 (2) (1979) 204-208
47. U. Gösele and K. N. Tu, “Growth kinetics of planar binary diffusion couples: Thin‐film case versus bulk cases,” J. Appl. Phys. 53, 3252 (1982)
48. AM Gusak et al., “Diffusion-controlled solid state reactions: in alloys, thin-films, and nanosystems,” Wiley, 2010
49. G. V. Kidson, J. Nucl. Mater. 3, 21 (1961).
50. Fan-Yi Ouyang, Wei-Cheng Jhu and Tao-Chih Chang, “Thermal-gradient induced abnormal Ni3Sn4 interfacial growth at cold side in Sn2.5Ag alloys for three-dimensional integrated circuits,” Journal of Alloys and Compounds, 580 (2013) 114-119
51. Guido Schmitz et al., “Reaction kinetics of Ni/Sn soldering reaction”, Acta Materialia 58 (2010) 3187–3197
52. https://en.wikipedia.org/wiki/Atomic_diffusion

53. W. J. Tomlinson and H. G. Rhodes, “Kinetics of intermetallic compound growth between nickel, electroless Ni-P, electroless Ni-B and tin at 453K to 493K”, Journal of Materials Science 22(1987) 1769 – 1772
54. M. O. Alam and Y. C. Chan, “Solid-state growth kinetics of Ni 3 Sn 4 at the Sn‑3.5Ag solder/Ni interface”, Journal of Applied Physics 98 (2005)
55. M. Mita et al., “Growth behavior of Ni3Sn4 layer during reactive diffusion between Ni and Sn at solid-state temperatures”, Materials Science and Engineering A 403 (2005) 269–275
56. Blair HD, Pan T, and Nicholson JM, “Intermetallic compound growth on Ni, Au/Ni and Pd/Ni substrates with Sn/Pb, Sn/Ag and Sn solders.” Proceedings of ECTC (1998) 259-267
57. H. Ipser et al., Interfaces in lead-free solder alloys: Enthalpy of formation of binary Ag–Sn, Cu–Sn and Ni–Sn intermetallic compounds, Thermochimica Acta 459 (2007) 34–39
58. W. Jeitschko and B. Jaberg, “Structure Refinement of Ni_3Sn_4”, Acta Cryst. B38 (1982) 598-600
59. N. T. S. Lee, V. B. C. Tan, and K. M. Lim, “Structural and mechanical properties of Sn-based intermetallics from ab initio calculations”, Applied Physics Letters 89 (2006)
60. http://home.anadolu.edu.tr/~esuvaci/egitim/Lecture2%20Diffusion.pdf
61. Michel Soustelle, “Thermodynamic Modeling of Solid Phases,” Wiley, 2015
62. K. Compann and Y. Haven, “Correlation factors for diffusion in solids”, Transactions of the Faraday Society 52(1956) 786-801

63. H.R. Glyde, “Relation of vacancy formation and migration energies to the Debye temperature in solids”, Journal of Physics and Chemistry of Solids 28(1967) 2061-2065
64. Steven D. Gardner, Gar B. Hoflund, “Characterization Study of Silica-Supported Platinized Tin Oxide Catalyst Used for Low Temperature CO Oxidation,” J. Phys. Chem. 95(1991) pp835-838
65. Andrew P. Grosvenor et al., “New interpretations of XPS spectra of nickel metal and oxides,” Surface Science 600 (2006) 1771–1779
66. Xin Ma et al., “Effect of La on the Cu–Sn intermetallic compound (IMC) growth and solder joint reliability,” J*ournal of Alloys and Compounds* 334 (2002) 224–227
67. Brook Chao et al., “nvestigation of diffusion and electromigration parameters for Cu–Sn intermetallic compounds in Pb-free solders using simulated annealing,” Acta Materialia 55 (2007) 2805–2814
68. YC Chan et al., “Aging Studies of Cu-Sn Intermetallic Compounds in Annealed Surface Mount Solder Joints,” 1996 Electronic Componentsand Technology Conference
69. C.Y. Liu et al., “Epitaxial Cu–Sn bulk crystals grown by electric current,” Acta Materialia 61 (2013) 5713–5719
70. T.L. Yang, J.J. Yu, W.L. Shih, C.H. Hsueh and C.R. Kao, “Effects of silver addition on Cu–Sn microjoints for chip-stacking applications,” Journal of Alloys and Compounds 605 (2014) 193–198
71. Gi-Tae Lim et al., “Temperature Effect on Intermetallic Compound Growth Kinetics of Cu Pillar/Sn Bumps,” Journal of Electronic Materials 38 (2009)

72. T.Y. Lee et al., “Morphology, kinetics, and thermodynamics of solid-state aging of eutectic SnPb and Pb-free solders (Sn‑3.5Ag, Sn‑3.8Ag‑0.7Cu and Sn‑0.7Cu) on Cu,” Journal of Materials Research, 17 (2002) 291-301

73. S. Poulston et al., “Surface Oxidation and Reduction of CuO and Cu2O Studied Using XPS and XAES,” Journal of Electron Spectroscopy and Related Phenamena, 4 (1974) 213-218